Monthly Notices of the ROYAL ASTRONOMICAL SOCIETY

MNRAS **540,** 919–960 (2025) https://doi.org/10.1093/mnras/staf742
Advance Access publication 2025 May 7

Exploring the chemical content of Galaxies using the SAMI Zoom Survey: a data release of 92 spatially resolved H II regions in nearby galaxies

Aaron Myszka [1,2]★ Sarah M. Sweet [2,3] Themiya Nanayakkara [1,2] Karl Glazebrook [1,2] Brent Groves [2,4] Alex J. Cameron [5] Kathryn Grasha [2,6] Mark R. Krumholz [2,6] Zefeng Li [2,6,7] Ángel R. López-Sánchez [2,8,9] David C. Nicholls [6] Stephanie Rowlands [1,2] Emma Ryan-Weber [1,2] and Yuan-Sen Ting [6,10,11,12,13]

[1] *Centre for Astrophysics and Supercomputing, Swinburne University of Technology, Hawthorn, Victoria 3122, Australia*
[2] *ARC Centre of Excellence for All-Sky Astrophysics in 3 Dimensions (ASTRO 3D), Australia*
[3] *School of Mathematics and Physics, University of Queensland, St Lucia, Queensland 4072, Australia*
[4] *International Centre for Radio Astronomy Research, University of Western Australia, 7 Fairway, Crawley, 6009 WA, Australia*
[5] *Sub-department of Astrophysics, University of Oxford, Keble Road, Oxford OX1 3RH, UK*
[6] *Research School of Astronomy and Astrophysics, Australian National University, Canberra, ACT 2611, Australia*
[7] *Department of Physics, Centre for Extragalactic Astronomy, Durham University, South Road, Durham DH1 3LE, UK*
[8] *School of Mathematical and Physical Sciences, Faculty of Science and Engineering, Macquarie University, Macquarie Park, NSW 2109, Australia*
[9] *Macquarie University Research Centre for Astrophysics and Space Technologies, Macquarie University, Macquarie Park, NSW 2109, Australia*
[10] *Research School of Computing, Australian National University, Acton, ACT 2612, Australia*
[11] *Department of Astronomy, The Ohio State University, Columbus, OH 45701, USA*
[12] *Center for Cosmology and AstroParticle Physics (CCAPP), The Ohio State University, Columbus, OH 43210, USA*
[13] *Department of Physics, Faculty of Science, Universiti Malaya, 50603 Kuala Lumpur, Malaysia*

Accepted 2025 April 29. Received 2025 April 2; in original form 2024 April 25

ABSTRACT

We present the SAMI Zoom Survey, spatially resolved IFU spectroscopy of 92 H II regions from 7 nearby galaxies (distances 2–14 Mpc) utilizing the Sydney-AAO Multi-object IFS (SAMI) instrument. Each H II region has two spectral data cubes (blue-arm sampling 1.05 Å pixel^{-1} between 3700–5746 Å, and red-arm sampling 0.57 Å pixel^{-1} between 6300–7399 Å) as well as two-dimensional emission line flux maps. The spatial sampling is 0.5 arcsec across 15 arcsec fields of view, with a mean angular resolution of 2.0 arcsec (18–150 pc). We investigate seven forms of common gas–phase metallicity determinations, contrasting metallicity calibrations including the direct electron temperature method and six strong-line methods. We determine these metallicities, temperatures, densities, and ionization parameters where possible, in spatially resolved form as well as an integrated-region data set where we focus our analysis. We find varying degrees of disparity between metallicity values using different methods, and likewise between derived abundance gradients of the host galaxies. In comparisons using R_{23} metallicity as a baseline, mean disparities span 0.12–0.49 dex in oxygen abundance depending on the chosen alternative method, with a maximum of 0.65 dex when comparing against the direct electron temperature method. Host-galaxy abundance gradients deviate up to 0.66 dex in central oxygen abundance while slopes vary by up to 0.51 dex $R_{25}{}^{-1}$. The SAMI Zoom Survey provides a data set with spatial resolution, spectral coverage, and radial extent to support the study of such astrophysical processes in nearby galaxies.

Key words: ISM: abundances – H II regions – galaxies: abundances – galaxies: evolution – galaxies: fundamental parameters.

1 INTRODUCTION

Gas-phase metallicity is an attribute closely tied to the formation and evolution of galaxies through cosmic time. The build-up of metals over time can be used to describe various dynamic processes, such as the creation and life cycles of stars, the enhancement of interstellar material in galaxies, the movement of gas into galaxies through accretion, the expulsion of gas through supernovae and galactic winds, and the merging of galaxies (Kewley, Nicholls & Sutherland 2019, and references therein).

A primary observable relating to these processes is the prevalence of radial metallicity gradients in galaxies, which describe how the abundance of metals vary moving radially outward from the centre of a galaxy. These profiles tend to be negatively sloped, as galactic centres are generally dominated by older metal-rich stars and gas while their discs contain lower-metallicity regions experiencing more active star formation (Boissier & Prantzos 1999; Fu et al. 2009; Ho et al. 2015). This relation may be used to uncover much about the evolutionary history of galaxies (van Zee et al. 1998; Bresolin et al. 2009a; Poetrodjojo et al. 2019). For instance, it should be

★ E-mail: amyszka@swin.edu.au

noted that gradients are liable to change, flattening through external interactions and galaxy merging (Rupke, Kewley & Chien 2010; Torres-Flores et al. 2014) as well as through other processes such as locally contained gas flows (Kewley et al. 2010).

Chemical abundance is a fundamental product of stellar evolution; therefore, it is a quantity which correlates with many intrinsic spectral features of galaxies and the star-forming regions within, allowing for both direct and empirical techniques for measurements. The gold standard metallicity diagnostic, the direct approach, uses the relation between observed emission line ratios and characteristic properties including the metal abundances and electron temperatures of a given region, a feature which has been known for many decades (Peimbert 1967). Here, an anticorrelation arises between electron temperature and gas-phase metallicity due to how these regions cool over time. At low metallicities, predominantly ionized-hydrogen environments provide an insufficient set of accessible electron energy levels which may be used to re-capture free electrons; therefore, the cooling of electrons is negligible. However, an increased presence of heavier elements brings an assortment of different energy levels through which a higher degree of recombination may occur, working to lower the electron temperature at a more effective rate within higher metallicities. This interaction may be investigated by observing temperature-sensitive auroral lines within emission spectra such as [O III] λ4363 and [N II] λ5755 among others, and is the basis for the various direct metallicity determinations within the literature (Hägele et al. 2008; Pérez-Montero 2017, among others).

Another observable tracer of metallicity is the collection of ratios between particular sets of strong emission lines within observed spectra, referred to as the strong emission line (SEL) methods. These work through determinations of relative emission line strengths between generally strong detections within a spectrum. Ratios here are generally compared to diagnostic curves calibrated either using observations to constrain such relations, for example Marino et al. (2013), working to refine such methods from physical data, or simulated data including stellar population synthesis and photoionization codes (STARBURST99 and MAPPINGS are often incorporated; Leitherer et al. 1999; Sutherland & Dopita 2017, respectively). Examples within this class of metallicity determination include the frequently used R_{23} diagnostic (Pagel et al. 1979; Kewley & Dopita 2002; Kobulnicky & Kewley 2004), using the ratio between a combination of [OII] λλ3726,3729 and [O III] λλ4959,5007 emission lines to the Hβ emission, as well as other methods utilizing emissions within the optical, ultraviolet, and infrared sections of the spectrum (see Kewley et al. 2019). This class of metallicity determinations are highly useful for situations where the temperature-sensitive auroral lines cannot be detected in observation, primarily for higher-metallicity regions or those which may be too faint or distant to provide detectable emissions. However, these methods may present difficulties in their use due to dependencies on ionization parameter (Kewley & Dopita 2002) as well as possible degeneracies in determined metallicities stemming from diagnostic shape (in particular R_{23}, which is not monotonic and has a prominent turning-point in its diagnostic curves). Dependencies on nitrogen abundance (specifically N/O) may also impact resulting metallicity measurements predominantly at lower metallicities ($Z < 0.5\,Z_{\odot}$, Kewley & Dopita 2002).

The discrepancy between results of differing groups of metallicity diagnostics have been the focus of much debate and development in recent years (Kewley & Ellison 2008; Peimbert, Peimbert & Delgado-Inglada 2017; Kewley et al. 2019), as the significant differences in methodologies between the direct electron temperature and empirical strong emission line methods have yet to be reconciled. This discrepancy may be severe depending on the case and has been shown to exist up to 0.7 dex in measured oxygen abundance (Kewley & Ellison 2008; Kewley et al. 2019), with direct methods reporting low metallicities and strong emission line models indicating high values, with recombination line methods typically yielding values between the two (Maiolino & Mannucci 2019). It has been theorized that these discrepancies arise due to the conditions of the inner structures found within galaxies and star-forming (H II) regions, including spatial variations of the electron temperature (Peimbert 1967; Méndez-Delgado et al. 2023), densities and pressures (Peimbert & Peimbert 2013) and degrees of ionization (Monreal-Ibero et al. 2011). Further roots to this issue have been hypothesized including the absence of a consideration for the presence of dust while using direct methods (Maiolino & Mannucci 2019) as well as the presence of nitrogen discussed above.

It is for this reason that sufficiently spatially resolved observations of galaxies and the star-forming regions within are critical in resolving the metallicity discrepancy issue. Regions of bright H II emission are ideal for such analysis, as they typically contain the strong collisionally excited nebular emissions required for metallicity determinations by either the direct or empirical approach. These regions are illuminated by the process of rapid star formation, generating large numbers of young and energetic stars which result in significant degrees of ionization throughout these regions.

There have been several previous studies addressing the gas-phase metallicity of H II regions in this context. An early work by Pagel et al. (1979) establishes one of the first metallicity methods calibrated with observational data, using auroral emission lines in combination with photoionization modelling. Pilyugin & Thuan (2005, henceforth PT05) use a large data set of temperature-based metallicity measurements to refine the relation between R_{23} metallicity and oxygen emissions across the diagnostic, a prevalent recalibration to this day. A further work by Pilyugin, Grebel & Mattsson (2012) presents a catalogue of 714 H II region spectra with at least one auroral line detection as well as detections in a set of other key emission lines used in metallicity determinations. Due to detections of multiple temperature-sensitive lines, an total of 899 electron temperature measurements are presented. Though this sample is not spatially resolved, it is an extensive compilation of temperature and metallicity data. Using this data set, the authors developed the 'counterpart' (*C*) method of determining metallicities, whereby regions of unknown metallicity are assigned a counterpart region given similar line intensities used to infer temperatures and ionic abundances.

Moustakas et al. (2010) employ the *Spitzer* Infrared Nearby Galaxy Survey (SINGS) to measure theoretical and empirical metallicities using Kobulnicky & Kewley (2004, henceforth KK04) and PT05 respectively, finding differences of 0.6 dex systematically across their sample of 21 galaxies with KK04 abundances returning higher measurements. Furthermore, metallicity gradients were compared between the two tested methods, showing some correlation however with KK04 metallicities driving consistently steeper profiles and PT05 results returning higher scatter for given radii. A study conducted by Croxall et al. (2013) bypassed temperature dependencies when measuring oxygen abundances. This was achieved by observing the far-infrared [O III] 88 μm emission using the PACS instrument on the Herschel Space Observatory, in conjunction with further emission line data from the *Spitzer* Space Telescope and the PINGS survey (additional far-infrared and optical lines). The authors derived oxygen abundances for seven H II regions within NGC 628, finding values situated between the KK04 and PT05 of Moustakas et al. (2010) given their radial positions within the galaxy.

The CHemical Abundances Of Spirals survey (CHAOS; Berg et al. 2015, 2020) has produced an extensive data base of direct-method

metallicity determinations for HII regions in nearby spiral galaxies. Using this data set, it has been shown that metallicity gradients developed using direct-method approaches show good agreement between studies (Rogers et al. 2022), however empirical SEL abundance and gradient determinations are more susceptible to disagreement and show a larger degree of dispersion between methods.

Observations within the Mapping Nearby Galaxies at Apache Point Observatory survey[1] (MaNGA; Bundy et al. 2015; Yan et al. 2016) have allowed for many studies on the abundance gradients (Belfiore et al. 2017; Zheng et al. 2017; Barrera-Ballesteros et al. 2023), impacts on metallicity due to star formation history (Goddard et al. 2017) and diffuse ionized gas (Zhang et al. 2017) across a sample of many thousands of nearby-galaxy targets. Primary outcomes include extensive fifth-order conversion relations between a set of eleven empirical metallicity calibrations based upon a large sample size on the order of one million spatial-pixel (spaxel) elements, at a resolution of approximately 1.8 kpc (Scudder et al. 2021). These have been shown to be insensitive to redshift binning within the ranges of the survey as well as the effective radius of a given observation. Furthermore, the Sydney–AAO Multi-object IFS (SAMI) galaxy survey[2] (Croom et al. 2012; Bryant et al. 2015; Sharp et al. 2015) has allowed for several studies of gas-phase metallicity at resolution scales of 1.65 kpc (median), particularly in the scope of the MZR (Sánchez et al. 2019) and the mapping and reconciling of SEL metallicities (Poetrodjojo et al. 2018, 2021) using conventional methods as well as emergent machine learning approaches across a large sample of galaxies. The authors highlight and stress the importance of robust conversion techniques between methods, particularly for high-redshift data sets where emission line observabilities and applicable diagnostics differ from that of nearby-galaxy data sets, posing a significant challenge for comparisons. This data set has also been applied to study particular local-universe candidates for high-redshift galaxy analogues (Cameron et al. 2021), matching properties of primordial galaxies such as low metallicities, indicated by strong detections of temperature-sensitive auroral emission lines, and low stellar masses.

More recently, the TYPHOON survey[3] has produced extensive well-resolved observations across local galaxy discs and resolvable H II regions within, leading to investigations of metallicities, radial abundance gradients, and spatial variations of key properties (Poetrodjojo et al. 2019; Grasha et al. 2022; Chen et al. 2023). Furthermore, the PHANGS-MUSE survey[4] (Emsellem et al. 2022) has been utilized to assemble a data set of many thousands of additional H II regions in 19 local spiral galaxies, forming further metallicity comparisons using an integrated-spectrum approach and detailing strong radial trends and residual variations with respect to ISM properties (Groves et al. 2023).

Another study presented by Jin et al. (2023) has shown highly detailed insights from four H II regions within the Small and Large Magellanic Clouds, investigating the prevalence of temperature and density structures at a very high resolution of 0.2–0.3 pc. This has allowed for the development of nebular models where these two properties may vary.

However, the above studies are limited with respect to the spatial resolution of finalized results, sampling size or radial extent, or measured spectral ranges. While CHAOS has been able to produce extensive coverage across entire galaxy discs, the H II regions observed within are covered only by single-slit apertures, prohibiting an analysis of spatial variations of properties within them. Others including MaNGA and the SAMI Galaxy Survey, also do not have the spatial resolution required to reach the sub-100 pc scales required to resolve these regions from diffuse ionized gas (DIG), which contaminate observations (Poetrodjojo et al. 2019). While PHANGS-MUSE does have this ability, resolving up to 10 pc scales, the limited wavelength coverage excludes bluer emission lines below wavelengths of 4850 Å. A very recent study performed by Rickards Vaught et al. (2024) bypasses this limitation by utilizing further MUSE observations in conjunction with blue-spectrum observations obtained with the Keck Cosmic Web Imager (KCWI). In this way, the authors are able to measure electron temperatures across differing ionization zones within many H II regions in nearby galaxies, with a metallicity analysis on these regions forthcoming.

The factors detailed above constrain the potential for a robust analysis of spatial variations within H II regions, as well as impacts on metallicity determinations and the comparisons between direct and empirical methods. For this reason, we present the SAMI Zoom Survey, an integral-field spectroscopic survey of 92 confirmed star-forming regions in seven nearby galaxies (distances 2–14 Mpc), covering spatial resolutions (approximately 18–150 pc) sufficient to resolve H II regions and a spectral range large enough to characterize the metallicity using a wide range of standard calibrations, sensitive enough in some cases to determine [OIII] temperatures for direct metallicities.

This is the first publication on the SAMI Zoom Survey, presenting the H II region sample and data in spatially resolved and integrated forms, observed emission line fluxes, and derived metallicity measurements and region properties. Also presented are comparisons between these properties as well as metallicity gradients of the host galaxies. A study on the spatially resolved distributions of various region properties, including temperatures, densities, and metallicities, and their impact on the metallicity discrepancy, is forthcoming (Sweet et al., in preparation).

We summarize the SAMI Zoom Survey target selection and observations in Section 2, and the data reduction and processing techniques in Section 3. Metallicity determinations and gradients using multiple diagnostics are described and presented in Section 4, with complete tabulated results in Appendix A. The results of these findings are discussed in Section 5, and we conclude in Section 6.

2 SAMI ZOOM OBSERVATIONS

The parent catalogue for the SAMI Zoom Survey contained star-forming H II regions in face-on galaxies, compiled using the NASA Extragalactic Data base[5] and sourced from multiple catalogues, that were observable at the AAO. The host galaxies were drawn from a list of nearby galaxies (distances < 20 Mpc) that were accessible to the AAT during the scheduled observing dates throughout 2017 April and 2018 July. Face-on galaxies were prioritized but not required.

A high-priority list of H II regions was drawn from published catalogues (see Table 1). This list was supplemented with lower-priority emission line candidates detected in SINGG narrow-band imaging (Meurer et al. 2006) using HIIPHOT (Thilker, Braun & Walterbos 2000); this supplied all targeted regions within NGC 3521 and IC 5201, as well as all but one region within NGC 5068. The high-priority list spans effective radii up to approximately 2.14 R_{25}, with

[1] https://www.sdss4.org/surveys/manga/
[2] http://www.sami-survey.org/
[3] https://typhoon.datacentral.org.au/
[4] https://sites.google.com/view/phangs/home
[5] NASA Extragalactic Database: https://ned.ipac.caltech.edu/

Table 1. Source catalogues used in the construction of the SAMI Zoom Survey target list. These are listed with corresponding observational targets in Table A1.

Catalogue	Reference
6dF	Jones et al. (2009)
ATCA	Payne et al. (2004)
BKR12	Bresolin, Kennicutt & Ryan-Weber (2012)
dPD83	Rumstay & Kaufman (1983)
DRW83	Dodorico, Rosa & Wampler (1983)
GALEX	Martin et al. (2005)
H76	Hodge (1976)
HIIPHOT	This work (see Section 2)
HK83	Hodge & Kennicutt (1983)
KWB2013	Khramtsova et al. (2013)
RK83	Rumstay & Kaufman (1983)
S66	Sérsic (1966)
SSTS	Faesi et al. (2014)
SSTSL	Bresolin et al. (2009a)
WS83	Webster & Smith (1983)

R_{25} describing the 25th B-magnitude per arcsecond squared radius of a host galaxy, while the HIIPHOT catalogue has a broader spatial coverage out to 3.67 R_{25}. The *greedy* tiling algorithm (Robotham et al. 2010) was used to make a blind selection across ionization parameter and metallicity. While the algorithm prioritized literature-sourced H II regions, it included candidate H II regions from the HIIPHOT catalogue especially towards the outskirts of the host galaxies where there were fewer H II regions confirmed by previous sources. In total, 156 targets across seven host galaxies were included in the initial sample, 46 of which originated from the HIIPHOT selection.

The host galaxies are shown in Fig. 1 and summarized in Table 2. Host galaxies hold distances less than 14 Mpc and isophotal radii between 3 and 10 arcmin, corresponding to physical diameters of 11.2 to 32.8 kpc. Observations were conducted during 2017 and 2018 using the SAMI instrumentation (Croom et al. 2012) on nine observing nights at the Anglo–Australian Telescope (AAT), situated at Siding Spring Observatory in NSW, Australia. The instrumentation used is the same as the SAMI Galaxy Survey (Scott et al. 2018); however, rather than assigning entire galaxies to each optical fibre bundle, observations of individual HII regions were the objective.

The observations made use of the SAMI instrument, which fed the AAOmega spectrograph. This instrument was fitted with an array of 13 hexabundles of 61 fibres, each covering a total field of view with a diameter of 14.7 arcsec (Sharp et al. 2015) as well as a practical collision radius of 15mm (approximately 228 arcsec; Croom et al. 2012). This collision radius imposed a constraint on the positioning of target regions as they could not physically be placed closer together than this limit due to cladding around the optical fibres. This further emphasizes the benefit of selecting targets towards galactic outskirts in addition to the previously documented inner HII regions.

While observing, each hexabundle was placed across a singular targeted HII region for an average exposure time of 89 minutes per region, allowing for effective spatially resolved observations. To increase the fidelity of the observations, each was dithered between five and seven times. To observe in the blue-arm wavelength range (3700–5746 Å), a 580V grating was used on the instrument. A 1000R grating was used for observing the majority of regions in the red arm (6300–7399 Å), though four regions in NGC 628 were observed using a 385R grating instead. These gratings provided sufficient range to measure targeted emissions, listed in Table 3. The specific observational parameters for each region are listed in Table A1.

Throughout the duration of the observing, each pointing had an individual hexabundle placed over a standard reference star for accurate determination of instrument position, flux calibrations and PSF measurements, which took place throughout the data reduction process (see Bryant et al. 2015, section 9). The resolution of the final data cubes ranged between 1.6–3.7 arcsec with a mean of 2.0 arcsec.

3 DATA REDUCTION AND INITIAL PROCESSING

3.1 2dFdr

The raw telescopic data was processed through the SAMI python manager, which calls the Two-Degree Field Data Reduction pipeline (2dFdr, Sharp et al. 2015) to reduce the AAOmega spectrograph data and produce spectral cubes. The version used for the SAMI Zoom Survey most closely resembles that described in Scott et al. (2018), with modifications to better suit our data set of H II regions. While the full process may be found in Sharp et al. (2015), a brief overview is given here.

First, flat and dark fields taken throughout the observational window were used to subtract the bias voltage and correct for any fibre-to-fibre variations across the instrument. Then, the position of each individual fibre within a hexabundle was located and traced to produce tramline maps across the data, indicating precise pixel locations as well as the curvature of each fibre line resulting from the light path through the instrument.

With the fibres traced and fitted, a wavelength calibration process was applied. Prior to observations, the detector was uniformly illuminated using copper-argon lamps; this allows the spectral information to be corrected, if necessary, as well as any curvature that may be present in the data. Then, further subtractions and calibrations were applied with respect to sky frames – direct observations of empty sky which are used to account for any atmospheric effects throughout the observations – as well as concurrent observations of standard stars of known luminosity, which also works to correct for any atmospheric or telluric effects.

Once all of these corrections and calibrations were carefully handled, the location of the data from each fibre was mapped to an x/y plane. The data was scaled to ensure measured flux is accurate, and the spectra were collated to form a data cube – one per observed H II region. The data cubes comprised of three-dimensional data, two spatial dimensions and one spectral. The spectral information was split into a blue and red arm, with wavelength coverages of 3750 to 5746 Å and 6300 to 7399 Å, respectively.

These data cubes held a spatial sampling of approximately 0.5 arcseconds per spaxel, and with spectral samplings of 1.050 Å per bin in the blue arm and 0.596 Å per bin in the red.

3.2 Spectrum fitting

The IDL program LZIFU (Ho et al. 2016) was first used to produce flux-calibrated data cubes from the reduced data. This program takes in the reduced H II region data cubes and performs a series of per-spaxel continuum fitting, continuum subtraction and emission line fitting to produce spatially resolved emission line maps of the data set. Through a series of trials, we found the provided *MILES* stellar population templates[6] (Sánchez-Blázquez et al. 2006;

[6]The *MILES* templates: http://research.iac.es/proyecto/miles/

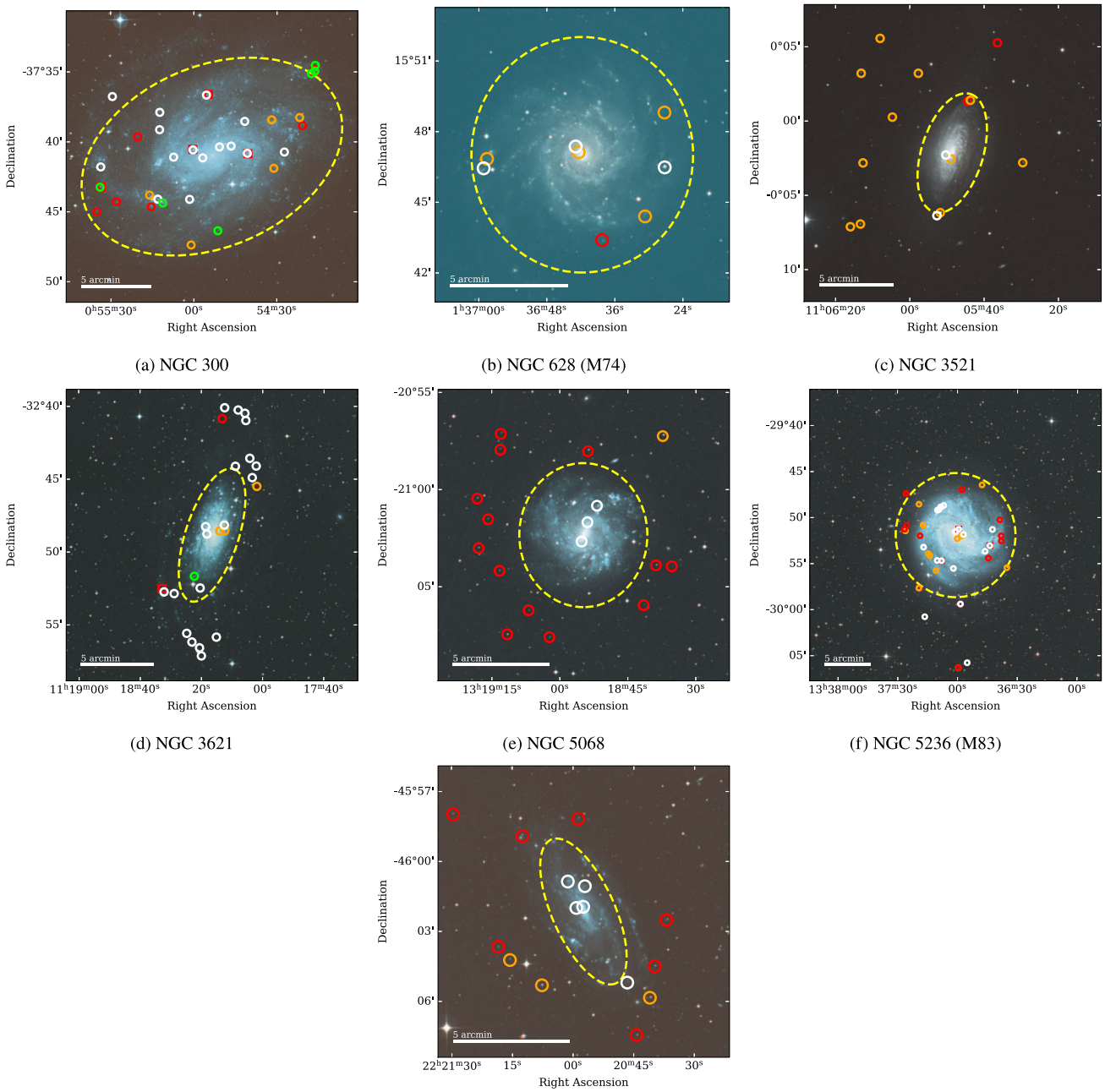

(a) NGC 300 (b) NGC 628 (M74) (c) NGC 3521

(d) NGC 3621 (e) NGC 5068 (f) NGC 5236 (M83)

(g) IC 5201

Figure 1. The seven host galaxies in the SAMI Zoom sample. Observed fields of view (as listed in Table A1) are indicated by to-scale markers and are coloured to distinguish fields with confirmed H II regions in white, or green if they also held measurable auroral [O III] λ4363 emission. Fields without confirmed H II regions are otherwise shown in orange if they could not be sufficiently fitted as red circles if the observed data was too poor (discussed within Section 3.5). Regions which were spatially coincident with a confirmed region of higher quality are indicated by red squares behind their preferred counterparts. The projected boundary of each host galaxy with respect to the 25th B-magnitude per arcsecond squared radius (R_{25}) is shown as yellow dashed ellipses, and 5 arcmin scale bars have been added to the lower left corner of each plot. Imagery sampled from the DSS2 survey (available at https://archive.eso.org/dss/dss).

Cenarro et al. 2007; Falcón-Barroso et al. 2011) in conjunction with fourth-degree additive polynomials gave the lowest residuals throughout continuum fitting.

While LZIFU is designed to completely process given spectra into fully fitted emission-line fluxes and uncertainties, throughout numerous attempts with the SAMI Zoom data cubes we came across some difficulty. The process worked well in many cases; however, we found that far too many flux values were being reported by the program without calculated uncertainties. While much time and effort were taken to find the root of this problem, it was decided that using this sole program to process the data cubes would be unfeasible due to the aforementioned complication. As the stellar continuum fitting was obtained without issue using LZIFU, these were retained and used throughout the further steps to convert the observed data cube spectra into continuum-subtracted analysable data.

As an alternative to the LZIFU spectrum fitting, the code LMFIT (Non-Linear Least-Squares Minimization and Curve-Fitting for PYTHON, Newville et al. 2014) was incorporated into the process.

Table 2. Summary of the host galaxies within the SAMI Zoom Survey and their targets. Cosmological constants $H_0 = 69.6\,\mathrm{km\,s^{-1}\,Mpc^{-1}}$ and $\Omega_m = 0.286$ are assumed for the calculation of mean physical resolution.

Host Galaxy	RA (hms)	Dec. (dms)	Mean angular resolution (arcsec)	Mean physical resolution (pc)	Published targets	HIIPHOT targets	Confirmed H II regions
NGC 300	00:54:53.48	−37:41:03.80	1.88 arcsec	18.0	37	0	25
NGC 628 (M74)	01:36:41.75	+ 15:47:01.18	3.05 arcsec	149.3	8	0	3
NGC 3521	11:05:48.58	−00:02:09.11	1.74 arcsec	144.4	0	15	3
NGC 3621	11:18:16.51	−32:48:50.60	1.88 arcsec	57.5	25	0	27
NGC 5068	13:18:54.81	−21:02:20.80	2.29 arcsec	57.2	1	16	4
NGC 5236 (M83)	13:37:00.95	−29:51:55.50	1.79 arcsec	42.5	39	0	23
IC 5201	22:20:57.44	−46:02:09.10	2.16 arcsec	113.8	0	15	7
Total					110	46	92

Table 3. The 20 blue-arm and 9 red-arm spectral emission lines fitted in this work with their observed (air) wavelengths listed in Ångstroms. Wavelength values were obtained from the NIST Atomic Spectra Database (available at https://www.nist.gov/pml/atomic-spectra-database).

Blue-arm species	λ_{air} (Å)	Red-arm species	λ_{air} (Å)
[O II]	3726.04	[S III]	6312.06
[O II]	3728.80	[N II]	6548.05
[Ne III]	3868.76	Hα	6562.79
He I	3888.65	[N II]	6583.45
Hϵ	3970.08	[He I]	6678.15
Hδ	4101.73	[S II]	6716.44
Hγ	4340.47	[S II]	6730.82
[Fe II]	4358.16	He I	7065.19
[O III]	4363.21	[Ar III]	7135.80
He I	4471.48		
He II	4685.70		
He I	4713.15		
Hβ	4861.35		
He I	4921.93		
[O III]	4958.91		
[O III]	5006.84		
He I	5015.68		
[N I]	5199.84		
[N I]	5201.61		
[N II]	5754.59		

For each spaxel in the data set, the blue-arm and red-arm spectra are fitted independently of each other, as well as from other spaxels in its region.

For each spectrum in the sample, the [O III] λ5007 and Hα λ6563 emissions were used as reference lines due to their relative high flux in the blue and red arm spectra, respectively. Measured widths and positions of these reference lines were used to constrain the parameters during the fitting of each other line in their respective spectral arms; the positions of the remaining lines were fully constrained based on the reference line redshifts in each arm, while their width parameters were constrained to lie within 0.5 Å of the corresponding reference-line widths.

Furthermore, to ensure accuracy and maintain the quality of the results, quality checks were performed throughout the fitting process. This involved calculating fractional differences between the data and the fitted model, with spectra exceeding a threshold of 5 per cent flagged and removed from the data set.

Once the fitting for all spectra within a given region was performed, the three values for all emission line component fits – wavelength (λ), width (σ), and flux (F) – for each line were recorded. These were then used to generate emission line maps for each region in the data set. An example of a set of final spatially-resolved emission line maps is shown in Fig. 2.

Emission line flux uncertainties were determined throughout the data set by measuring the degree of root-mean-square (RMS) scatter throughout a central section of each spectrum with emission lines masked out. The wavelength ranges considered for the uncertainty extraction were between 4300–5100 Å in the blue-arm spectra, and between 6500–7200 Å in the red; this was done to reduce the impact on the RMS from spectral features towards the edges of the full spectral ranges. The measured RMS scatter is then scaled in quadrature by a number of times equal to the amount of spectral bins encompassing a 5σ interval around each emission line, to represent the full amount of error integrated across such an interval. As the amount of bins within this range is equivalent between emission lines of a spectral arm (due to the constraint on line width implemented in the fitting), lines of an arm also share equivalent flux uncertainty values (see Table A2).

We perform the error analysis in this way because we are limited in the systematics we can access and analyse. While the LMFIT process does return values for error in the fitted Gaussian models, they appear to significantly underestimate this error when taking the amount of RMS scatter within the spectra into account, indicating the need for the additional approach. Regarding the underestimation, uncertainties reported by the LMFIT program across the sample are approximatlely 1.44 and 6.80 times smaller than the RMS-based errors on average for the bright [O III] λ5007 and Hα lines respectively. For the fainter [O III] λ4363 emissions, we see LMFIT errors smaller by a factor of 1.97 on average.

3.3 Region bounding

On several occurrences throughout the SAMI Zoom data set, multiple distinct areas of high flux were apparent within individual fields of view. This indicated the possibility of multiple sources of ionization existing in a given observation. In order to separate potential distinct HII regions to be analysed individually, boundaries were developed between these areas and the data files were divided accordingly.

The ASTRODENDRO PYTHON package[7] (Robitaille et al. 2019) was used to find borders between these areas of high flux. This package utilizes dendrograms, a method of arranging hierarchical data into a tree-like structure composed of 'branches' (intermediate elements) and 'leaves' (endpoint elements). In the context of astronomical data, dendrograms may be used to identify distinct features and structures

[7] ASTRODENDRO: https://dendrograms.readthedocs.io/en/stable/

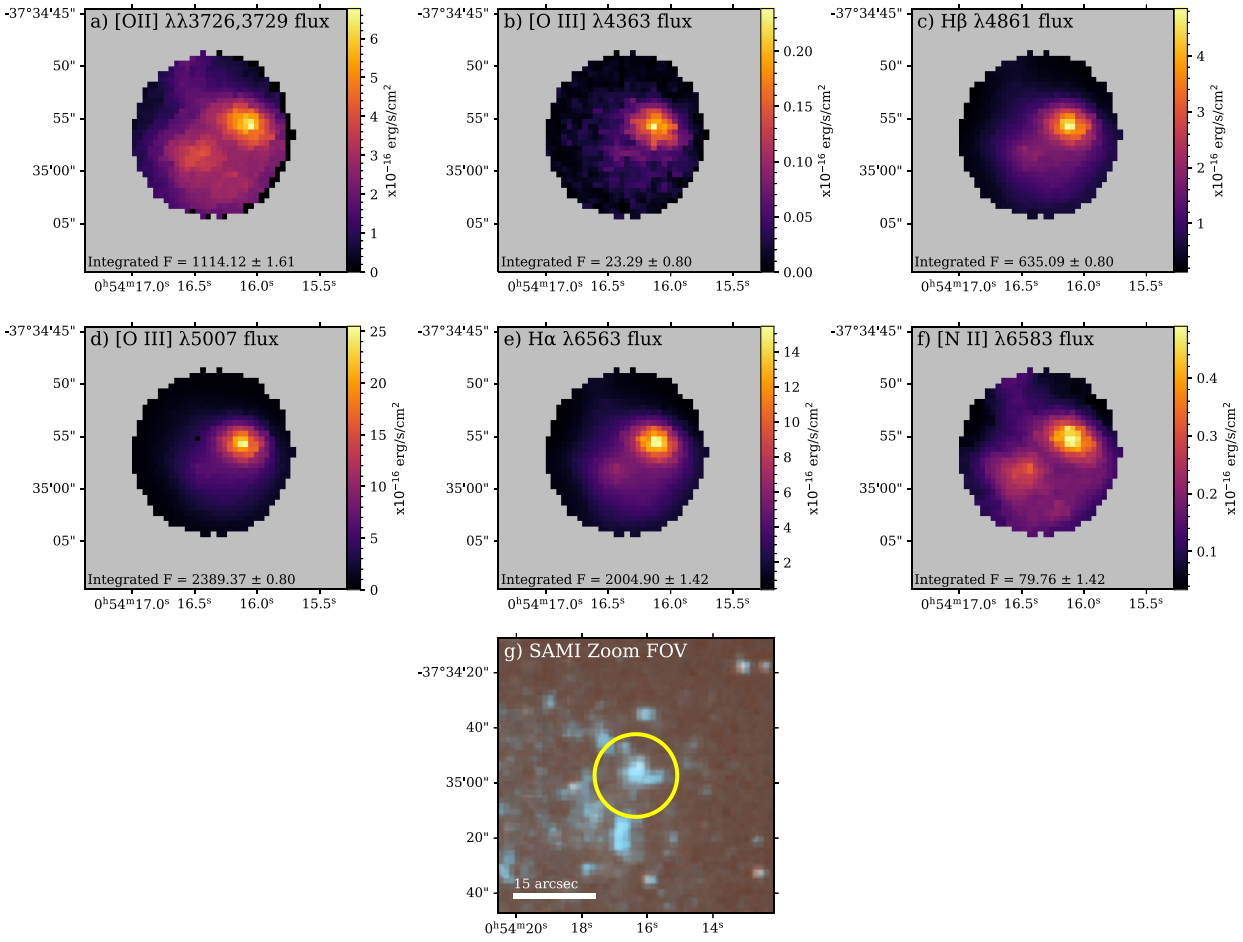

Figure 2. Example of spatially resolved flux maps from SAMI Zoom H II region 300002271.0, showing the approximately 15-arcsecond field of view across multiple key emission lines. The corresponding flux values determined using the integrated region data set are also shown in the bottom-left corner of panels a to f. Also shown in panel g is the SAMI Zoom field of view superimposed over the position of the region as imaged by the DSS2 survey (available at https://archive.eso.org/dss/dss).

of interest within an observation, for example individual areas of distinct contiguous flux.

For each SAMI Zoom field of view, a summation of the H α, H β, and [O III] λ5007 emission line fluxes was used as the baseline signal maps for this process; these lines effectively trace high flux and ionization throughout the observations. For the bounding algorithm, the minimum flux required for a spaxel to be considered part of a high-flux area was set as three times the mean uncertainty in H α + H β + [O III] λ5007, as given by LZIFU[8], across an observation. The algorithm also requires the specification of the the minimum difference in flux needed to distinguish two high-flux areas as separate dendrogram leaves; this was set to the mean noise value measured across the observations. Also, the minimum angular size of a high-flux area to be considered for a dendrogram leaf was set to the angular resolution of the observation.

Borders were initially established around the 'leaves' of the resulting dendrogram structures, the distinct areas of brightest flux. Then, to fill out the field of view of each observation, each spaxel not assigned to a dendrogram 'leaf' was set to belong to the nearest leaf. An example of this process can be seen in Fig. 3. Furthermore, leaves of insignificant structure were manually omitted before these extended boundaries were created.

Of the initial 156 observations, 138 (approx. 84 per cent) FOVs remained whole without any intermediate boundaries. 23 observations were split into two bounded regions, 3 observations into three bounded regions and 1 observation into four bounded regions. In total, 197 bounded regions were defined.

These bounded regions are named by taking the name of the target and adding a suffix as assigned by the bounding process (i.e. '.0', '.1', etc.). These suffixes were assigned arbitrarily to the structures within the dendrograms (both branches and leaves), so some sets of regions from the same target may have non-sequential suffixes. An example of this being regions 300003096.0 and 300003096.2; there is no region 300003096.1 as the suffix '.1' was not assigned to a dendrogram leaf and therefore was not propagated into a separate H II region. This may also occur if a potential region was removed from the data set due to being unconfirmed (see Section 3.5).

For the remainder of this paper we opt to focus on the integrated data set (described in the following Section 3.4) for the purpose of contextualizing SAMI Zoom. In a future paper (Sweet et al., in

[8]The LZIFU results were not used in the overall region flux analysis due to the issues outlined in the previous section, however the program worked sufficiently enough for bright emissions (H α, H β, [O III] λ5007) to be used as initial parameters for the bounding.

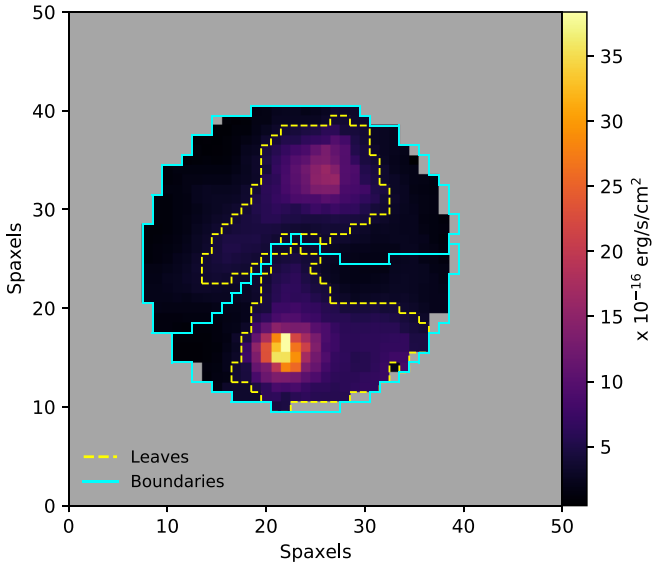

Figure 3. An example of the ASTRODENDRO region-bounding method applied to SAMI Zoom target 300003026. The map of the combined Hα + Hβ + [O III] λ5007 flux used to arrange the dendrogram is overlaid with resulting leaf boundaries (dashed lines) and final extended boundaries (solid lines), which in this case was used to split the FOV into the two distinct regions 300003026.0 (upper) and 300003026.2 (lower).

preparation), we will analyse the spatially resolved data set to address the implications of spatial varitions across these regions.

3.4 Integrated data set

As a second set of data products, the spectra for each confirmed H II region in the sample were combined to form a set of fully integrated spectra.

The signal and variance spectra of each spaxel across the data set were optimally integrated using profile weighting. This was performed by taking the spatially resolved [O III] λ5007 flux, as previously determined, as the profile and using the equation:

$$F = \left(\sum_{i=1}^{n} P_i\right) \cdot \frac{\sum_{i=1}^{n} \frac{w_i}{\sigma_i^2} \cdot F_i \cdot P_i}{\sum_{i=1}^{n} \frac{w_i}{\sigma_i^2} \cdot P_i^2} \quad (1)$$

where P_i is the [O III] λ5007 profile, w_i is the weight (set to 1 unless masked, in which case set to 0), F_i is the flux value within each spatial bin (substituted for the variance when combining the variance spectra), and σ_i is the corresponding standard deviation value, equal to the square root of the variance in the spatial bins. The [O III] λ5007 emission was chosen as this profile for both spectral arms as it was primarily one of the brightest lines across the observations as well as the importance of using the temperature-sensitive [O III] λ4363 emission in our metallicity analysis (see Section 4.1).

These combined spectra were then fed through LZIFU in much the same way as the spatially resolved data to obtain model continua to subtract off and then sent through the spectrum-fitting codes.

This data set contains significantly higher data quality (signal-to-noise ratio, or SNR); however, all spatial information regarding the distributions of properties including emissions, ionization, and electron temperatures and densities within each represented H II region is lost.

An example representative integrated H II region spectrum is shown in Fig. 4.

3.5 Data quality

Of the original 197 bounded potential H II regions in the data set, a total of 92 (approximately 47 per cent) were able to be confirmed as H II regions and used in the metallicity analysis. The remaining 105 were removed due to a number of factors. The most prevalent of these was the faintness of emission lines in the spectra, leading to an inability to observe or measure prominent emission lines including [O III] λ5007 and/or Hα even in the integrated form, as was seen in 40 cases.

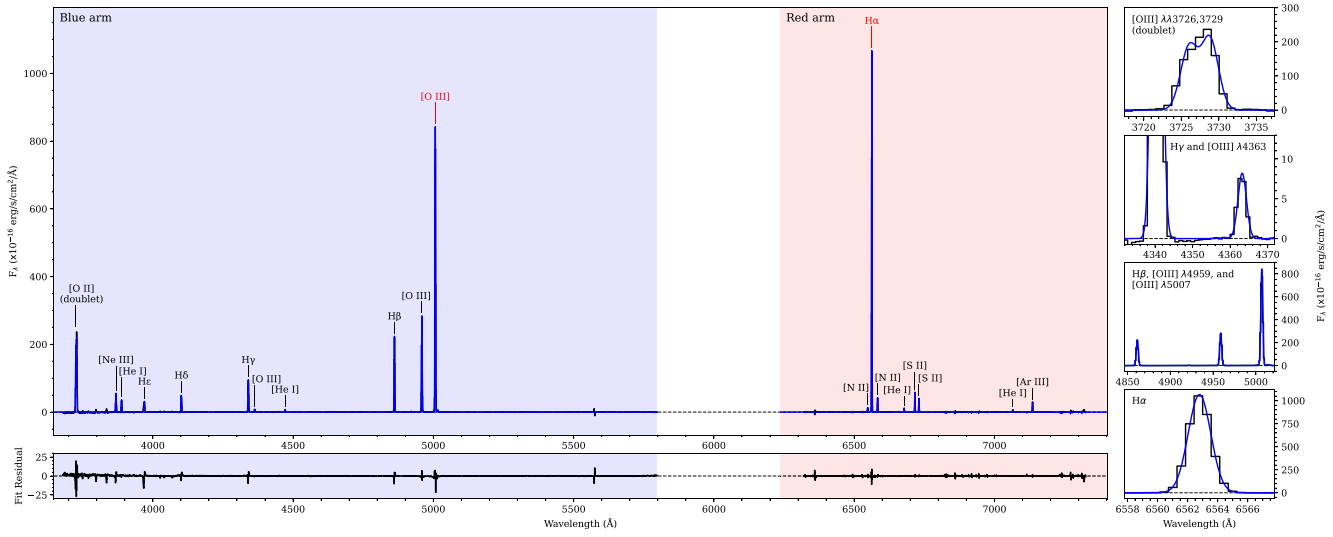

Figure 4. The continuum-subtracted spectrum of integrated SAMI Zoom H II region 300002271.0 (pictured in Fig. 2) in observed and fitted forms. The blue- and red-arm spectral ranges are indicated by shaded regions on the left and right of the primary panel respectively. Fit resuduals are shown below the full spectrum in the lower left panel, and zoomed-in windows are placed along the right side to view emission lines of interest in more detail. Prominent emission lines are labeled, with the full list of fitted lines is shown in Table 3. It should also be noted that while this spectrum has prominent [O III] λ4363 emission, this is a rarity as the line is not detected in the majority of the H II region spectra.

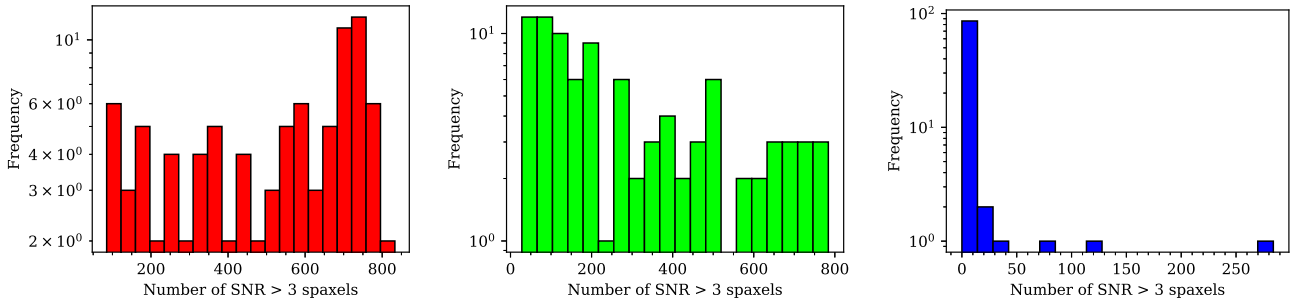

(a) Hα (b) [OIII] λ5007 (c) [OIII] λ4363

Figure 5. Histograms of the number of spaxels in each unbinned H II region with a measured signal-to-noise ratio (SNR) greater than three for a the key emission lines Hα, [O III] λ5007, and [O III] λ4363. There is a median 702.5 spaxels of data per region.

In addition, 24 regions were excluded due to significant fractional differences between the data and fit for reference lines ([OIII] λ5007 and Hα for the blue and red arm spectra, respectively) as described in Section 3.2. A further 22 were excluded due to poor continuum fitting or subtraction, resulting in processed spectra that were not uniformly flat at zero flux across wavelength ranges in the absence of emission lines; these could not have emission lines reliably fitted or measured. These two categorizations may be further attributed to a number of factors including faintness of the continuum or stellar contamination. 16 regions were removed from the data set as they were spatially coincident with other confirmed regions, as to not double-count regions in the further metallicity comparison and host-galaxy gradient analysis. In such cases, the region with the higher-quality spectrum was selected for further analysis.

The remaining three regions which were excluded from the data set showed significant emission broadening across their integrated spectra. Measuring such emissions requires a more complex fitting routine including multiple-Gaussian emission fits which was outside the scope of this study. Due to the implications of underlying physical conditions unique to these three regions in the sample, they were not considered for further analysis in this study.

The 105 regions excluded from the data set were not considered in any of the following metallicity analysis in Sections 4 and 5. This cut corresponds to a loss of observational target pointings from the original 156 (see Table 2) to a final total of 75 (approximately 48 per cent). The corresponding number of regions within these pointings changed from 197 potential regions to the 92 confirmed in the final sample.

Within the group of 92 confirmed regions, varying levels of emission line observabilities can be seen. In terms of the spatially resolved data set, a significant amount of variability can be seen in the amount of spaxels where emission lines are detected. For the key reference lines, [O III] λ5007 and Hα were generally readily observable, with an average of 57 per cent and 92 per cent of spaxels per region holding a signal-to-noise ratio of three respectively. Furthermore, 90 of the 92 confirmed regions (98 per cent) held at least 30 well-detected [O III] λ5007 spaxels per IFU bundle, with all regions for Hα. In the entire resolved confirmed region sample, a total of 46 660 spaxels held detected (SNR $>$ 3) Hα detections, with 32 175 in Hβ, 26 677 in [O III] λ5007, and 713 in [O III] λ4363. Maps of the Hα and [O III] λ5007 flux for these 92 regions are shown in Fig. A1.

In terms of the spatially resolved detectability of [O III] λ4363, a line crucial in the determination of metallicities via the direct method, regions had an average of 7.8 spaxels with this line detected to the SNR $>$ 3 threshold, and only 4 of the 92 regions had greater than 30 well-detected spaxels using this line. Histograms covering the distributions of good-SNR spaxels for these emission lines are presented in Fig. 5.

As for the integrated-region data set, each of the 92 confirmed H II regions had at least a SNR of 3 in both [O III] λ5007 and Hα, with mean SNRs of 210 and 181, respectively. For [O III] λ4363, 8 of the 92 regions (8.7 per cent) had a SNR greater than 3, with the mean value across the sample being approximately 1.49. Histograms displaying the distributions of SNRs for these lines in the integrated data set can be found in Fig. 6, with a decumulative representation of the integrated region SNR values in Fig. 7. Fitting the temperature-sensitive emission lines [N II] λ5755 and [S III] λ6312 was also attempted. However, due to their intrinsic faintness and proximity to the boundaries of their respective spectral arms, the data quality at these wavelengths was unfortunately insufficient for accurate fitting.

4 METALLICITY DETERMINATIONS AND RESULTS

Prior to each metallicity determination, a reddening correction was applied to all emission line fluxes. We use the method provided within the PYNEB PYTHON package[9] (Luridiana, Morisset & Shaw 2015), using the theoretical ratio of the two strongest observed Balmer lines, Hα / Hβ = 2.85 (Osterbrock 1989). This procedure follows the CCM89 dust correction of Cardelli, Clayton & Mathis (1989). Once completed, the metallicities within each H II region in both unbinned and integrated form were determined by the following methods.

We present the seven metallicity methods applied in this study in Sections 4.1 to 4.7, and an explanation of our method of determining uncertainties is given in Section 4.9.

4.1 The direct electron temperature (T_e) method

The direct electron temperature method metallicity was computed using the framework presented by Pérez-Montero (2017, henceforth P17), described briefly here. For a detailed description of this method and the basis for its physical derivation, see Nicholls, Kewley & Sutherland (2020).

The ratios of certain emission lines used in this method are as follows:

[9]PYNEB: http://research.iac.es/proyecto/PyNeb/

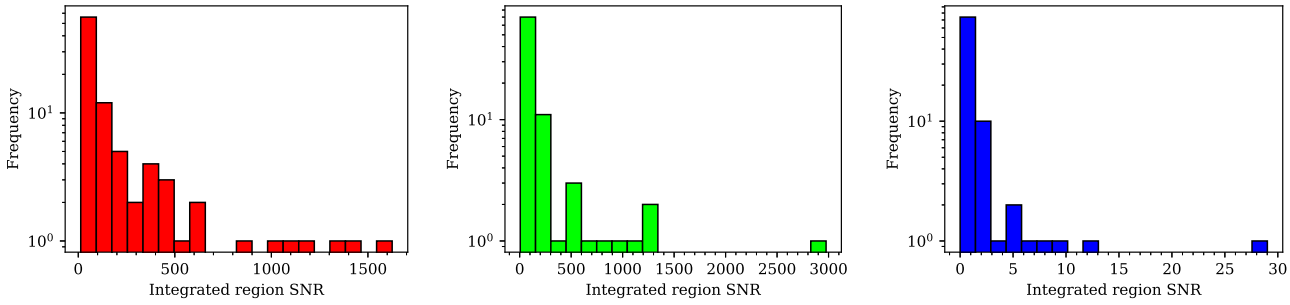

(a) Hα (b) [OIII] λ5007 (c) [OIII] λ4363

Figure 6. Histograms of the measured signal-to-noise ratio (SNR) per integrated region for the key emission lines Hα, [O III] λ5007, and [O III] λ4363.

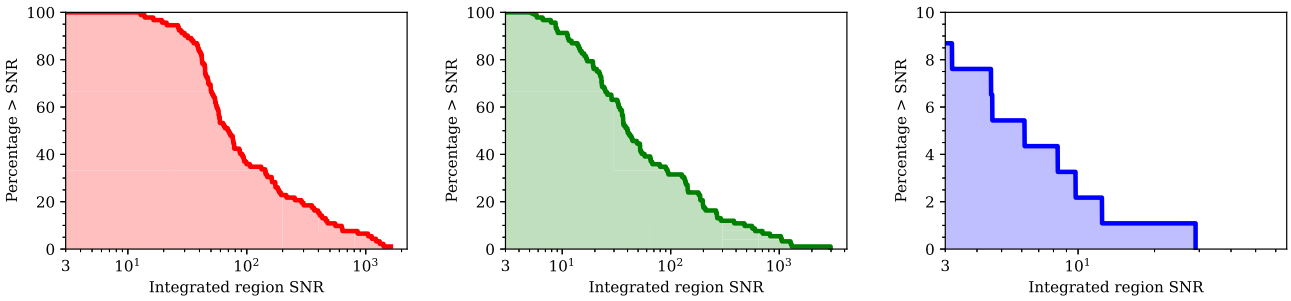

(a) Hα (b) [OIII] λ5007 (c) [OIII] λ4363

Figure 7. The decumulative proportion of integrated regions with measured signal-to-noise ratio (SNR) greater than the values along the x-axis, shown for the key emission lines Hα, [O III] λ5007, and [O III] λ4363. The plots begin at an SNR of 3 on the x-axis, the applied threshold for a confirmed line detection. 100 per cent of the 92 integrated-region spectra have SNR $>$ 3 in Hα and [O III] λ5007 flux, whereas only 8.7 per cent (8/92 region spectra) achieve this in [O III] λ4363 flux.

$$R_{O3} = \frac{[\mathrm{O\,III}]\,\lambda\lambda 4959, 5007}{[\mathrm{O\,III}]\,\lambda 4363} \tag{2}$$

$$R_{S2} = \frac{[\mathrm{S\,II}]\,\lambda 6716}{[\mathrm{S\,II}]\,\lambda 6731} \tag{3}$$

The intrinsic relation set by quantum physics between the fluxes of [O III] λ4959 and [O III] λ5007 was used to obtain the former:

$$[\mathrm{O\,III}]\,\lambda 4959 = \frac{1}{2.98} \cdot [\mathrm{O\,III}]\,\lambda 5007 \tag{4}$$

This equivalence removes the need for manually measuring [O III] λ4959 from data, so this line was not included in the fitted line list previously discussed throughout the methods.

Electron temperatures were determined using the ratio of temperature-sensitive [O III] emission lines, as given by the authors of P17:

$$T_{O3} = 0.7840\text{–}0.0001357 \cdot R_{O3} + \frac{48.44}{R_{O3}} \tag{5}$$

in units 10^4 K. Values of T_{O3} less than the given lower bound of 0.7×10^4 K were set to equal this value; however, the resulting metallicities in these cases are excluded from the data set to avoid inaccuracy due to their the strong dependence on temperature. Resulting electron densities using this temperature assumption are less impacted by inaccuracies in temperature and are retained, however these should be addressed with the assumptions in mind.

An additional method to determine electron temperatures is given by Nicholls et al. (2020), whereby the authors fit values for electron temperature using a polynomial ratio, in terms of a chosen emission line ratio. Choosing the ratio [OIII] λ4363/([O III] λ4959 + [O III] λ5007), this polynomial fit is given as:

$$\log(T_e) = \frac{3.5363 + 7.2939 \cdot x}{1 + 1.6298 \cdot x - 0.1221 \cdot x^2 - 0.0074 \cdot x^3} \tag{6}$$

with T_e in units K and where x is the aforementioned emission line ratio. Temperatures determined using this method were found to vary from the previous T_{O3} values from equation (5) by a small 0.2 per cent to 2.7 per cent, so we continue to use the P17-method temperature values going forward.

Electron densities were determined using the method given by P17, using their equation:

$$n_e = 10^3 \cdot \frac{R_{S2} \cdot a_0(T_{O3}) + a_1(T_{O3})}{R_{S2} \cdot b_0(T_{O3}) + b_1(T_{O3})} \tag{7}$$

with n_e in units of cm^{-1}. Similar to the re-assignment of out-of-bounds values of T_{O3}, n_e values less than their given lower bound of 10 cm^{-3} were also set to this value. The four additional functions of temperature in the above are given in P17 as:

$$a_0(t) = 16.054 - 7.79 \cdot t^{-1} - 11.32 \cdot t \tag{8}$$

$$a_1(t) = -22.66 + 11.08 \cdot t^{-1} + 16.02 \cdot t \tag{9}$$

$$b_0(t) = -21.61 + 11.89 \cdot t^{-1} + 14.59 \cdot t \tag{10}$$

$$b_1(t) = 9.17 - 5.09 \cdot t^{-1} - 6.18 \cdot t \tag{11}$$

where the values for T_{O3} are substituted in for t.

With electron temperature and density in hand, the relative abundances of O^+ and O^{2+} may be separately calculated the following equations given by P17:

$$\begin{aligned} Z_1 &= 12 + \log\left(O^+/H^+\right) \\ &= \log\left(\frac{[\mathrm{O\,II}]\,\lambda3726 + [\mathrm{O\,II}]\,\lambda3729}{H\beta}\right) + 5.887 + \frac{1.641}{T_{O2}} \\ &\quad - 0.543 \cdot \log\left(T_{O2}\right) + 0.000114 \cdot n_e \end{aligned} \tag{12}$$

$$\begin{aligned} Z_2 &= 12 + \log\left(O^{2+}/H^+\right) \\ &= \log\left(\frac{[\mathrm{O\,III}]\,\lambda4959 + [\mathrm{O\,III}]\,\lambda5007}{H\beta}\right) + 6.1868 + \frac{1.2491}{T_{O3}} \\ &\quad - 0.5816 \cdot \log\left(T_{O3}\right) \end{aligned} \tag{13}$$

In equation (12), values for T_{O2}, the electron temperature found via [O II] emission lines, could not be accurately determined for our regions as the required 7319 Å and 7330 Å[O II] emission lines were not sufficiently observed, likely due to poor signal being too close to the end of the red-arm wavelength range. It was instead determined using the following relation given by P17:

$$T_{O2} = \frac{1.2 + 0.002 \cdot n_e + 4.2 \cdot {n_e}^{-1}}{{T_{O3}}^{-1} + 0.08 + 0.003 \cdot n_e + 2.5 \cdot {n_e}^{-1}} \tag{14}$$

also in units 10^4 K. This equation is dependent on the electron density, which in our case is derived using the [O III] electron temperature in equation (7).

Using the established approximation $O/H = O^+/H^+ + O^{2+}/H^+$ given by P17, the individual abundances of O^+ and O^{2+} determined in equations (12) and (13) may be combined into the total oxygen abundance to give a final electron temperature method metallicity:

$$12 + \log(O/H) = 12 + \log\left(10^{Z_1 - 12} + 10^{Z_2 - 12}\right) \tag{15}$$

The empirical $O32$ correction presented by Yates et al. (2020, henceforth Y20) is implemented to account for regions dominated by oxygen in the O^+ state. In this regime, errors in the determination of electron temperatures through the use of [OIII] emissions make resulting metallicities largely susceptable to underestimations. Taking the version determined using their Bayesian method, the Y20 correction was applied as follows:

$$Z_{T_e,cor} = Z_{T_e} - 0.71 \cdot (O32 - 0.29) \tag{16}$$

where $O32 = \log([\mathrm{OIII}]\lambda\lambda4959, 5007/[\mathrm{OII}]\lambda\lambda3726, 3729])$. This correction is only considered for when $O32 \leq 0.29$. Of the regions in the sample with valid direct-method integrated metallicities, four hold values of $O32$ smaller than 0.29. These are 300003198.0 (region ID 6), 300003247.0 (ID 8), 300006262.0 (ID 31), and 300009275.0 (ID 43), with $O32$ values of 0.22, −0.38, 0.08, and 0.16, respectively.

Region 300003198.0 has its initial integrated temperature-based metallicity corrected from $Z_{T_e} = 8.246$ to $Z_{T_e,corr} = 8.311$, a minor increase of 0.065 dex. Similarly, regions 300006262.0 and 300009275.0 see small increases of 0.187 and 0.101 dex, respectively. The remaining region, 300003247.0, holds a substantial increase in direct metallicity, with the correction raising its value from $Z_{T_e} = 7.881$ to $Z_{T_e,\mathrm{corr}} = 8.380$, a very substantial increase of 0.499 dex.

The results for this metallicity diagnostic as applied to the integrated-region data set can be found in Table A4. Compared to most other methods, this diagnostic was unable to be determined for a large proportion of the data set. This is primarily due to the faintness of the [O III] λ4363 emission line in our sample, which could be confidently detected in 8 of our 92 integrated-region spectra (approximately 8.7 per cent), held in predominantly low-metallicity regions within NGC 300.

4.2 The R_{23} strong emission line method

The R_{23} metallicity diagnostic is among the most frequently applied methods of

determining metallicities using strong emission lines in optical spectra. Introduced by Pagel et al. (1979), this method uses the ratio between a combination of [O II] and [O III] emission lines to the H β line, comparing values to a diagnostic curve to obtain metallicity values.

We use the R_{23} method developed by Kobulnicky & Kewley (2004), an model-driven calibration of the previous photoionization-based work of Kewley & Dopita (2002, henceforth KD02), following the process described by Poetrodjojo et al. (2021).

The emission line ratio R_{23} is defined:

$$R_{23} = \frac{[\mathrm{OII}]\,\lambda\lambda3726, 3729 + [\mathrm{OIII}]\,\lambda\lambda4959, 5007}{H\beta} \tag{17}$$

Due to the inherent issues of a strong dependence on the measured ionization parameter and a double-valued nature prevalent throughout this diagnostic, an iterative approach using multiple strong-line diagnostics in conjunction with R_{23} is used. To select which branch of the R_{23} diagnostic to apply, a rough initial metallicity is determined via the N2O2 diagnostic as outlined by KD02. This uses the emission line ratio N2O2, defined as:

$$\mathrm{N2O2} = \frac{[\mathrm{NII}]\,\lambda6583}{[\mathrm{OII}]\,\lambda\lambda3726, 3729} \tag{18}$$

which is then used in the following to find a rough estimate for metallicity:

$$\begin{aligned} Z_{N2O2} &= 1106.87 - 532.154 \cdot \mathrm{x} + 96.3733 \cdot \mathrm{x}^2 - 7.81061 \cdot \mathrm{x}^3 \\ &\quad + 0.239282 \cdot x^4 \end{aligned} \tag{19}$$

in the form of $12 + \log(O/H)$, where $\mathrm{x} = \log(\mathrm{N2O2})$. This diagnostic is favourable to obtain a good starting value due to its relatively low dependence on the ionization parameter and single-valued form above a metallicity of approximately $12 + \log(O/H) = 8$.

For a given observation, if the initial value of Z_{N2O2} was below $12 + \log(O/H) = 8.4$ that observation was assigned to the lower branch of the R_{23} diagnostic, otherwise it was assigned to the higher branch. From here, values for the degrees of ionization (q) were obtained using the following:

$$\mathrm{O3O2} = \frac{[\mathrm{O\,III}]\,\lambda\lambda4959, 5007}{[\mathrm{O\,II}]\,\lambda\lambda3726, 3729} \tag{20}$$

$$\begin{aligned} \log(q) &= 32.81 - 1.153 \cdot \mathrm{y}^2 + Z \cdot (-3.396 - 0.025 \cdot \mathrm{y} \\ &\quad + 0.1444 \cdot \mathrm{y}^2) \cdot [4.603 - 0.3119 \cdot y - 0.163 \cdot \mathrm{y}^2 \\ &\quad + Z \cdot (-0.48 + 0.0271 \cdot y + 0.02037 \cdot \mathrm{y}^2)]^{-1} \end{aligned} \tag{21}$$

where $\mathrm{y} = \log(\mathrm{O3O2})$ and with Z initially as the rough N2O2 metallicity.

The branching decision along with these values for q are then used in the following set of equations to determine R_{23} metallicity:

$$\begin{aligned} 12 + \log(O/H)_{\mathrm{lower}} &= 9.40 + 4.65 \cdot R - 3.17 \cdot R^2 - \log(q) \\ &\quad \cdot(0.272 + 0.547 \cdot R - 0.513 \cdot R^2) \end{aligned} \tag{22}$$

$$12 + \log(O/H)_{\rm upper} = 9.72 - 0.777 \cdot R - 0.951 \cdot R^2 - 0.072 \cdot R^3 - 0.811 \cdot R^4 - \log(q) \cdot (0.0737 - 0.0713 \cdot R - 0.141 \cdot R^2 + 0.0373 \cdot R^3 - 0.058 \cdot R^4) \quad (23)$$

where $R = \log(R_{23})$.

From here, an iterative procedure was established by placing the evaluated R_{23} metallicity values, derived using equation (22) or (23), back into equation (21) for ionization parameter, which was then taken to be used in a new set of metallicity determinations, and so on. The choice of branching was also allowed to change between the upper and lower branches if an intermediate metallicity value crossed the $12 + \log(\mathrm{O/H}) = 8.4$ threshold. In agreement with Poetrodjojo et al. (2021), we found that a total of three iterations were sufficient to obtain stable metallicity values.

The results for this metallicity diagnostic as applied to the integrated-region data set can be found in Table A4, where 91 of the 92 confirmed regions (99 per cent) held valid integrated metallicities.

4.3 The N2O2 method

Having already determined the N2O2 metallicity as an intermediate step in the R_{23} method above, the same method (i.e. equations (18) and (19) as defined by KD02) were again used to evaluate metallicity here. Again, the methods used by KD02 made use of stellar population synthesis and photoionization models to develop abundance diagnostics.

It should be noted that this diagnostic is only valid in the metallicity range $12 + \log \mathrm{O/H} > 8.35$, being the lowest metallicity sampled in the H II region data set which was used to first calibrate this method by Zaritsky, Kennicutt & Huchra (1994). The results for this metallicity diagnostic as applied to the integrated-region data set can be found in Table A4, where 81 out of the 92 confirmed regions (88 per cent) held valid integrated metallicities.

4.4 The N2S2 method

This method features a ionization-parameter dependence much like that previously observed in the R_{23} method. This is managed in much the same way, by implementing an iterative method across both the N2S2 metallicity diagnostic and the [O III]/[O II] ionization parameter diagnostic concurrently. The initial rough metallicity values were determined by the [N II]/[O II] diagnostic, in much the same way as previously found through the R_{23} method. This rough metallicity value again allowed for the determination of an ionization parameter through O3O2, which could be used to select the [N II]/[S II] diagnostic curve, and then iterated through to achieve a stable metallicity result.

As outlined by KD02, this diagnostic uses the ratio:

$$\mathrm{N2S2} = \frac{[\mathrm{N\,II}]\,\lambda 6583}{[\mathrm{S\,II}]\,\lambda\lambda 6716, 6731} \quad (24)$$

in conjunction with a series of fourth-degree ionization-parameter-dependent diagnostic polynomials (coefficients given by the authors), again based on stellar population synthesis and photoionization modelling. An upper metallicity limit was set at $12 + \log(\mathrm{O/H}) = 9.25$ (determined metallicities higher than this were set to equal this value), as this is the point where the diagnostic polynomials begin to turn over (see KD02 Fig. 4). Uncertainties in these metallicity values were also evaluated using a Monte Carlo procedure. This diagnostic is valid within the metallicity range $8.3 < 12 + \log(\mathrm{O/H}) < 9.2$.

The results for this metallicity diagnostic as applied to the integrated-region data set can be found in Table A4, where 49 out of the 92 confirmed regions (54 per cent) held valid integrated metallicities.

4.5 The N2H α method

This metallicity method is outlined by Pettini & Pagel (2004, henceforth PP04) as a prelude to their O3N2 diagnostic, and is based on photoionization models. It is simple in form, evaluating a result for metallicity using only the emission line ratio $\mathrm{N2H}\,\alpha = [\mathrm{N\,II}]\,\lambda 6583 / \mathrm{H}\alpha$ in the third-degree polynomial equation:

$$12 + \log(\mathrm{O/H}) = 9.37 + 2.03 \cdot \mathrm{x} + 1.26 \cdot \mathrm{x}^2 + 0.32 \cdot \mathrm{x}^3 \quad (25)$$

where $\mathrm{x} = \log(\mathrm{N2H}\,\alpha)$. This diagnostic is included here for completeness, as it is to be directly expanded on in Section 4.7 below. Metallicities here are valid within the range $7.2 < 12 + \log(\mathrm{O/H}) < 8.7$.

The results for this metallicity diagnostic as applied to the integrated-region data set can be found in Table A4, where 72 out of the 92 confirmed regions (78 per cent) held valid integrated metallicities.

4.6 The N2S2H α method

This method, as given by Dopita et al. (2016), incorporates both the N2S2 and N2H α methods into a diagnostic which is both metallicity sensitive and ionization independent, and is also based on photoionization modelling. Here, emission line ratios N2S2 and N2H α are as defined above in equations (24) and (25), respectively. These ratios are combined and incorporated to determine metallicity values by the authors using:

$$\mathrm{y} = \log(\mathrm{N2S2}) + 0.264 \cdot \log(\mathrm{N2H}\alpha) \quad (26)$$

$$12 + \log(\mathrm{O/H}) = 8.77 + \mathrm{y} + 0.45 \cdot (\mathrm{y} + 0.3)^5 \quad (27)$$

This method produces metallicity values which are valid between $7.5 < 12 + \log(\mathrm{O/H}) < 9.4$.

The results for this metallicity diagnostic as applied to the integrated-region data set can be found in Table A4, where all 92 confirmed regions (100 per cent) held valid integrated metallicities.

4.7 The O3N2 method

As an improvement upon the previous N2H α method, PP04 proposed the use of a new ratio:

$$\mathrm{O3N2} = \frac{[\mathrm{O\,III}]\,\lambda 5007 / \mathrm{H}\beta}{[\mathrm{N\,II}]\,\lambda 6583 / \mathrm{H}\,\alpha} \quad (28)$$

with the work of Marino et al. (2013) calibrating this ratio using temperature-based H II region metallicity data using the following:

$$12 + \log(\mathrm{O/H}) = 8.533 - 0.214 \cdot \log(\mathrm{O3N2}) \quad (29)$$

Metallicities determined through this diagnostic are valid within the range $8.2 < 12 + \log(\mathrm{O/H}) < 8.8$.

The results for this metallicity diagnostic as applied to the integrated-region data set can be found in Table A4, where 79 out of the 92 confirmed regions held valid integrated metallicities (86 per cent).

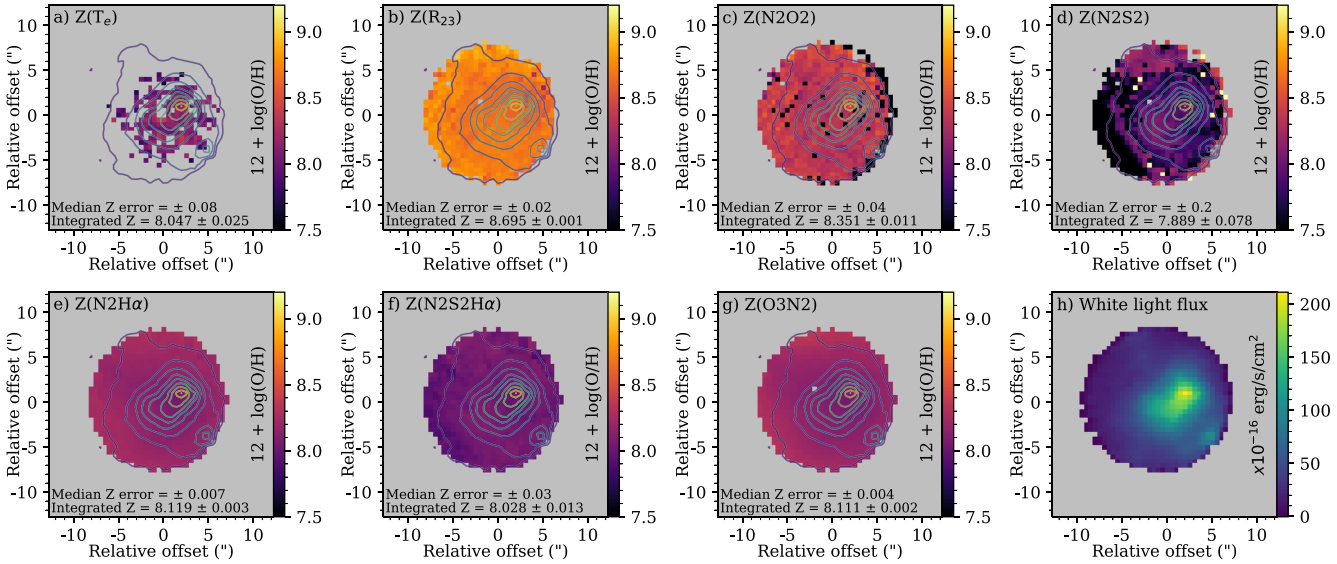

Figure 8. Spatially resolved metallicity maps (panels a–g) of SAMI Zoom HII region 300002271.0, displayed using the same colour map scaling to emphasize disparities. Corresponding metallicitiy measurements determined using the integrated region data set are given below each map. Also shown is a white light flux map displaying the form of the region (panel h), which is also used for the contours across the metallicity maps at the same colour scaling.

4.8 Other methods

Apart from the methods addressed in this work, other empirical approaches to metallicity evaluation exist that are widely used today. These include Pilyugin & Thuan (2005), mentioned earlier as PT05, which worked to improve and recalibrate strong-line abundance methods using many observations of H II regions with well-defined λ4363 emissions and derived electron temperature metallicities. Other prevalent methods include the S-calibration and R-calibration put forward by Pilyugin & Grebel (2016), which again uses measured T_e metallicities of H II regions to refine strong emission line abundance relations and are applicable to low- and high-metallicity regimes, and the work of Curti et al. (2017) who similarly applied empirical calibrations to many SEL-based diagnostics using observations of SDSS galaxies.

We do not evaluate metallicities using these methods here as it is outside the scope of this study. However, it is important to note that including further empirical calibrations would help limit biases and improve results by accounting for a broader range of observational conditions. This would reduce reliance on theoretical or model-based assumptions, such as the quantities and geometric structures of electron temperature and ionization throughout observed HII regions.

4.9 Evaluating uncertainties

As it is difficult to produce a formal error propagation through the complex system of equations required in each method, the uncertainties for all metallicity measurements were determined by applying a Monte Carlo technique. For each, a series of 100 concurrent metallicity determinations were conducted using identical methods to those established above, each drawing a separate set of emission line flux values sampled using normal distributions with means equal to the respective flux values of their relevant lines and standard deviations equal to the corresponding flux uncertainties. In every case, metallicity values from each set of Monte Carlo iterations formed a normal distribution in terms of 12 + log(O/H). This is also true for electron density and temperature measurements in the direct method, which also displayed well-ordered normal distributions across iterated values.

5 DISCUSSION

5.1 Disparity

Due to their differences in methodology, comparisons between the results of T_e- and SEL-method determinations, as well as between SEL methods using differing forms of calibration, are difficult at best. In their paper, Kewley & Ellison (2008) showed the disparity between metallicity diagnostics may span almost an order of magnitude in terms of relative oxygen abundance. Furthermore, the work by López-Sánchez et al. (2012) highlights additional considerations in comparing abundance determinations, noting that the abundances determined solely from electron temperatures lose viability at lower metallicities (12 + log(O/H) < 8), while SEL methods that do not account for the ionization parameter are susceptible to substantial variability and error. Further details on these methods and their limitations are also provided in the appendix of López-Sánchez & Esteban (2010).

Significant disparities were seen across the SAMI Zoom sample in both the spatially resolved and integrated data sets. An example of this is shown in Fig. 8, where spatially resolved metallicity maps are displayed on the same colour scale accompanied by corresponding integrated-region measured values underneath. The full list of measured integrated-region metallicities across the SAMI Zoom sample can be found in Table A4, with all produced spatially resolved metallicity maps published online (see Section 6). Unobserved states of ionization throughout these regions may contribute to these differences. These may be reconciled using ratios of excited helium and measured oxygen abundances (Izotov et al. 2006), though none of the regions within the integrated data set could present the He II λ4686 detections required to make such corrections.

To quantify the behaviour and extent of the metallicity discrepancies in the SAMI Zoom data set, a fiducial method was selected to be a comparison point against the remaining. Here, the R_{23}

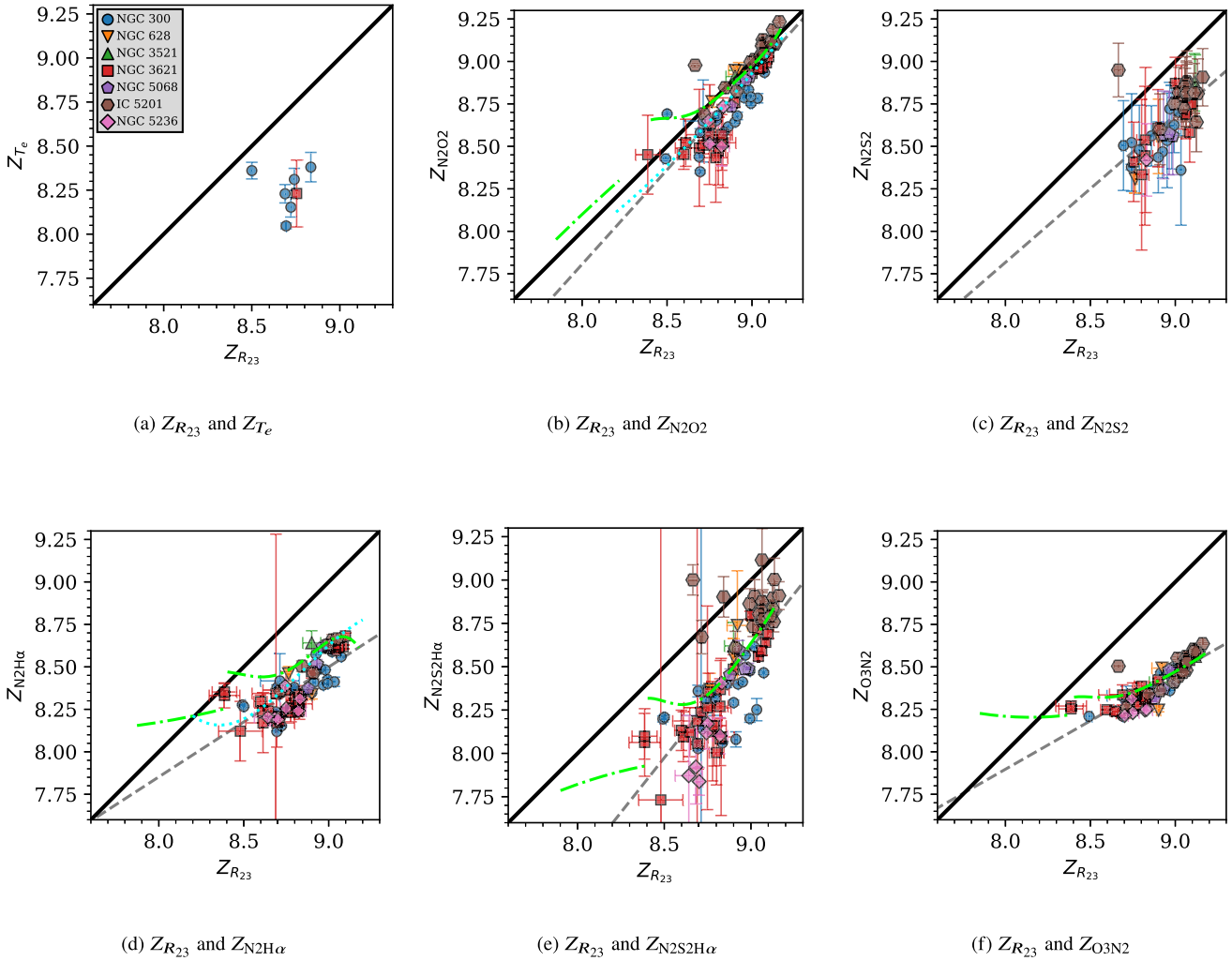

(a) $Z_{R_{23}}$ and Z_{T_e} (b) $Z_{R_{23}}$ and Z_{N2O2} (c) $Z_{R_{23}}$ and Z_{N2S2}

(d) $Z_{R_{23}}$ and $Z_{\mathrm{N2H}\alpha}$ (e) $Z_{R_{23}}$ and $Z_{\mathrm{N2S2H}\alpha}$ (f) $Z_{R_{23}}$ and Z_{O3N2}

Figure 9. Comparisons between metallicities determined by the R_{23} method and the six other methods in this study using the integrated H II region spectra (values shown in Table A4). In each plot, a 1:1 comparison line is shown as a solid line. For comparisons utilizing SEL-method metallicities, a trend line determined by linear regression through an iterative Monte Carlo method is plotted as the dashed line, with parameters described in Table 4. Data points represent all pairings of valid metallicity measurements (i.e. within the calibrated ranges of each as stated in Section 4) with at least a 3σ confidence in either method. Points are styled to distinguish between H II regions in different host galaxies, as specified in the legend on panel a. The conversions between diagnostics given by Scudder et al. (2021) using a Milky Way type dust correction are shown dash–dotted for panels b, d, e, and f. Conversions given by Kewley & Ellison (2008) are shown as a dotted line in panels b and d.

metallicity was chosen as such due to its prevalence in the literature and its dependence on relatively strong emission lines. Comparisons between pairings of the R_{23} metallicity and measurements using the other methods were then developed, with the results shown in Fig. 9 and Table 4. To robustly contrast between methods, a linear trend is fitted to the data. Due to the presence of errors across both axes, each metallicity–metallicity trend is constructed using basic linear regression through a Monte Carlo method of 10 000 iterations while altering the metallicity data with respect to their standard error.

Each case shows significant differences between the metallicities derived from each pairing of methods. Between the fiducial R_{23} and the direct electron temperature metallicities, discrepancies of up to 0.65 dex in oxygen abundance were seen with an average deviation of 0.46 dex, with the direct method showing systematically lower metallicities across our regions. A contributing factor to this discrepancy may be the estimation of electron temperatures throughout separate ionization zones of each H II region; these are generally divided into an O^+ zone and an O^{2+} zone, each with temperatures that must be determined individually. As auroral lines are difficult to observe, particularly in high-metallicity samples including SAMI Zoom, the temperature of the O^+ zone is estimated using a correction in terms of the O^{2+} temperature (equation (14)). This may introduce error due to existing states of ionization within regions which were unobserved; Hägele et al. (2008) estimates this effect underestimates direct-method metallicities by up to 0.2 dex, though this may be exacerbated in our analysis by the use of the integrated-region sample. This would be remedied by a more comprehensive determination of the electron temperatures using a larger assortment of auroral lines (Kewley et al. 2019 lists [O II], [S II], [S III], and [N II] to compliment [O III]), which would require deeper observing of these regions to resolve. It should also be noted that this comparison held a significantly lower amount of valid data points compared to subsequent ones with a total of seven comparable metallicity pairings (six from host galaxy NGC 300 and a singular point from NGC 3621). A linear trend to the comparative data between these two methods is not attempted as the data is not complete enough to form a reliable analysis in this case.

Table 4. Various quantified parameters relating to the comparisons between SEL-method metallicity diagnostics as shown in Fig. 9. The slope and intercept values are that of the linear trends determined between each pairing of metallicities through an iterative Monte Carlo method along with corresponding correlation coefficient (r^2) values. Also shown are the amounts of scatter measured in each trend line and the mean deviations from the 1:1 comparison line for each pairing.

Diagnostic pair	Trend gradient	Trend intercept	Trend r^2 value	Trend residual 3σ scatter	1:1 mean deviation
$Z_{R_{23}}$ and Z_{N2O2}	1.111 ± 0.085	-1.08 ± 0.77	0.73	0.36	0.12
$Z_{R_{23}}$ and Z_{N2S2}	0.87 ± 0.25	0.9 ± 2.3	0.42	0.39	0.32
$Z_{R_{23}}$ and $Z_{\mathrm{N2H}\alpha}$	0.65 ± 0.11	2.67 ± 0.91	0.56	0.30	0.44
$Z_{R_{23}}$ and $Z_{\mathrm{N2S2H}\alpha}$	1.26 ± 0.39	-2.8 ± 3.5	0.58	0.62	0.44
$Z_{R_{23}}$ and Z_{O3N2}	0.570 ± 0.030	3.34 ± 0.27	0.73	0.19	0.49

Stronger observations of auroral [O III] is required to obtain further robust measurements of direct metallicity for such investigation.

Further regarding ionization zones, an issue may arise within regions not fully contained within observational fields of view. That is, partial coverage of a HII region may partially or entirely exclude ionization zones leading to inaccurate measurements of electron temperature metallicity. While many regions in our sample are only partially observed (for example, see Fig. A1 regions such as IDs [35] and [60] among others), all regions with measured electron temperatures are well contained within their respective field of view boundaries.

The remaining comparisons display evident positive correlations, each more-or-less following the fiducial R_{23} metallicities however to varying limitations. Kewley et al. (2019) note that discrepancies between SEL diagnostics remain substantial, despite many years of improving data sets. In the case of the comparison with the N2O2 method, another photoionization-based approach however calibrated using different data sets (Kewley & Dopita 2002; Kobulnicky & Kewley 2004), the two approach a convergence at higher metallicities (approx. $Z > 9$) yet increasingly diverge towards lower values with the N2O2 method producing progressively smaller metallicities as either form decrease. This comparison returned the smallest mean deviation across the pairings of methods of 0.12 dex across the sampled range, and a maximum deviation of 0.35 dex. In terms of an apparent trend, the two are clearly positively correlated along a constructed trend line, with a moderate degree of scatter. Furthermore, the two metallicities are seen to increase at a similar rate with a trend gradient of 1.11 (as a gradient of one would signify a 1:1 conversion).

The comparison with N2S2 metallicity, a further photoionization-based method seen in Kewley & Dopita (2002), follows a similar pattern albeit with a larger mean deviation from the comparison line of 0.32 dex. This paring does not reach a convergence as the previous did, rather its comparison shows a steady offset with a trend line gradient fairly close to one, similar to the previous. This pairing showed a higher degree of scatter across the sample range however, holding a moderately correlated trend line. Comparisons between the R_{23} method and each of the N2Hα and N2S2Hα methods, approaches calibrated using separate instances of photoionization modelling by Pettini & Pagel (2004) and Dopita et al. (2016) respectively, each produced positively correlated trends with mean deviations of 0.44 in either case. Each of these two comparisons again showed a predominantly larger R_{23} metallicity yield, following moderately offset linear trends yet seemingly turning up towards the one-to-one comparison lines at higher metallicities (approx. $Z > 9$).

Regarding N2S2, N2Hα, and N2S2Hα metallicities, the effects of diffuse ionized gas (DIG) throughout H II regions may introduce inaccuracies in these metallicity determinations (Sanders et al. 2017; Mannucci et al. 2021). Light from these gasses may contaminate observations if they are not sufficiently resolved, particularly impacting metallicity diagnostics which utilize the emission line ratios [N II]/Hα and [N II]/[S II], causing overestimations in these determinations (Kewley et al. 2019). The extent of any such overestimations is unclear in our sample, however, as these three diagnostics generally produced lower metallicity values when compared to the R_{23} method. To address this, a thorough investigation using the spatially resolved data set to isolate H II regions from any potential DIG contamination could be conducted.

Table 5. Host galaxy physical properties used to determine deprojected HII region galactocentric radii, obtained from the HyperLeda database (Makarov et al. 2014, available at https://leda.univ-lyon1.fr/).

Host Galaxy	PA (deg)	I (deg)	D (Mpc)	R_{25} (arcmin)
NGC 300	113.2	48.5	1.979	9.75
NGC 628 (M74)	0.0	19.8	10.093	5.00
NGC 3521	162.8	60.0	13.552	4.16
NGC 3621	161.7	67.6	6.310	4.77
NGC 5068	0.0	27.3	5.152	3.71
NGC 5236 (M83)	0.0	15.3	4.898	6.74
IC 5201	24.3	66.6	10.864	3.38

Lastly, the comparison with the O3N2 metallicity diagnostic shows the most tightly correlated linear trend between pairings of methods, forming a trend line with a relatively low 3σ residual scatter of 0.19 dex. Calibrated using temperature-based H II region metallicity data (Marino et al. 2013), a unique feature within SEL methods tested in this analysis, the comparison between this and the fiducial R_{23} metallicity holds the largest mean deviation of 0.49 dex, as well as the most divergent comparative trend line gradient with a value of 0.570 ± 0.030. This signifies that as the determined value of R_{23} metallicity increases, corresponding O3N2 metallicities differ to both the greatest extent and at the fastest rate among the SEL diagnostics analysed in this study.

Where possible, the Fig. 9 plots include the metallicity-to-metallicity conversions developed by Scudder et al. (2021, henceforth S21), drawn as green dash–dotted curves. There, the authors use approximately 1.1 million star-forming spectra from the MaNGA survey to determine fifth-degree polynomial fits to relate pairings of metallicity methods. The direct electron temperature method and the N2S2 method are not included in this study. In some cases, upper- and lower-branch polynomials are given by the authors with individual polynomials assigned to each, breaking at a specified metallicity to more accurately fit their data sample. Also plotted are the applicable conversions by Kewley & Ellison (2008), drawn as cyan dotted curves in Fig. 9.

In the case of the R_{23} to N2O2 metallicity comparison, the respective S21 polynomial matches well with the data of this work. This can be seen particularly well with the IC 5201 data points (brown

Table 6. Measured continuous metallicity gradients of three of the seven host galaxies within the SAMI Zoom Survey, using metallicity diagnostics for which there were at least five valid data points (N) to construct a linear trend. Gradients for NGC 3521, NGC 5068 and NGC 628, as well as those utilising the metallicity methods in this analysis not included below, could not be determined due to this constraint. The gradients of NGC 3621 were measured with a break at 1 R_{25}, and are given in Table 7. Gradients are plotted in Fig. 10, with more detailed views across Figs A2, A4, and A5. Correlation coefficient (r^2) values are also provided.

Host Galaxy	Method	N	Slope (dex $R_{25}{}^{-1}$)	Intercept (12 + log(O/H))	r^2 value
NGC 300	Z_{T_e}	6	-0.59 ± 0.23	8.72 ± 0.22	0.63
	$Z_{R_{23}}$	24	-0.300 ± 0.049	9.021 ± 0.029	0.64
	Z_{N2O2}	23	-0.456 ± 0.047	8.915 ± 0.021	0.82
	Z_{N2S2}	13	-0.368 ± 0.060	8.674 ± 0.038	0.78
	$Z_{\mathrm{N2H}\alpha}$	25	-0.313 ± 0.040	8.528 ± 0.023	0.73
	$Z_{\mathrm{N2S2H}\alpha}$	24	-0.511 ± 0.044	8.577 ± 0.023	0.86
	Z_{O3N2}	20	-0.189 ± 0.047	8.456 ± 0.023	0.48
IC 5201	$Z_{R_{23}}$	7	-0.138 ± 0.044	8.831 ± 0.025	0.67
	$Z_{\mathrm{N2H}\alpha}$	7	-0.129 ± 0.037	8.323 ± 0.021	0.72
	$Z_{\mathrm{N2S2H}\alpha}$	7	-0.55 ± 0.12	8.413 ± 0.057	0.81
	Z_{O3N2}	5	-0.044 ± 0.031	8.261 ± 0.016	0.41
NGC 5236 (M83)	$Z_{R_{23}}$	23	-0.232 ± 0.054	9.188 ± 0.032	0.47
	Z_{N2O2}	23	-0.246 ± 0.038	9.194 ± 0.023	0.67
	Z_{N2S2}	18	-0.126 ± 0.069	8.863 ± 0.038	0.17
	$Z_{\mathrm{N2H}\alpha}$	23	-0.314 ± 0.053	8.951 ± 0.040	0.63
	$Z_{\mathrm{N2S2H}\alpha}$	23	-0.096 ± 0.047	8.871 ± 0.030	0.17
	Z_{O3N2}	23	-0.184 ± 0.032	8.620 ± 0.022	0.62

Table 7. The measured metallicity gradients of NGC 3621 featuring a break at 1 R_{25}, again given where possible following the condition of at least five valid metallicity-radius data points. These are plotted together in Fig. 10b, with a more detailed view within Fig. A3 accompanied by literature comparisons. Correlation coefficient (r^2) values for the inner segments are also provided.

		Inner disc ($R < R_{25}$)				Outer disc ($R > R_{25}$)	
Host Galaxy	Method	N	Slope (dex $R_{25}{}^{-1}$)	Intercept (12 + log(O/H))	r^2 value	N	Mean (12 + log(O/H))
NGC 3621	$Z_{R_{23}}$	8	-0.62 ± 0.14	9.231 ± 0.055	0.77	19	8.70 ± 0.14
	Z_{N2O2}	8	-0.44 ± 0.13	9.105 ± 0.044	0.68	11	8.500 ± 0.044
	Z_{N2S2}	7	-0.42 ± 0.25	8.85 ± 0.11	0.37	3	8.440 ± 0.084
	$Z_{\mathrm{N2H}\alpha}$	8	-0.56 ± 0.17	8.787 ± 0.066	0.65	19	8.256 ± 0.069
	$Z_{\mathrm{N2S2H}\alpha}$	8	-0.42 ± 0.24	8.784 ± 0.088	0.34	17	8.14 ± 0.14
	Z_{O3N2}	7	-0.194 ± 0.094	8.568 ± 0.035	0.46	14	8.286 ± 0.046

hexagons) at metallicities of $Z_{R_{23}} > 8.7$. The values from other host galaxies in this range also match relatively well, though the S21 polynomial predicts higher values of N2O2-method abundances by approximately 0.1 to 0.2 dex. Conversely the polynomial turns off at lower metallicities, predicting progressively larger discrepancies as metallicity decreases.

A similar form can be seen in the comparisons of R_{23} metallicity with both the N2S2Hα and O3N2 methods. In either case, the S21 polynomials match SAMI Zoom comparison data very well at high metallicities, turning off the grey dashed line from approximately $Z_{R_{23}} < 8.7$. The comparison with N2Hα metallicity however shows the largest difference. Here, the S21 polynomial predicts significantly higher N2Hα metallicities for given R_{23} metallicities across the large majority of SAMI Zoom data points and indeed when contrasting against the constructed linear trend line. Data points are seen trending towards matching with the S21 polynomial at high metallicities (around $Z_{R_{23}} = 9$), though this is only a small proportion.

These discrepancies between this work and the conversions given by S21 may be driven by differences in the sample selection of the two data sets. The S21 polynomials draw from a much larger sample of star-forming regions in MaNGA using which they may construct higher-degree conversions between the diagnostics.

5.2 Metallicity gradients

Radial metallicity gradients for the seven SAMI Zoom host galaxies were constructed by applying weighted linear regression fits to data points representing the deprojected galactocentric distances (calculated using the parameters in Table 5) and integrated metallicities of the relevant regions within each galaxy. These regressions were weighted with respect to the inverse standard error on metallicity. Here, distances are represented in the form R_{GC}/R_{25}, the ratio of the derived galactocentric radii to the host galaxy isophotal radius at a B-band surface brightness of 25$^{\mathrm{th}}$ magnitude.

The measured gradients are listed in Tables 6 and 7, and are shown graphically in Fig. 10. We only consider gradients for which there are at least five valid measurements that may be used to construct a trend between radius and metallicity. These gradients are also shown independently within Figs A2 to A5, plotted in terms of R_{GC}/R_{25}, with accompanying comparisons with literature gradients as well as data points calculated using the methods outlined in Section 4 on respective literature flux values and ratios.

Previous works have identified the presence of non-linearity, breaks, or discontinuities in the gradients of these host galaxies. An example of this may be seen in the work of Bresolin et al. (2009a) which details a considerably flatter gradient within the outer regions

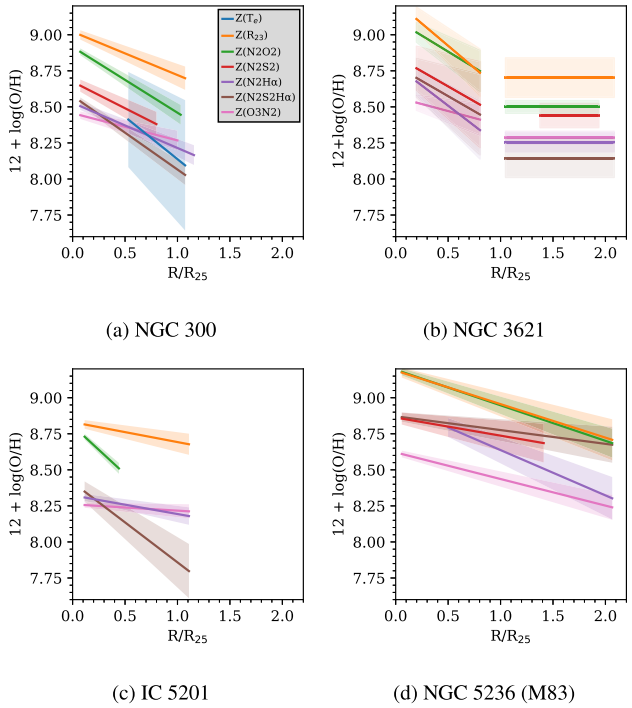

(a) NGC 300 (b) NGC 3621

(c) IC 5201 (d) NGC 5236 (M83)

Figure 10. The set of measured metallicity gradients for each host galaxy determined in the integrated-region study, as listed in Tables 6 and 7. Gradients are distinguished by metallicity method as indicated by the legend shown in panel 10(a), with 1σ uncertainty bands also shown around each line. Detailed versions of these plots as well as literature comparisons are shown in Figs A2 to A5.

(of radii R > R$_{25}$) within NGC 5236 (M83), forming a discontinuity in the abundance gradient. Also, a similar result from Bresolin et al. (2012) shows such features for host galaxy NGC 3621. Unfortunately the regions within the SAMI Zoom data for NGC 5236 do not extend past R$_{25}$ sufficiently enough to distinguish a possible break. We do however observe regions of sufficient radial extent within NGC 3621, showing a gradient break at R$_{25}$ in the data.

5.2.1 *NGC 300*

NGC 300 had derivable gradients for each of the seven metallicity diagnostics applied, to varying extents of quality. Metallicities derived using the direct electron temperature method formed a radial gradient of slope -0.59 ± 0.23 dex R$_{25}{}^{-1}$ and an intercept (central metallicity) of $12 + \log(\mathrm{O/H}) = 8.72 \pm 0.22$; these values held the largest errors of their respective properties across the whole study, leading to a gradient with comparably large uncertainties. On the other hand, gradients constructed using SEL methods produced clearer negative trends, beginning at central metallicity values (trend intercepts) of $12 + \log(\mathrm{O/H}) = 8.456$ (O3N2) to 9.021 (R_{23}). These also varied in slope magnitude; the O3N2 diagnostic provided the shallowest gradient for NGC 300 of -0.188 ± 0.047 dex R$_{25}{}^{-1}$, with the steepest SEL gradient here being -0.511 ± 0.044 dex R$_{25}{}^{-1}$ obtained through the use of the N2S2Hα diagnostic. Gradient intercepts also differed, ranging from central metallicity values of 8.456–9.021 (corresponding to gradients via the O3N2 and R_{23} methods, respectively) in terms of $12 + \log(\mathrm{O/H})$, a range of 0.565 dex. This was also the only host galaxy in the sample with a determinable direct-method abundance gradient.

When compared to gradients developed within previous literature, a variety of agreements and disagreements can be seen. Considered here are the past findings of Bresolin et al. (2009b), Stasińska et al. (2013), and Toribio San Cipriano et al. (2016), who constructed gradients each utilizing direct-method metallicities, as well as McLeod et al. (2021) using the N2Hα method. The three direct-method data sets agree particularly well between each other, finding gradients of $-0.41 \cdot \mathrm{R/R_{25}} + 8.57$, $-0.361 \cdot \mathrm{R/R_{25}} + 8.48$, and $-0.3 \cdot \mathrm{R/R_{25}} + 8.48$, respectively. The SAMI Zoom direct-method gradient did produce fairly comparable results, with the relevant data points being tentatively consistent with the literature gradients as well as having the Bresolin et al. (2009b) slope and intercepts within respective 1σ error margins. However, errors of ± 0.23 and ± 0.22 respectively are considerably large, making this window of consistency less definitive. Unfortunately, we do not sample enough NGC 300 H II regions with determinable direct-method metallicities at lower galactocentric radii (<0.5 R$_{25}$) to sufficiently measure a gradient across the entire disc of the galaxy.

As for the N2Hα-method results, the SAMI Zoom gradient of $-0.313(\pm 0.040) \cdot \mathrm{R/R_{25}} + 8.528(\pm 0.023)$ is somewhat comparable to the McLeod et al. (2021) result of $-0.25(\pm 0.04) \cdot \mathrm{R/R_{25}} + 8.50(\pm 0.01)$; though SAMI Zoom finds a slightly steeper gradient and higher intercept value, the two variables are somewhat consistent with the literature result as they differ by approximately 1.2 and 1.6 standard error values, respectively. Notably, the range of radius values covered by McLeod et al. (2021) is significantly smaller than the SAMI Zoom data set, covering the galactic disc out to a radius of 0.43 R$_{25}$ due to the field of view of the MUSE instrument. Taking this into account and re-fitting the SAMI Zoom radius-metallicity data only using the 9 regions out to this radius results in a gradient of $-0.16(\pm 0.28) \cdot \mathrm{R/R_{25}} + 8.500(\pm 0.059)$ (with correlation coefficient $r^2 = 0.05$), a significantly worse fit to the data due to the large amount of scatter in this portion of the data set.

5.2.2 *NGC 3621*

Within this study, metallicity gradients for NGC 3621 uniquely follow a broken profile featuring a negatively sloped relation from the centre of the galaxy out to the effective radius (R$_{25}$), followed by a flat outer-disc profile with zero slope. The emergence of this form follows literature precedent, with the work of Bresolin et al. (2012) utilising numerous high quality spectra to identify the flattened disc of this galaxy past 1 R$_{25}$ with very little scatter in metallicity across the outer radii.

Gradients were able to be constructed for all six SEL metallicity diagnostics in this study within NGC 3621; however, there was insufficient data to do so for the direct electron temperature method. We employ the same linear regression method described earlier in Section 5.2 to derive these gradients within R$_{25}$, producing slopes and intercepts characterizing the inner regions. For outer-galaxy radii, we assume a constant profile represented by the error-weighted mean metallicity past R$_{25}$.

Inner SEL-method gradients are well defined with numerous regions either side of the breaks. Gradients hold slopes between -0.194 ± 0.094 (O3N2) and -0.62 ± 0.14 (R_{23}) in terms of dex R$_{25}{}^{-1}$. The N2O2, N2S2, and N2S2Hα methods show strong agreement in slope, differing by only 0.02 dex R$_{25}{}^{-1}$. Inner-gradient intercepts span values of $12 + \log(\mathrm{O/H}) = 8.568 \pm 0.035$ (O3N2) to 9.231 ± 0.055 (R_{23}).

Beyond R_{25}, all six metallicity–radius profiles clearly flatten, though with varying degrees of scatter. The weighted mean metallicity values for the outer regions range from $12 + \log(O/H) = 8.14 \pm 0.14$ (N2S2Hα) to 8.70 ± 0.14 (R_{23}). These two methods also show the greatest amount of scatter (1σ standard deviation) across these outer regions.

To confirm that broken metallicity gradients are preferred in these cases, unbroken gradients were applied (using the same method as NGC 300 above) to compare. Results of this comparison are provided in Table A5. All six unbroken SEL-method gradients produced worse residuals, calculated as the absolute differences between the new fitted gradients and the metallicity–radius data points. The total residuals for these unbroken profiles are consistently larger, ranging from 0.149 to 1.151 dex higher than their broken-gradient counterparts, supporting the preference for a break at $1\,R_{25}$ for this galaxy.

We compare our results to the work of Bresolin et al. (2012, henceforth B12), who used the R_{23}-based McGaugh (1991, M91) and N2-based Pettini & Pagel (2004) methods to derive gradients with a break at R_{25}. Their N2-based gradient of $-0.51 \cdot R/R_{25} + 8.73$ and outer mean metallicity of $12 + \log(O/H) = 8.23$ align well with our SAMI Zoom N2Hα gradient of $-0.56 \cdot R/R_{25} + 8.787$ and outer mean metallicity of 8.256. Comparisons of R_{23} gradients are less applicable due to different methodologies. While B12 uses the M91 method, we apply the approach given by Kobulnicky & Kewley (2004) which rescales R_{23} metallicities by averaging M91 and KD02 results. The B12 R_{23} gradient has a slope of $-0.62\,\mathrm{dex}\,R_{25}^{-1}$ and an intercept of $12 + \log(O/H) = 9.09$ with an outer mean of 8.59. This slope matches our SAMI Zoom result of $-0.62\ \mathrm{dex}\,R_{25}^{-1}$; however, we find a much higher intercept (9.231) and outer mean (8.70) demonstrating the aforementioned difference in underlying procedure. A similar comparison with Ryder (1995), who used the R_{23} calibration from Zaritsky et al. (1994), shows good agreement in slope ($-0.65\,\mathrm{dex}\,R_{25}^{-1}$) but a lower intercept of $12 + \log(O/H) = 8.92$, further emphasizing disparities.

5.2.3 IC 5201

Four metallicity gradients were able to be constructed for the host galaxy IC 5201 as the direct, N2O2, and N2S2 methods held insufficient data. We find derived gradient slopes for this galaxy ranging between -0.044 and $-0.55\,\mathrm{dex}\,R_{25}^{-1}$ and central metallicities between $12 + \log(O/H)$ values of 8.273 and 8.841, a range of 0.568 dex in oxygen abundance.

We compare these findings with the past work of Ryder (1995, henceforth R95), who determined the gradient of this galaxy using the R_{23} method as $-0.14 \cdot R_{25} + 8.64$. In terms of gradient slope value, the SAMI Zoom R_{23} method matches considerably well, holding a value of $-0.148\,\mathrm{dex}\,R_{25}^{-1}$. However, the intercept values between the two vary a fair amount, differing by approximately 0.2 dex in oxygen abundance with the SAMI Zoom data set producing larger R_{23} metallicities. This may be a result of systematic differences between the methodologies used between this work and that of R95, with the latter selecting the metallicity method of Zaritsky et al. (1994).

One thing to note, while the three other host galaxies in this study consistently had gradients constructed using large numbers of data points, each gradient for IC 5201 has been developed using at most 7 points. While this is noticeably lower than the majority of the gradients within other host galaxies, the high correlation and low general scatter within the radius-metallicity data points across IC 5201 indicate well-defined gradients across the sampled radii.

5.2.4 NGC 5236 (M83)

NGC 5236 was able to be characterized by metallicity gradients using the six SEL methods addressed by this work. Of these, gradient slope values ranged between -0.096 and $-0.314\,\mathrm{dex}\,R_{25}^{-1}$, from the N2S2H$\alpha$ and N2Hα methods, respectively. Central metallicities varied between $12 + \log(O/H)$ values of 8.620 using O3N2 and 9.194 using N2O2. Gradients were relatively well defined, however a concentration of regions with radii of approximately $0.5\,R_{25}$ showed a large spread in metallicity in some cases, causing fitted trend r^2 values to decline. This was particularly visible for the N2Hα and N2S2Hα methods, which produced metallicities spanning approximately 0.4 dex in oxygen abundance (excluding the high-metallicity outlier point) within this small radius range alone.

A previous gradient for this host galaxy was determined by Grasha et al. (2022, henceforth G22) using the N2O2 diagnostic, presenting as $-0.075 \cdot R_{25} + 9.131$. The SAMI Zoom gradient determined in this work differs significantly from the G22 result, showing a much steeper negative slope of -0.246 ± 0.038 and a higher central metallicity value of $12 + \log(O/H) = 9.194 \pm 0.023$. These may be seen within Fig. A5b. The discrepancy may be a result of a the radius ranges sampled in either study; the G22 sample contained H II regions fairly uniformly between radii of approximately 0.25 to $1.5\,R_{25}$ [see Grasha et al. 2022; fig. 13(e)], whereas the SAMI Zoom Survey sampled a large amount of regions close to $0.5\,R_{25}$ and only a few either side. The three SAMI Zoom regions past R_{25} also drive the determined gradient slightly steeper, as do the lowest-radius points with high metallicity; while the G22 sample does have regions towards these areas, they do not contribute as much to a steeper gradient due to the presence of additional data points at these radii. The G22 data points within Fig. A5, derived in this work using their reported emission line data in an identical metallicity analysis (Section 4), also show inconsistencies when compared to the SAMI Zoom data. This is primarily at both low galactocentric radii (approx. 0 to $0.2\,R_{GC}$) and high radii ($>1\,R_{GC}$). Due to the small amount of SAMI Zoom data points in these areas, this may simply be a sampling or selection effect. The main concentration of SAMI Zoom data points positioned around $0.5\,R_{GC}$ does appear offset from the G22 data in some cases, largely while using R_{23} and O3N2 metallicities where they report much shallower gradients. A broader sampling of radii either side of the $0.5\,R_{GC}$ grouping of regions would greatly help to clarify these effects.

Another measurement for the gradient of this galaxy is given by Della Bruna et al. (2022) using the N2Hα method, presented as $-0.10(\pm0.033)R/R_e + 8.88(\pm0.016)$. Given the stated effective radius of this galaxy of 3.5 kpc and the conversion of $R_{25} = 6.74' = 9.61$ kpc at a distance of 4.898 Mpc to the host, their gradient may be expressed in terms of R_{25} as $-0.10\,R/R_e = -0.10 \cdot (9.61/3.5)\,R/R_{25} = -0.274\,R/R_{25}$. This gradient is consistent with the SAMI Zoom result for this host galaxy and metallicity method, lying within the 1σ error interval of the result. The literature intercept value is less agreeing however, differing by approximately 1.8 standard error values.

We are unable to determine any evidence of a break or discontinuity in the abundance gradient as identified by Bresolin et al. (2009a), as our sampling of HII regions becomes relatively thin past a radius of R_{25} with only three confirmed.

5.2.5 NGC 3521, NGC 5068, and NGC 628 (M74)

No abundance gradients could be determined using the SAMI Zoom data set for host galaxies NGC 3521, NGC 5068, and NGC 628,

given the restriction of a minimum of five valid radius–metallicity data points.

6 SUMMARY AND CONCLUSIONS

We present the SAMI Zoom Survey, a collection of 92 confirmed H II regions across seven nearby galaxies in both spatially resolved and integrated form. Observed using the AAOmega spectrograph on the Anglo-Australian Telescope (AAT), the spatially resolved sample is structured as three-dimensional data cubes with fields-of-view of approximately 14.7 arcsec, holding a spatial sampling of 0.5 arcsec per spaxel. Data cubes and integrated spectra are divided into blue and red spectral arms, covering wavelength ranges of 3700–5746 Å and 6300–7399 Å, respectively. The breadth and resolution of this spectral information is sufficient to derive metallicity measurements across the SAMI Zoom data set, in both spatially resolved and integrated forms, using many of the diagnostics available in current literature. This is complementary to existing data sets including the CHAOS (Berg et al. 2015, 2020), MaNGA (Bundy et al. 2015; Yan et al. 2016), SAMI galaxy survey (Croom et al. 2012; Bryant et al. 2015; Sharp et al. 2015), TYPHOON (Poetrodjojo et al. 2019; Grasha et al. 2022; Chen et al. 2023), and PHANGS-MUSE (Emsellem et al. 2022) samples.

We measure such metallicities using the direct electron temperature method as described by Pérez-Montero (2017) and the strong emission diagnostics R_{23} (Kobulnicky & Kewley 2004; Poetrodjojo et al. 2021), N2O2 and N2S2 (Kewley et al. 2019), N2Hα (Pettini & Pagel 2004), N2S2Hα (Dopita et al. 2016), and O3N2 (Marino et al. 2013). We compare metallicites computed with the various methods, using $Z(R_{23})$ as the fiducial metallicity.

Where applicable, metallicity gradients for four of the seven host galaxies in this survey are constructed using metallicities determined from the set of diagnostics above, and contrasted between each other as well as past literature values.

The main findings throughout this work are summarized here:

(i) The SAMI Zoom Survey contains data of sufficient spectral resolution and coverage to investigate many forms of optical metallicity diagnostics found throughout the literature. The high spatial resolution allows for individual H II regions to be resolved at a FWHM of 18–150 pc. The spectral ranges of the data of both spatially resolved and integrated forms allow for robust spectral analysis, detecting key strong emission lines across the sample as well as fainter but crucial lines such as auroral [O III] λ4363 in a handful of cases (Figs 2, 5, and 6; Table A2). A total of 92 H II regions were confirmed within the data set.

(ii) The spatially resolved confirmed region sample holds a total of 46 660 spaxels with detected (SNR > 3) Hα emission, with totals of 32 175 in Hβ, 26 677 in [O III] λ5007, and 713 in [O III] λ4363. In the integrated data set, all 92 confirmed regions held detected Hα and [O III] λ5007, with 91 in Hβ and 8 in [O III] λ4363.

(iii) Metallicity measurements determined using separate methods return significantly different results (Fig. 8; Table A4). When compared to the fiducial R_{23} metallicity within the integrated region sample (Fig. 9; Table 4), the O3N2 method shows the greatest disagreement with a mean disparity of 0.49 dex in oxygen abundance. Compared to the direct electron temperature method, we find a mean discrepancy of 0.46 dex in oxygen abundance, up to a maximum of 0.65 dex; however, this method has considerably fewer comparable data points within the integrated region sample, primarily due to limited detections of auroral [O III] λ4363. These disagreements are also generally consistent with the previous findings in the field.

(iv) We fit abundance gradient profiles to the host galaxies NGC 300, NGC 3621, IC 5201, and NGC 5236 (M83) using diagnostics for which at least five valid data points exist. We find negative gradients in all cases (shown in Figs A2 to A5; Tables 6 and 7), averaging $-0.39\,\mathrm{dex\,R_{25}}^{-1}$ for NGC 300, $-0.22\,\mathrm{dex\,R_{25}}^{-1}$ for IC 5201, and $-0.20\,\mathrm{dex\,R_{25}}^{-1}$ for NGC 5236, as well as the presence of a break at R_{25} and subsequent flattening for NGC 3621 with inner-disc gradients averaging $-0.44\,\mathrm{dex\,R_{25}}^{-1}$ up to R_{25} and outer disc metallicities averaging to $12 + \log(\mathrm{O/H}) = 8.39$. All derived gradients indicate metal-rich galactic centres leading to metal-poor outskirts characteristic to inside-out galaxy formation.

(v) Comparing derived abundance gradients for each host galaxy, we find considerable variation in both gradient slope and intercept (up to $0.51\,\mathrm{dex\,R_{25}}^{-1}$ and 0.66 dex respectively), indicating in our sample that choice of method has a substantial impact on the result. This is further supported by comparisons between past literature gradients, which also show notable variations (Figs A2 to A5).

In the future, we plan to address the spatially resolved data set in higher detail to uncover how spatial variations of H II region properties impact metallicity determinations. A forthcoming paper will conduct a spatially resolved analysis of the discrepancy between metallicities estimated with strong emission lines and those estimated with the electron temperature method, and investigate a connection between the discrepancy and the geometry and degree of spatial variation within the HII regions upon which the diagnostics are calibrated (Sweet et al., in preparation).

The publicly available SAMI Zoom data would be ideal to inform the calibration of theoretical models, including tailored 3D spherical models such as MOCASSIN (Ercolano, Barlow & Storey 2005) or Messenger Monte Carlo MAPPINGS V (M3, Jin, Kewley & Sutherland 2022a, b). It could enable a study of the kinematic structure of H II regions, probing the contribution to galactic thermal broadening and turbulence from expansion of the regions, as suggested by Barat et al. (2020) and Gao et al. (2023). Other works could include a study of ionization sources by cross-matching with high-energy catalogues, which would inform the validity of calibrating metallicity diagnostics against such regions, or an investigation into the conditions within super star clusters, thought to be analogues of high-redshift star formation clumps.

A number of extensions to SAMI Zoom can be foreseen. Deeper observations would be needed for a spatially resolved comparison of temperatures derived from auroral lines of different species as in Berg et al. (2020), for example with Hector (Bryant et al. 2024) which replaces SAMI at the AAT and offers improved spectral resolution, larger fields of view, and more IFUs. Observations could also be extended to a wider wavelength range, for example with XSHOOTER to include near-infrared lines and better trace the full range of temperature variations, ionizations, and densities.

ACKNOWLEDGEMENTS

The authors would like to thank Lisa J. Kewley for mentoring the SAMI Zoom concept, Julia J. Bryant for invaluable assistance tiling and configuring the plates, Gerhardt R. Meurer for assistance with target selection, the AAT night assistants and Joshua d'Agostino and Henry Poetrodjojo for help with the observations, I-Ting Ho for help with LZIFU, and Erica Thygesen for early work on the data reduction.

AM is grateful for the support through an Australian Government Research Training Program Scholarship (RTPS). This research was also supported by the Australian Research Council Centre of Excellence for All Sky Astrophysics in 3 Dimensions (ASTRO 3D),

through project number CE170100013. SMS acknowledges funding from the Australian Research Council (DE220100003). TN and KG acknowledge support from Australian Research Council Laureate Fellowship FL180100060. AJC acknowledges funding from the 'FirstGalaxies' Advanced Grant from the European Research Council (ERC) under the European Union's Horizon 2020 research and innovation programme (grant agreement no. 789056). KGr is supported by the Australian Research Council through the Discovery Early Career Researcher Award (DECRA) Fellowship (project number DE220100766) funded by the Australian Government. MK acknowledges support from the Australian Research Council through Laureate Fellowship FL220100020.

Based on data acquired at the Anglo-Australian Telescope, under programmes A/2017A/17 and A/2018A/03. We acknowledge the traditional custodians of the land on which the AAT stands, the Gamilaraay people, and pay our respects to elders past and present.

DATA AVAILABILITY

The data from the first SAMI Zoom Survey release will be publicly available online at Data Central, https://datacentral.org.au/.

REFERENCES

Barat D., D'Eugenio F., Colless M., Sweet S. M., Groves B., Cortese L., 2020, MNRAS, 498, 5885
Barrera-Ballesteros J. K. et al., 2023, RMxAA, 59, 213
Belfiore F. et al., 2017, MNRAS, 469, 151
Berg D. A., Skillman E. D., Croxall K. V., Pogge R. W., Moustakas J., Johnson-Groh M., 2015, ApJ, 806, 16
Berg D. A., Pogge R. W., Skillman E. D., Croxall K. V., Moustakas J., Rogers N. S. J., Sun J., 2020, ApJ, 893, 96
Boissier S., Prantzos N., 1999, MNRAS, 307, 857
Bresolin F., Ryan-Weber E., Kennicutt R. C., Goddard Q., 2009a, ApJ, 695, 580
Bresolin F., Gieren W., Kudritzki R.-P., Pietrzyński G., Urbaneja M. A., Carraro G., 2009b, ApJ, 700, 309
Bresolin F., Kennicutt R. C., Ryan-Weber E., 2012, ApJ, 750, 122
Bryant J. J. et al., 2015, MNRAS, 447, 2857
Bryant J. J. et al., 2024, in Bryant J. J., Motohara K., Vernet J. R. D., eds, Proc. SPIE Conf. Ser. Vol. 13096, Ground-based and Airborne Instrumentation for Astronomy X. SPIE, Bellingham, p. 130960D
Bundy K. et al., 2015, ApJ, 798, 7
Cameron A. J., Yuan T., Trenti M., Nicholls D. C., Kewley L. J., 2021, MNRAS, 501, 3695
Cardelli J. A., Clayton G. C., Mathis J. S., 1989, ApJ, 345, 245
Cenarro A. J. et al., 2007, MNRAS, 374, 664
Chen Q.-H., Grasha K., Battisti A. J., Kewley L. J., Madore B. F., Seibert M., Rich J. A., Beaton R. L., 2023, MNRAS, 519, 4801
Croom S. M. et al., 2012, MNRAS, 421, 872
Croxall K. V. et al., 2013, ApJ, 777, 96
Curti M., Cresci G., Mannucci F., Marconi A., Maiolino R., Esposito S., 2017, MNRAS, 465, 1384
Della Bruna L. et al., 2022, A&A, 666, A29
Dodorico S., Rosa M., Wampler E. J., 1983, A&AS, 53, 97
Dopita M. A., Kewley L. J., Sutherland R. S., Nicholls D. C., 2016, Ap&SS, 361, 61
Emsellem E. et al., 2022, A&A, 659, A191
Ercolano B., Barlow M. J., Storey P. J., 2005, MNRAS, 362, 1038
Faesi C. M., Lada C. J., Forbrich J., Menten K. M., Bouy H., 2014, ApJ, 789, 81
Falcón-Barroso J., Sánchez-Blázquez P., Vazdekis A., Ricciardelli E., Cardiel N., Cenarro A. J., Gorgas J., Peletier R. F., 2011, A&A, 532, A95
Fu J., Hou J. L., Yin J., Chang R. X., 2009, ApJ, 696, 668
Gao Y., Gu Q., Liu G., Zhang H., Shi Y., Dou J., Li X., Kong X., 2023, A&A, 677, A179
Goddard D. et al., 2017, MNRAS, 466, 4731
Grasha K. et al., 2022, ApJ, 929, 118
Groves B. et al., 2023, MNRAS, 520, 4902
Hägele G. F., Díaz A. I., Terlevich E., Terlevich R., Pérez-Montero E., Cardaci M. V., 2008, MNRAS, 383, 209
Ho I. T., Kudritzki R.-P., Kewley L. J., Zahid H. J., Dopita M. A., Bresolin F., Rupke D. S. N., 2015, MNRAS, 448, 2030
Ho I.-T. et al., 2016, Ap&SS, 361, 280
Hodge P. W., 1976, ApJ, 205, 728
Hodge P. W., Kennicutt R. C. J., 1983, AJ, 88, 296
Izotov Y. I., Stasińska G., Meynet G., Guseva N. G., Thuan T. X., 2006, A&A, 448, 955
Jin Y., Kewley L. J., Sutherland R., 2022a, ApJ, 927, 37
Jin Y., Kewley L. J., Sutherland R. S., 2022b, ApJ, 934, L8
Jin Y., Sutherland R., Kewley L. J., Nicholls D. C., 2023, ApJ, 958, 179
Jones D. H. et al., 2009, MNRAS, 399, 683
Kewley L. J., Dopita M. A., 2002, ApJS, 142, 35
Kewley L. J., Ellison S. L., 2008, ApJ, 681, 1183
Kewley L. J., Rupke D., Zahid H. J., Geller M. J., Barton E. J., 2010, ApJ, 721, L48
Kewley L. J., Nicholls D. C., Sutherland R. S., 2019, ARA&A, 57, 511
Khramtsova M. S., Wiebe D. S., Boley P. A., Pavlyuchenkov Y. N., 2013, MNRAS, 431, 2006
Kobulnicky H. A., Kewley L. J., 2004, ApJ, 617, 240
Leitherer C. et al., 1999, ApJS, 123, 3
López-Sánchez Á. R., Esteban C., 2010, A&A, 517, A85
López-Sánchez Á. R., Dopita M. A., Kewley L. J., Zahid H. J., Nicholls D. C., Scharwächter J., 2012, MNRAS, 426, 2630
Luridiana V., Morisset C., Shaw R. A., 2015, A&A, 573, A42
Maiolino R., Mannucci F., 2019, A&A Rev., 27, 3
Makarov D., Prugniel P., Terekhova N., Courtois H., Vauglin I., 2014, A&A, 570, A13
Mannucci F. et al., 2021, MNRAS, 508, 1582
Marino R. A. et al., 2013, A&A, 559, A114
Martin D. C. et al., 2005, ApJ, 619, L1
McGaugh S. S., 1991, ApJ, 380, 140
McLeod A. F. et al., 2021, MNRAS, 508, 5425
Méndez-Delgado J. E., Esteban C., García-Rojas J., Kreckel K., Peimbert M., 2023, Nature, 618, 249
Meurer G. R. et al., 2006, ApJS, 165, 307
Monreal-Ibero A., Relaño M., Kehrig C., Pérez-Montero E., Vílchez J. M., Kelz A., Roth M. M., Streicher O., 2011, MNRAS, 413, 2242
Moustakas J., Kennicutt Robert C. J., Tremonti C. A., Dale D. A., Smith J.-D. T., Calzetti D., 2010, ApJS, 190, 233
Newville M., Stensitzki T., Allen D. B., Ingargiola A., 2014, LMFIT: Non-Linear Least-Square Minimization and Curve-Fitting for Python. Zenodo, available at: https://zenodo.org/records/11813
Nicholls D. C., Kewley L. J., Sutherland R. S., 2020, PASP, 132, 033001
Osterbrock D. E., 1989, Astrophysics of Gaseous Nebulae and Active Galactic Nuclei. University Science Books, Sausalito, California, p. 307
Pagel B. E. J., Edmunds M. G., Blackwell D. E., Chun M. S., Smith G., 1979, MNRAS, 189, 95
Payne J. L., Filipović M. D., Pannuti T. G., Jones P. A., Duric N., White G. L., Carpano S., 2004, A&A, 425, 443
Peimbert A., Peimbert M., 2013, ApJ, 778, 89
Peimbert M., 1967, ApJ, 150, 825
Peimbert M., Peimbert A., Delgado-Inglada G., 2017, PASP, 129, 082001
Pérez-Montero E., 2017, PASP, 129, 043001
Pettini M., Pagel B. E. J., 2004, MNRAS, 348, L59
Pilyugin L. S., Grebel E. K., 2016, MNRAS, 457, 3678
Pilyugin L. S., Thuan T. X., 2005, ApJ, 631, 231
Pilyugin L. S., Grebel E. K., Mattsson L., 2012, MNRAS, 424, 2316
Poetrodjojo H. et al., 2018, MNRAS, 479, 5235
Poetrodjojo H., D'Agostino J. J., Groves B., Kewley L., Ho I. T., Rich J., Madore B. F., Seibert M., 2019, MNRAS, 487, 79
Poetrodjojo H. et al., 2021, MNRAS, 502, 3357

Rickards Vaught R. J. et al., 2024, ApJ, 966, 130
Robitaille T., Rice T., Beaumont C., Ginsburg A., MacDonald B., Rosolowsky E., 2019, Astrophysics Source Code Library, record ascl:1907.016
Robotham A. et al., 2010, PASA, 27, 76
Rogers N. S. J., Skillman E. D., Pogge R. W., Berg D. A., Croxall K. V., Bartlett J., Arellano-Córdova K. Z., Moustakas J., 2022, ApJ, 939, 44
Rumstay K. S., Kaufman M., 1983, ApJ, 274, 611
Rupke D. S. N., Kewley L. J., Chien L. H., 2010, ApJ, 723, 1255
Ryder S. D., 1995, ApJ, 444, 610
Sánchez-Blázquez P. et al., 2006, MNRAS, 371, 703
Sánchez S. F. et al., 2019, MNRAS, 484, 3042
Sanders R. L., Shapley A. E., Zhang K., Yan R., 2017, ApJ, 850, 136
Scott N. et al., 2018, MNRAS, 481, 2299
Scudder J. M., Ellison S. L., El Meddah El Idrissi L., Poetrodjojo H., 2021, MNRAS, 507, 2468
Sérsic J. L., 1966, ZAp, 64, 212
Sharp R. et al., 2015, MNRAS, 446, 1551
Stasińska G., Peña M., Bresolin F., Tsamis Y. G., 2013, A&A, 552, A12
Sutherland R. S., Dopita M. A., 2017, ApJS, 229, 34
Thilker D. A., Braun R., Walterbos R. A. M., 2000, AJ, 120, 3070
Toribio San Cipriano L., García-Rojas J., Esteban C., Bresolin F., Peimbert M., 2016, MNRAS, 458, 1866
Torres-Flores S. et al., 2014, in Revista Mexicana de Astronomia y Astrofisica Conference Series. National Autonomous University of Mexico, Mexico City, p. 188
Webster B. L., Smith M. G., 1983, MNRAS, 204, 743
Yan R. et al., 2016, AJ, 152, 197
Yates R. M., Schady P., Chen T. W., Schweyer T., Wiseman P., 2020, A&A, 634, A107
Zaritsky D., Kennicutt R. C. Jr, Huchra J. P., 1994, ApJ, 420, 87
van Zee L., Salzer J. J., Haynes M. P., O'Donoghue A. A., Balonek T. J., 1998, AJ, 116, 2805
Zhang K. et al., 2017, MNRAS, 466, 3217
Zheng Z. et al., 2017, MNRAS, 465, 4572

APPENDIX A: SUPPLEMENTARY TABLES AND FIGURES

Table A1 contains the SAMI Zoom Survey target catalogue, listed with observational parameters, sourced catalogues, and the amount of H II regions confirmed within each field. Table A2 lists the integrated-region fluxes through a set nine key emission lines across the confirmed HII regions of the SAMI Zoom sample. Derived properties including electron temperatures and densities as well as ionization are presented in Table A3 for each of these regions in the integrated data set. Table A4 contains the metallicities measured throughout the integrated data set for the seven diagnostics addressed in this work; also listed are the determined galactocentric radii (in terms of R/R_{25}) for each region. Lastly, Table A5 lists the alternate metallicity gradient parameters for NGC 3621 accounting for an unbroken profile, used to check the preferred form.

Fig. A1 displays the spatially resolved H II region flux maps of emissions Hα and [O III] λ5007 for the set of 92 confirmed regions in the SAMI Zoom Survey. Figs A2 to A5 present measured metallicity gradients constructed where possible (given the five data point restriction described in Section 5.2), which could be applied to four of the seven host galaxies; also plotted are literature comparisons used to contrast against the SAMI Zoom data set.

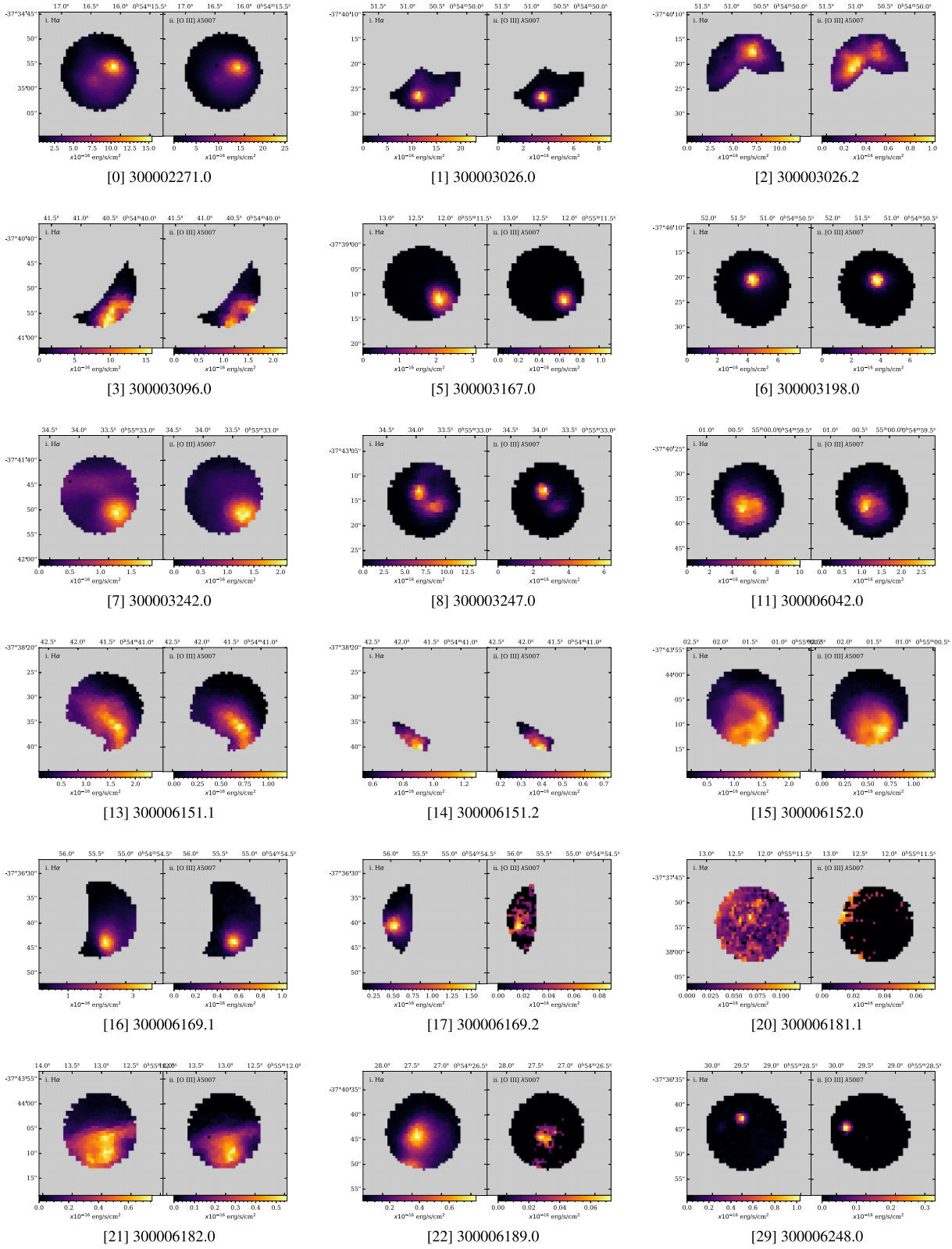

[0] 300002271.0 [1] 300003026.0 [2] 300003026.2

[3] 300003096.0 [5] 300003167.0 [6] 300003198.0

[7] 300003242.0 [8] 300003247.0 [11] 300006042.0

[13] 300006151.1 [14] 300006151.2 [15] 300006152.0

[16] 300006169.1 [17] 300006169.2 [20] 300006181.1

[21] 300006182.0 [22] 300006189.0 [29] 300006248.0

Figure A1. Spatially resolved fitted flux maps for i. Hα and ii. [O III] λ5007 across the 92 confirmed SAMI Zoom HII regions. Panels are labelled using respective region IDs (see Table A2) in square brackets.

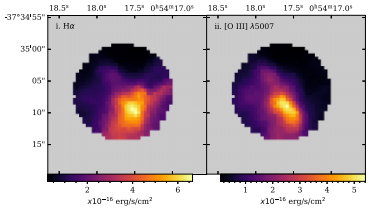

[31] 300006262.0

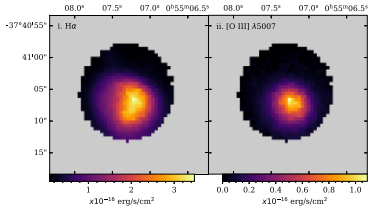

[33] 300008108.0

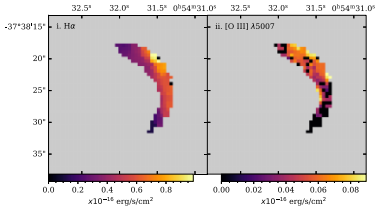

[35] 300008185.3

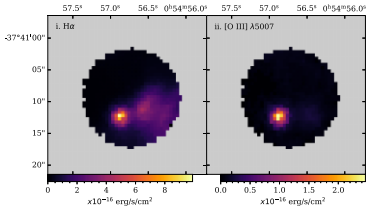

[39] 300009011.0

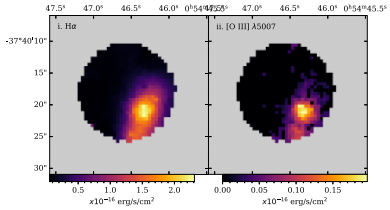

[40] 300009050.0

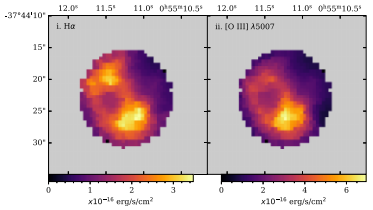

[41] 300009180.0

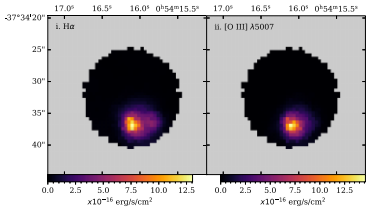

[43] 300009275.0

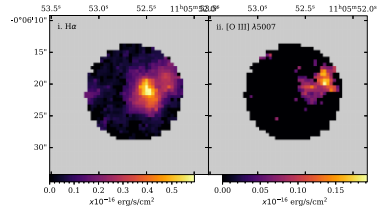

[51] 3521003210.0

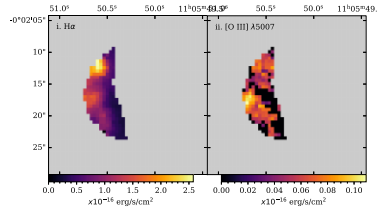

[53] 3521003295.1

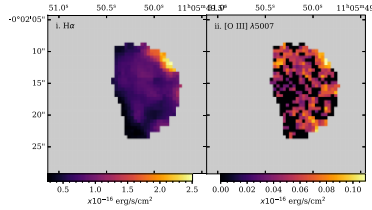

[54] 3521003295.2

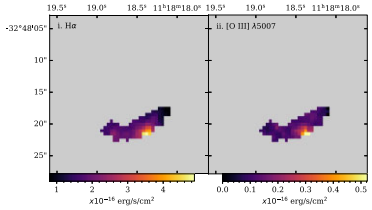

[60] 3621001001.0

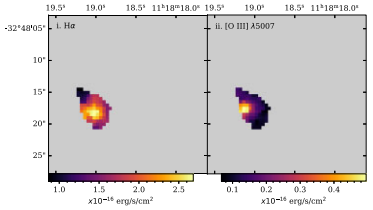

[61] 3621001001.3

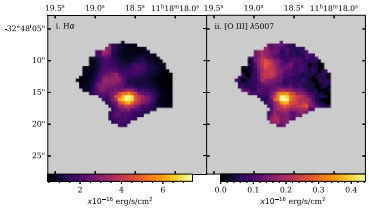

[62] 3621001001.4

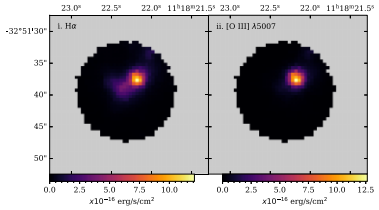

[63] 3621001019.0

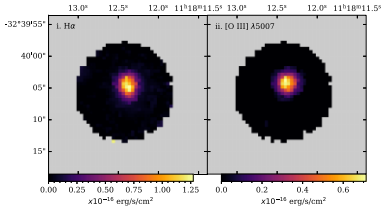

[66] 3621005021.0

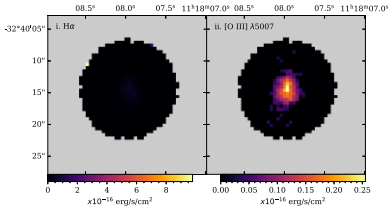

[67] 3621005022.0

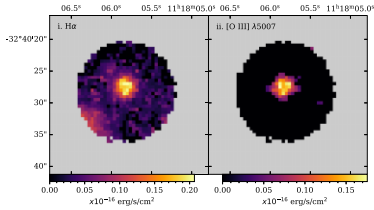

[68] 3621005023.0

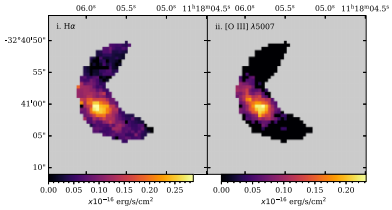

[70] 3621005026.1

Figure A1. – *continued*

Figure A1. (cont.)

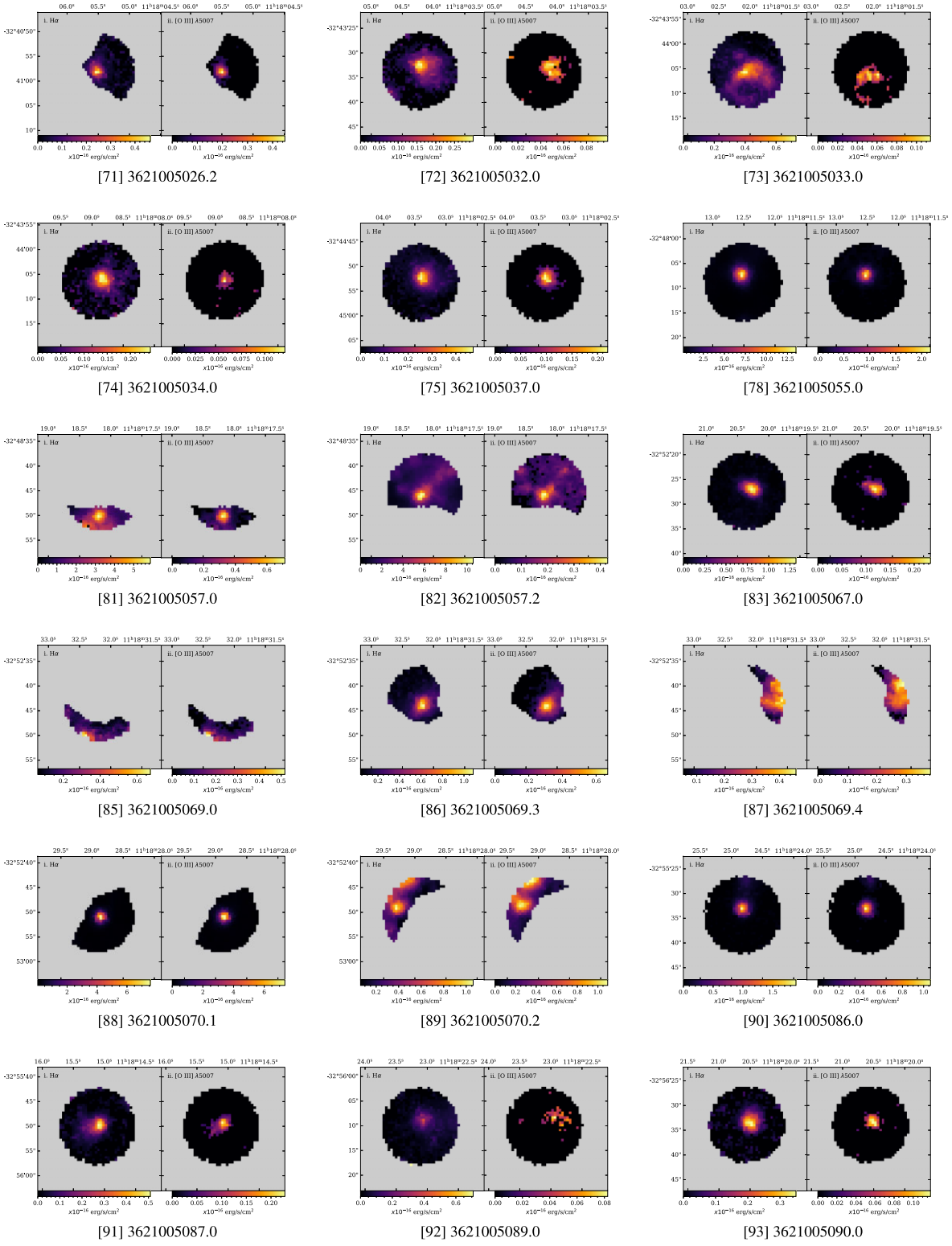

[71] 3621005026.2 [72] 3621005032.0 [73] 3621005033.0

[74] 3621005034.0 [75] 3621005037.0 [78] 3621005055.0

[81] 3621005057.0 [82] 3621005057.2 [83] 3621005067.0

[85] 3621005069.0 [86] 3621005069.3 [87] 3621005069.4

[88] 3621005070.1 [89] 3621005070.2 [90] 3621005086.0

[91] 3621005087.0 [92] 3621005089.0 [93] 3621005090.0

Figure A1. *– continued*

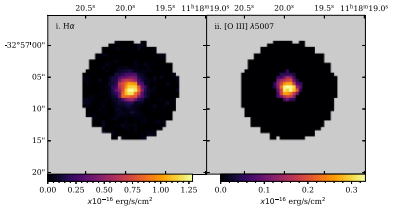

[94] 3621005091.0

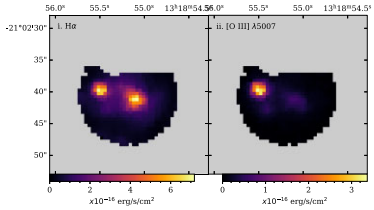

[95] 5068001006.1

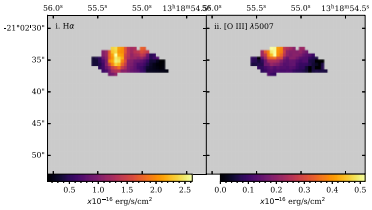

[96] 5068001006.2

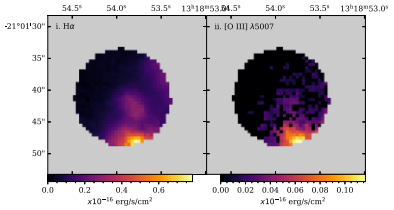

[106] 5068002272.0

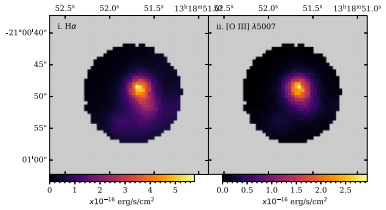

[108] 5068002323.0

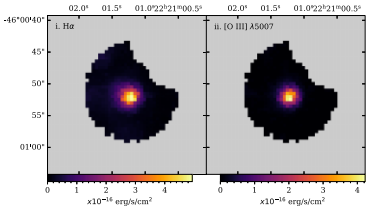

[118] 5201001038.0

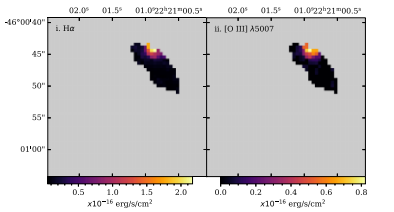

[119] 5201001038.2

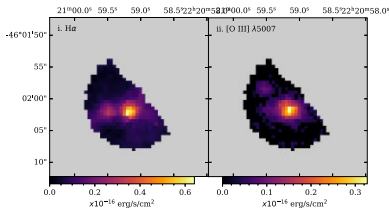

[120] 5201001053.1

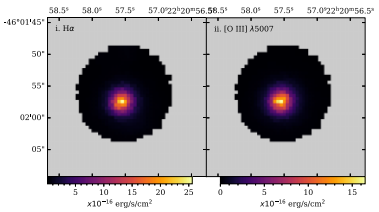

[123] 5201001069.0

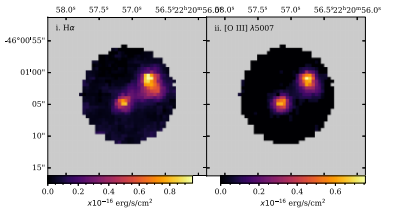

[124] 5201001075.0

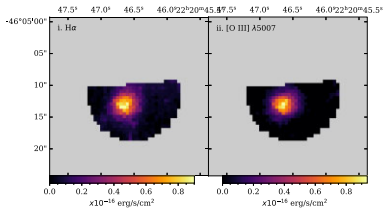

[125] 5201001133.1

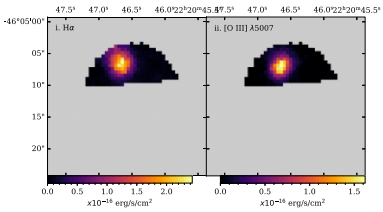

[126] 5201001133.2

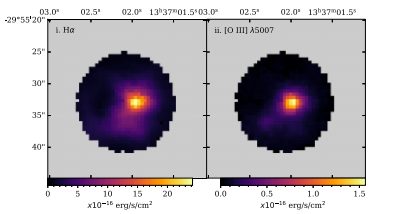

[132] 5236004216.0

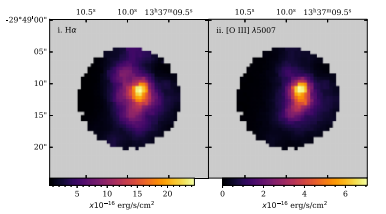

[133] 5236004309.0

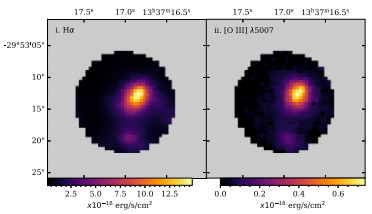

[134] 5236004341.0

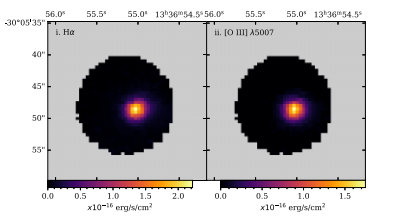

[135] 5236006127.0

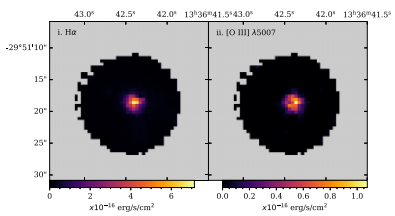

[140] 5236009025.0

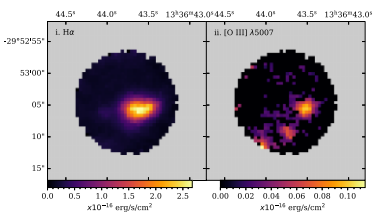

[142] 5236009030.1

Figure A1. – *continued*

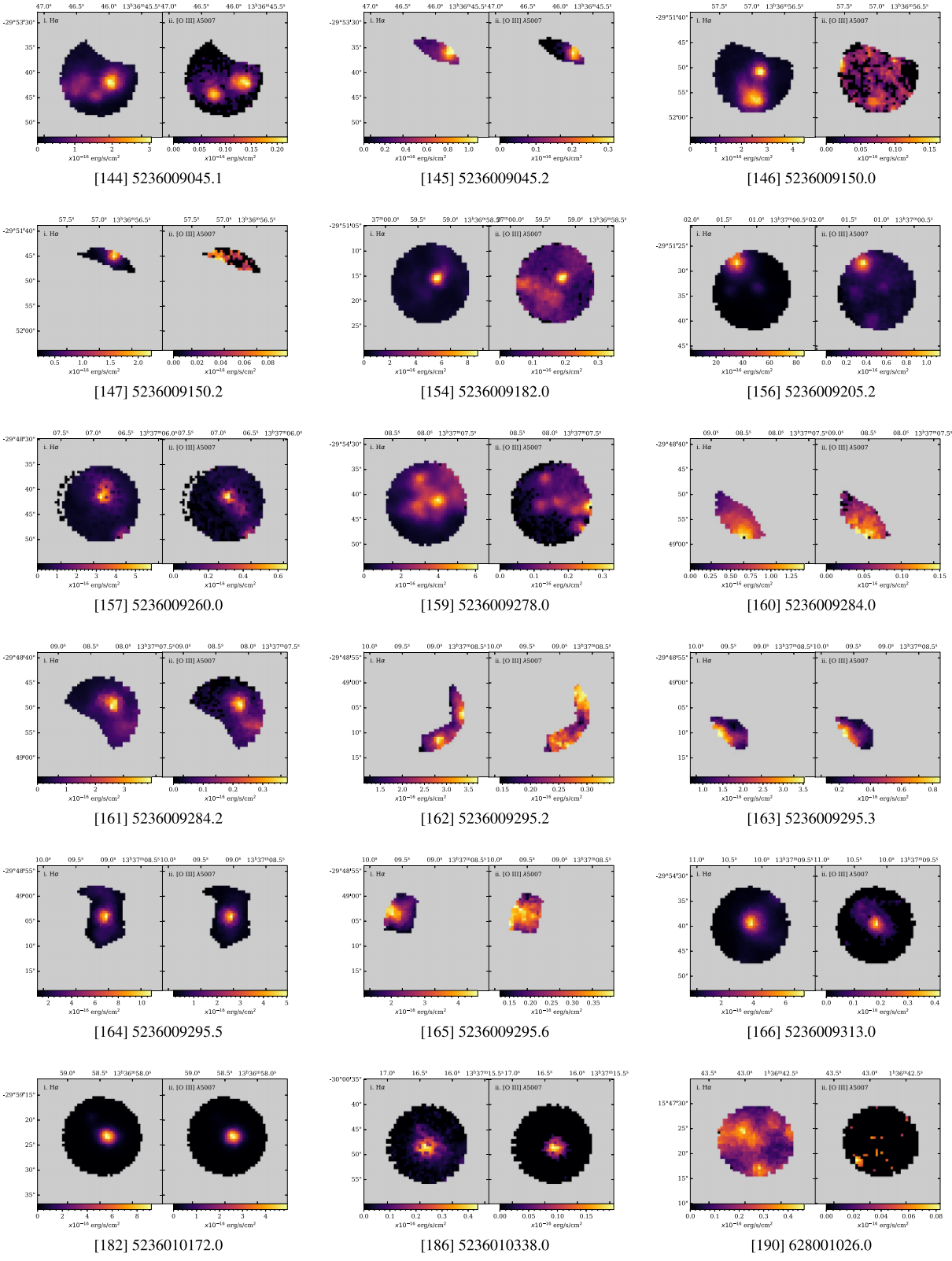

Figure A1. – *continued*

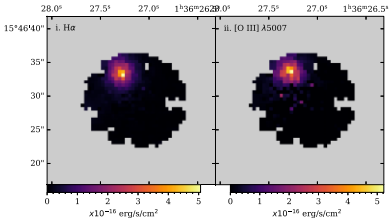

[191] 628001677.0

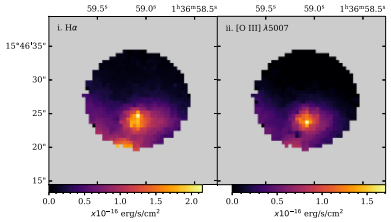

[196] 628001724.0

Figure A1. – *continued*

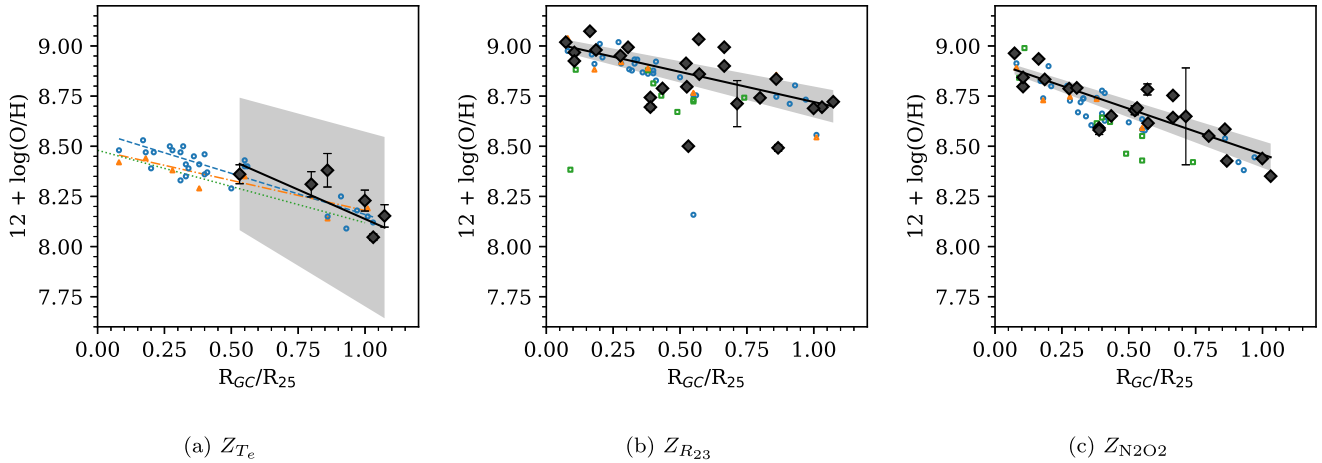

(a) Z_{T_e} (b) $Z_{R_{23}}$ (c) Z_{N2O2}

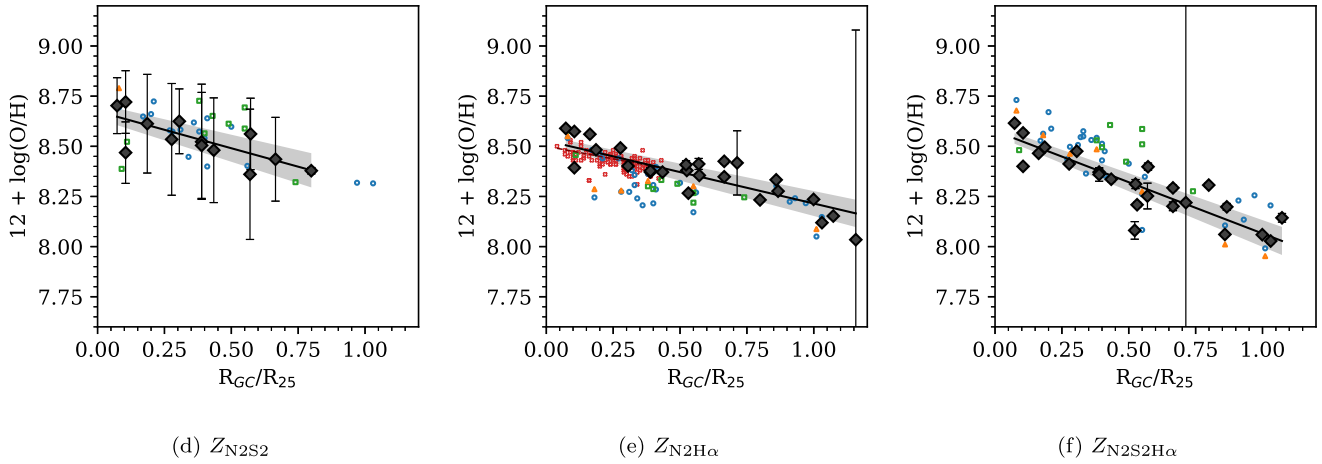

(d) Z_{N2S2} (e) $Z_{\mathrm{N2H}\alpha}$ (f) $Z_{\mathrm{N2S2H}\alpha}$

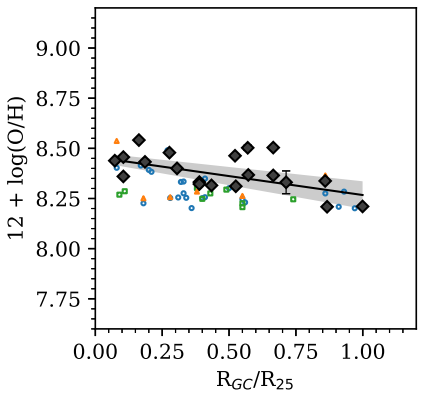

(g) Z_{O3N2}

Figure A2. Radial abundance gradients for NGC 300 using metallicity diagnostics for which at least five valid data points could be used to determine a confident linear trend. Data from this work (diamonds and solid line, with 1σ gradient uncertainty as the shaded region) is shown alongside gradients given by Bresolin et al. (2009b) as the dashed trend, Stasińska et al. (2013) as the dotted trend, and Toribio San Cipriano et al. (2016) as the dash-dotted trend in relevant subplots. Open data points represent metallicity–radius data derived in this work through a mirrored analysis, identical to the methods in Section 4, using the flux values and ratios reported within B09 (circles), S13 (squares), and T16 (triangles). Also shown in panel (e) as open cross points are the direct results from McLeod et al. (2021) and their N2Hα-method analysis. SAMI Zoom gradient parameters are given in Table 6.

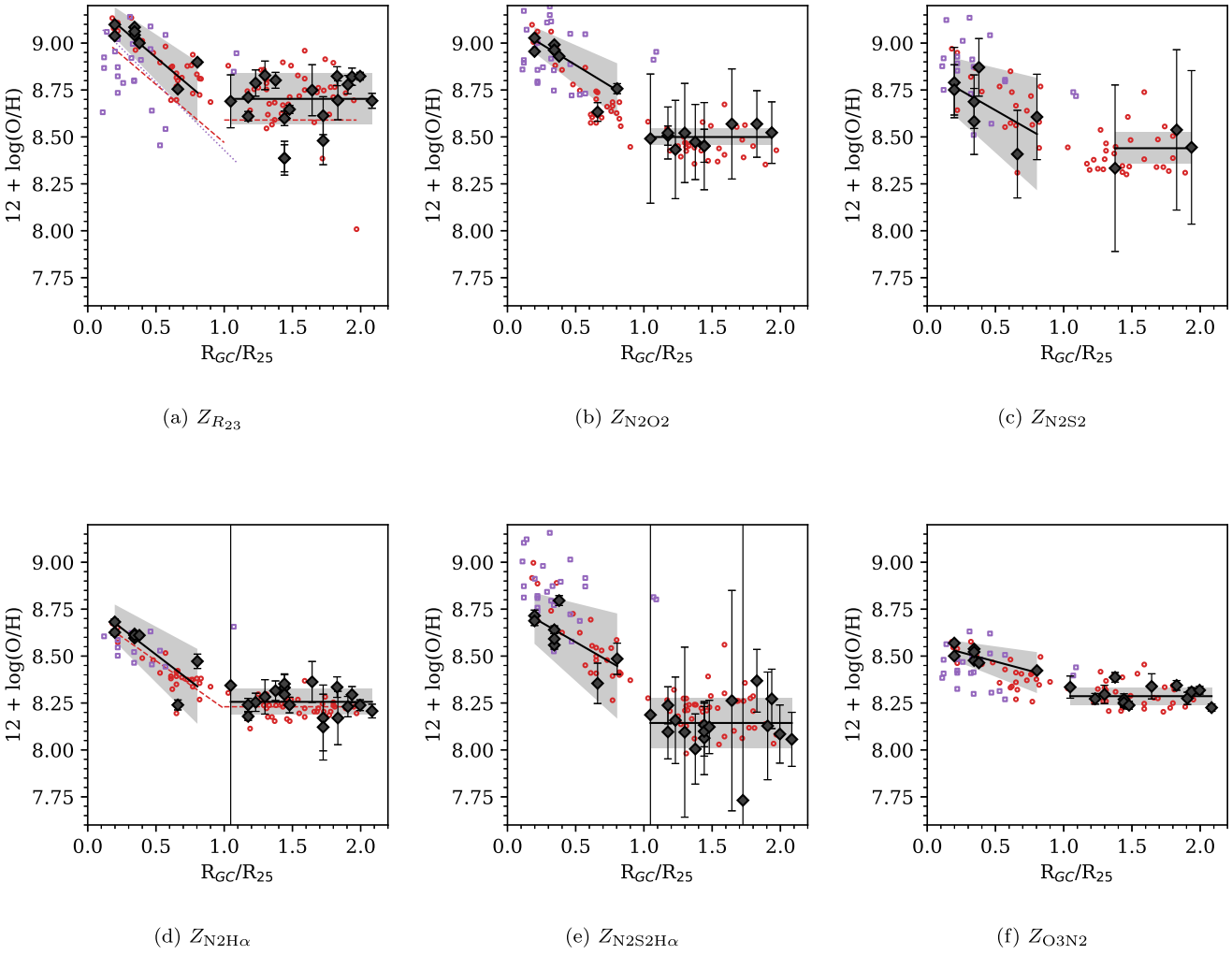

(a) $Z_{R_{23}}$ (b) Z_{N2O2} (c) Z_{N2S2}

(d) $Z_{\mathrm{N2H}\alpha}$ (e) $Z_{\mathrm{N2S2H}\alpha}$ (f) Z_{O3N2}

Figure A3. Radial abundance gradients for NGC 3621 using metallicity diagnostics for which at least five valid data points could be used to determine a confident linear trend. Data from this work, shown as diamonds and a solid trend, with 1σ gradient uncertainty as the shaded region, is shown alongside gradients given by Bresolin et al. (2012) and Ryder (1995) as the dashed and dotted trends respectively. Open data points represent data derived in this work through the metallicity methods as outlined in Section 4, using the flux values and ratios reported within B12 (circles) and R95 (squares). The gradient parameters for this work are given in Table 7. The discrepancy between the B12 gradient and respective data point set in panel A3(a) is due to a difference in metallicity method; the gradient shown is plotted directly as reported by B12 constructed using the McGaugh (1991) R_{23} approach, whereas the corresponding data point set was derived using the flux values of B12 within the metallicity method used in our work within Section 4.2.

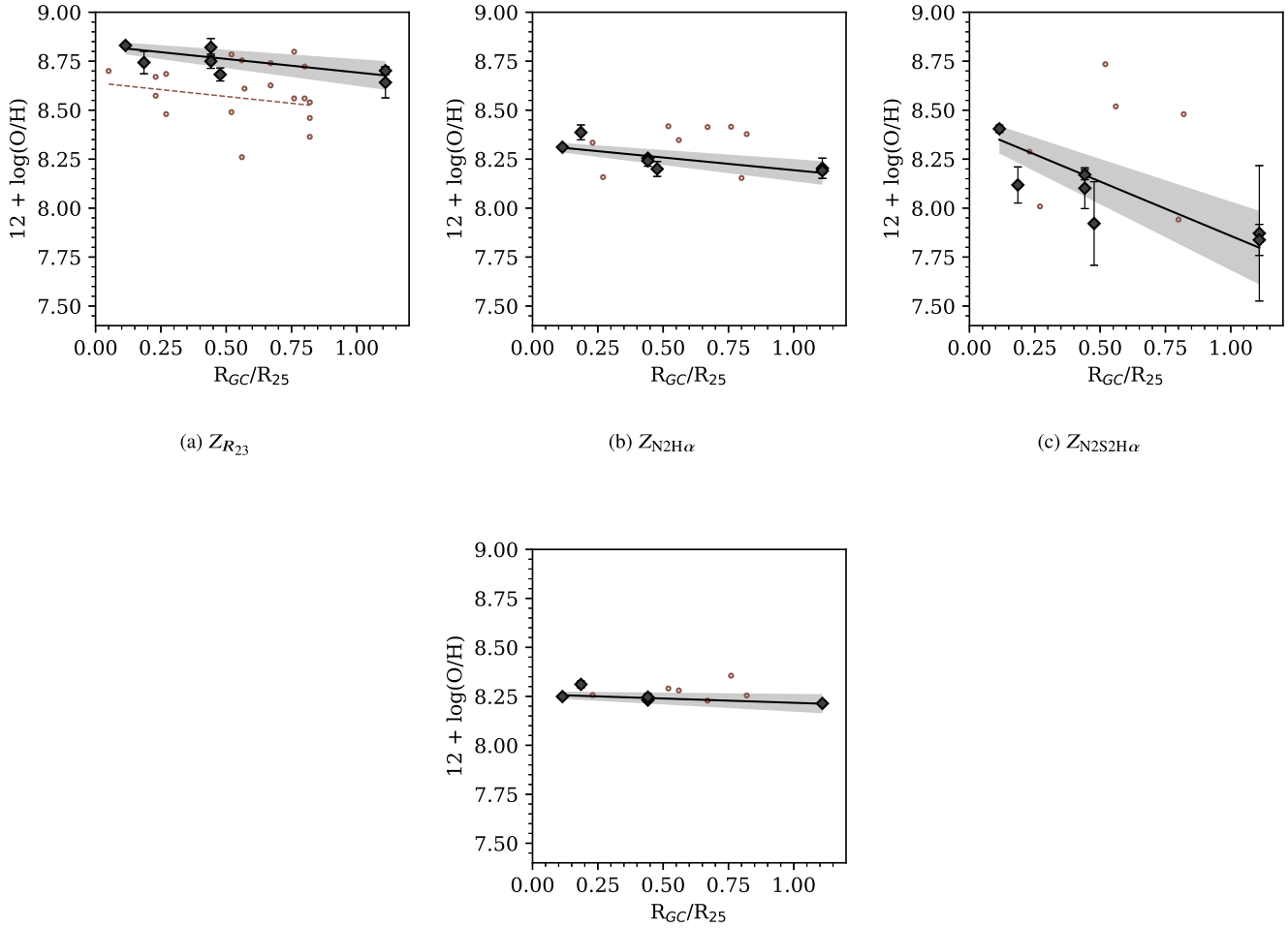

(a) $Z_{R_{23}}$ (b) $Z_{\mathrm{N2H}\alpha}$ (c) $Z_{\mathrm{N2S2H}\alpha}$

(d) Z_{O3N2}

Figure A4. Radial abundance gradients for IC 5201 using metallicity diagnostics for which at least five valid data points could be used to determine a confident linear trend. Data from this work is shown as diamonds and solid trend, with 1σ gradient uncertainty as the shaded region. Panel (a) also shows the gradient determined by Ryder (1995) as the dashed trend, while each panel shows data points derived in this work by taking reported flux values within the literature source and analysing them through the methods detailed in Section 4, shown as open circles. Gradient parameters for this work are given in Table 6.

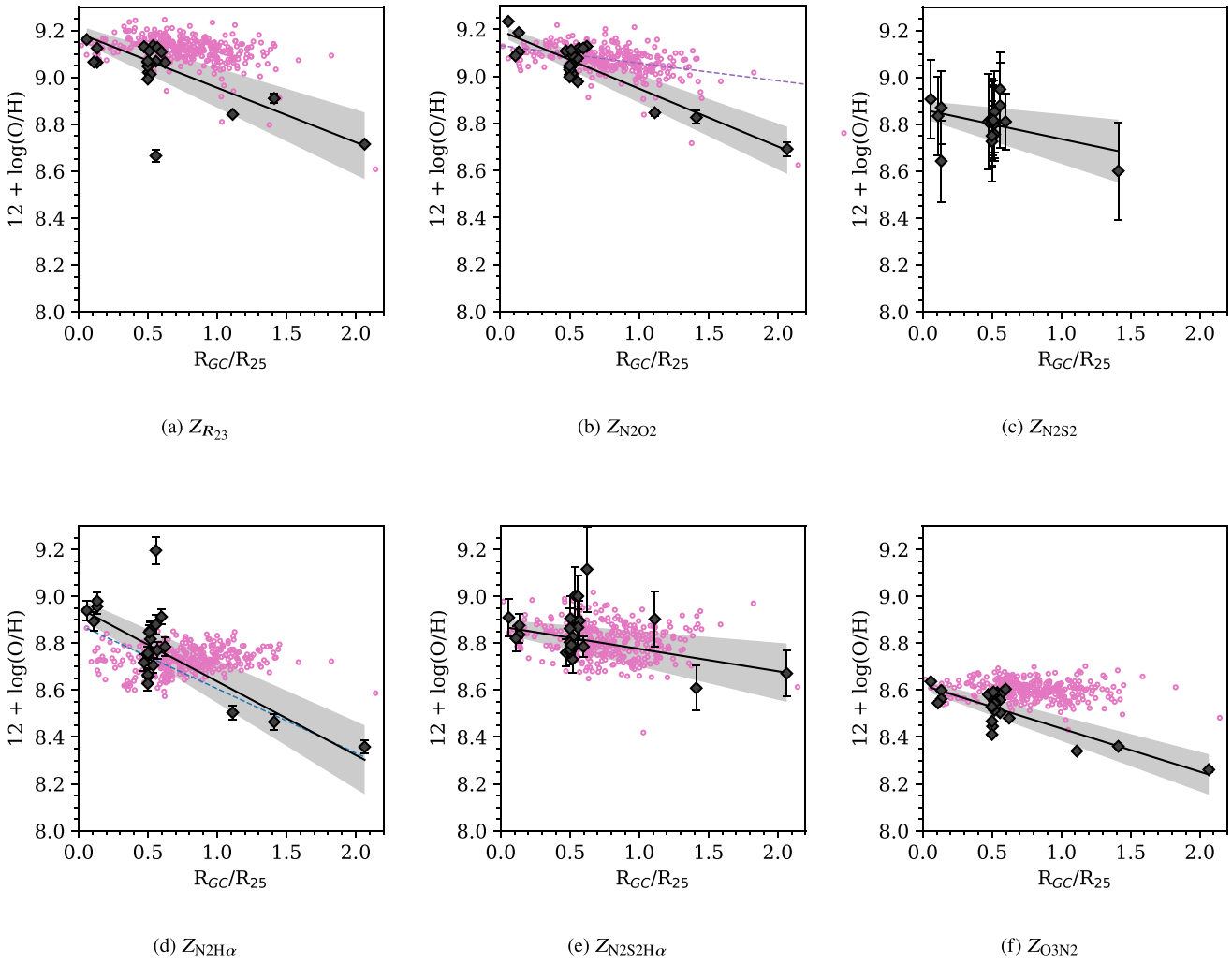

(a) $Z_{R_{23}}$ (b) Z_{N2O2} (c) Z_{N2S2}

(d) $Z_{\mathrm{N2H}\alpha}$ (e) $Z_{\mathrm{N2S2H}\alpha}$ (f) Z_{O3N2}

Figure A5. Radial abundance gradients for NGC 5236 (M83) using metallicity diagnostics for which at least five valid data points could be used to determine a confident linear trend. Data from this work is shown as diamonds and a solid trend, with 1σ gradient uncertainty as the shaded region. The gradient presented by Grasha et al. (2022) is shown within panel (b) as the dashed line, with open points representing metallicity–radius pairings derived in this work by taking reported flux values within the literature source and analysing them through the methods detailed through Section 4. Also shown in panel (d) is the N2Hα-method gradient determined by Della Bruna et al. (2022) as a dashed trend. Gradient parameters for this work are given in Table 6.

Table A1. The SAMI Zoom Survey target list.

Host galaxy	Target	RA	Dec.	Source catalogue (see Table 1)	Date	Blue grating	Red grating	Angular resolution (')	Exposure (minutes)	Confirmed regions
NGC 300	300002271	00:54:16.35	−37:34:57.3	6dF	2017 07 29	580V	1000R	2.4	91	1
	300003026	00:54:50.73	−37:40:22.2	ATCA	2017 07 28	580V	1000R	1.6	13	2
	300003096	00:54:40.68	−37:40:49.7	ATCA	2017 07 28	580V	1000R	1.8	91	1
	300003167	00:55:12.37	−37:39:08.5	ATCA	2017 07 28	580V	1000R	1.6	13	1
	300003198	00:54:51.34	−37:46:21.9	ATCA	2017 07 27	580V	1000R	1.6	91	1
	300003242	00:55:33.65	−37:41:47.8	ATCA	2017 07 29	580V	1000R	2.4	91	1
	300003247	00:55:33.87	−37:43:14.6	ATCA	2017 07 28	580V	1000R	1.8	91	1
	300005097	00:54:40.49	−37:40:51.6	DRW83	2017 07 27	580V	1000R	2.1	99	0
	300006042	00:55:00.30	−37:40:35.0	S66	2017 07 28	580V	1000R	1.8	91	1
	300006046	00:55:00.38	−37:40:33.0	S66	2017 07 27	580V	1000R	2.1	99	0
	300006151	00:54:41.63	−37:38:32.7	S66	2017 07 27	580V	1000R	1.6	91	2
	300006152	00:55:01.54	−37:44:07.2	S66	2017 07 28	580V	1000R	1.6	13	1
	300006169	00:54:55.44	−37:36:39.9	S66	2017 07 28	580V	1000R	1.6	13	2
	300006171	00:54:54.75	−37:36:37.4	S66	2017 07 29	580V	1000R	2.4	91	0
	300006173	00:54:31.10	−37:41:54.0	S66	2017 07 27	580V	1000R	1.6	91	0
	300006181	00:55:12.30	−37:37:54.0	S66	2017 07 27	580V	1000R	1.6	91	1
	300006182	00:55:13.03	−37:44:06.2	S66	2017 07 27	580V	1000R	2.1	99	1
	300006189	00:54:27.30	−37:40:44.0	S66	2017 07 29	580V	1000R	2.4	91	1
	300006193	00:55:16.00	−37:43:49.0	S66	2017 07 27	580V	1000R	1.6	91	0
	300006224	00:55:01.00	−37:47:23.0	S66	2017 07 29	580V	1000R	2.4	91	0
	300006226	00:54:20.80	−37:38:51.0	S66	2017 07 28	580V	1000R	1.8	91	0
	300006228	00:54:21.80	−37:38:16.0	S66	2017 07 27	580V	1000R	1.6	91	0
	300006238	00:55:27.97	−37:44:17.0	S66	2017 07 28	580V	1000R	1.6	13	0
	300006245	00:55:33.50	−37:43:14.0	S66	2017 07 27	580V	1000R	2.1	99	0
	300006248	00:55:29.40	−37:36:46.0	S66	2017 07 28	580V	1000R	1.6	13	1
	300006260	00:55:35.00	−37:45:01.0	S66	2017 07 27	580V	1000R	1.6	91	0
	300006262	00:54:17.62	−37:35:07.4	S66	2017 07 28	580V	1000R	1.6	13	1
	300006272	00:54:16.39	−37:34:52.5	S66	2017 07 28	580V	1000R	1.8	91	0
	300008108	00:55:07.30	−37:41:06.1	SSTS	2017 07 29	580V	1000R	2.4	91	1
	300008185	00:54:31.91	−37:38:25.9	SSTS	2017 07 28	580V	1000R	1.6	13	1
	300008205	00:55:20.28	−37:39:38.6	SSTS	2017 07 28	580V	1000R	1.8	91	0
	300008206	00:55:15.40	−37:44:39.2	SSTS	2017 07 29	580V	1000R	2.4	91	0
	300009011	00:54:56.80	−37:41:09.2	WS83	2017 07 27	580V	1000R	1.6	91	1
	300009050	00:54:46.55	−37:40:18.7	WS83	2017 07 29	580V	1000R	2.4	91	1
	300009180	00:55:11.23	−37:44:22.7	WS83	2017 07 28	580V	1000R	1.8	91	1
	300009270	00:54:16.40	−37:34:58.0	WS83	2017 07 27	580V	1000R	2.1	99	0
	300009275	00:54:16.19	−37:34:32.4	WS83	2017 07 27	580V	1000R	1.6	91	1
NGC 3521	3521003153	11:06:16.00	−00:07:07.0	HIIPHOT	2018 04 21	580V	1000R	1.9	71	0
	3521003154	11:06:13.30	−00:06:56.0	HIIPHOT	2018 04 20	580V	1000R	1.6	71	0
	3521003155	11:06:13.10	00:03:13.0	HIIPHOT	2018 04 21	580V	1000R	1.9	71	0
	3521003156	11:06:12.60	−00:02:49.0	HIIPHOT	2018 04 21	580V	1000R	1.9	71	0
	3521003157	11:06:08.00	00:05:34.0	HIIPHOT	2018 04 20	580V	1000R	1.6	71	0

Table A1 – *continued*

Host galaxy	Target	RA	Dec.	Source catalogue (see Table 1)	Date	Blue grating	Red grating	Angular resolution (')	Exposure (minutes)	Confirmed regions
NGC 3521	3521003158	11:06:04.70	00:00:16.0	HIIPHOT	2018 04 20	580V	1000R	1.6	71	0
	3521003166	11:05:57.70	00:03:13.0	HIIPHOT	2018 04 21	580V	1000R	1.9	71	0
	3521003210	11:05:52.70	−00:06:22.0	HIIPHOT	2018 04 21	580V	1000R	1.9	71	1
	3521003232	11:05:51.80	−00:06:10.0	HIIPHOT	2018 04 20	580V	1000R	1.6	71	0
	3521003295	11:05:50.30	−00:02:17.0	HIIPHOT	2018 04 20	580V	1000R	1.6	71	2
	3521003366	11:05:48.90	−00:02:33.0	HIIPHOT	2018 04 21	580V	1000R	1.9	71	0
	3521003529	11:05:44.50	00:01:20.0	HIIPHOT	2018 04 20	580V	1000R	1.6	71	0
	3521003543	11:05:43.70	00:01:24.0	HIIPHOT	2018 04 21	580V	1000R	1.9	71	0
	3521003593	11:05:36.40	00:05:16.0	HIIPHOT	2018 04 20	580V	1000R	1.6	71	0
	3521003597	11:05:29.60	−00:02:48.0	HIIPHOT	2018 04 20	580V	1000R	1.6	71	0
NGC 3621	3621001001	11:18:18.62	−32:48:15.6	KWB2013	2018 04 22	580V	1000R	1.6	71	3
	3621001019	11:18:22.30	−32:51:40.2	KWB2013	2018 04 23	580V	1000R	2.1	70	1
	3621004005	11:18:12.38	−32:48:32.6	SSTS	2018 04 21	580V	1000R	1.7	70	0
	3621005021	11:18:12.40	−32:40:06.3	BKR12	2018 04 23	580V	1000R	2.1	70	1
	3621005022	11:18:08.00	−32:40:15.6	BKR12	2018 04 21	580V	1000R	1.7	70	1
	3621005023	11:18:05.80	−32:40:29.0	BKR12	2018 04 22	580V	1000R	1.9	70	1
	3621005025	11:18:13.20	−32:40:51.2	BKR12	2018 04 23	580V	1000R	2.1	70	0
	3621005026	11:18:05.50	−32:40:58.8	BKR12	2018 04 22	580V	1000R	1.6	71	2
	3621005032	11:18:04.20	−32:43:34.5	BKR12	2018 04 23	580V	1000R	2.1	70	1
	3621005033	11:18:02.10	−32:44:06.3	BKR12	2018 04 23	580V	1000R	2.1	70	1
	3621005034	11:18:08.90	−32:44:07.4	BKR12	2018 04 21	580V	1000R	1.7	70	1
	3621005037	11:18:03.40	−32:44:54.0	BKR12	2018 04 22	580V	1000R	1.9	70	1
	3621005040	11:18:01.90	−32:45:30.1	BKR12	2018 04 22	580V	1000R	1.6	71	0
	3621005055	11:18:12.50	−32:48:09.6	BKR12	2018 04 23	580V	1000R	2.1	70	1
	3621005056	11:18:14.00	−32:48:33.4	BKR12	2018 04 22	580V	1000R	1.9	70	0
	3621005057	11:18:18.20	−32:48:46.3	BKR12	2018 04 23	580V	1000R	2.1	70	2
	3621005067	11:18:20.40	−32:52:28.6	BKR12	2018 04 21	580V	1000R	1.7	70	1
	3621005068	11:18:32.80	−32:52:31.1	BKR12	2018 04 22	580V	1000R	1.9	70	0
	3621005069	11:18:32.20	−32:52:44.5	BKR12	2018 04 23	580V	1000R	2.1	70	3
	3621005070	11:18:28.90	−32:52:51.4	BKR12	2018 04 22	580V	1000R	1.6	71	2
	3621005086	11:18:24.80	−32:55:35.2	BKR12	2018 04 23	580V	1000R	2.1	70	1
	3621005087	11:18:15.10	−32:55:50.8	BKR12	2018 04 22	580V	1000R	1.6	71	1
	3621005089	11:18:23.10	−32:56:10.9	BKR12	2018 04 22	580V	1000R	1.9	70	1
	3621005090	11:18:20.60	−32:56:35.0	BKR12	2018 04 21	580V	1000R	1.7	70	1
	3621005091	11:18:20.00	−32:57:08.0	BKR12	2018 04 23	580V	1000R	2.1	70	1
NGC 5068	5068001006	13:18:55.19	−21:02:40.7	HK83	2018 04 20	580V	1000R	2.0	70	2
	5068002054	13:19:18.20	−21:00:28.0	HIIPHOT	2018 04 20	580V	1000R	2.0	70	0
	5068002055	13:19:17.90	−21:03:01.0	HIIPHOT	2018 04 21	580V	1000R	2.9	100	0
	5068002057	13:19:15.80	−21:01:32.0	HIIPHOT	2018 04 20	580V	1000R	2.1	100	0
	5068002058	13:19:13.30	−21:04:11.0	HIIPHOT	2018 04 20	580V	1000R	2.0	70	0
	5068002059	13:19:13.10	−20:57:57.0	HIIPHOT	2018 04 21	580V	1000R	2.9	100	0
	5068002060	13:19:13.00	−20:57:08.0	HIIPHOT	2018 04 20	580V	1000R	2.1	100	0

Table A1 – *continued*

Host galaxy	Target	RA	Dec.	Source catalogue (see Table 1)	Date	Blue grating	Red grating	Angular resolution (')	Exposure (minutes)	Confirmed regions
NGC 5068	5068002061	13:19:11.60	−21:07:27.0	HIIPHOT	2018 04 21	580V	1000R	2.9	100	0
	5068002071	13:19:06.90	−21:06:13.0	HIIPHOT	2018 04 20	580V	1000R	2.1	100	0
	5068002112	13:19:02.30	−21:07:36.0	HIIPHOT	2018 04 20	580V	1000R	2.0	70	0
	5068002272	13:18:53.90	−21:01:41.0	HIIPHOT	2018 04 20	580V	1000R	2.1	100	1
	5068002277	13:18:53.80	−20:58:02.0	HIIPHOT	2018 04 20	580V	1000R	2.0	70	0
	5068002323	13:18:51.80	−21:00:50.0	HIIPHOT	2018 04 21	580V	1000R	2.9	100	1
	5068002481	13:18:41.50	−21:05:57.0	HIIPHOT	2018 04 21	580V	1000R	2.9	100	0
	5068002482	13:18:38.80	−21:03:54.0	HIIPHOT	2018 04 20	580V	1000R	2.0	70	0
	5068002483	13:18:37.30	−20:57:15.0	HIIPHOT	2018 04 20	580V	1000R	2.0	70	0
	5068002484	13:18:35.30	−21:03:57.0	HIIPHOT	2018 04 20	580V	1000R	2.1	100	0
IC 5201	5201001001	22:21:29.60	−45:57:59.0	HIIPHOT	2018 04 20	580V	1000R	2.1	90	0
	5201001002	22:21:18.50	−46:03:40.0	HIIPHOT	2018 04 23	580V	1000R	1.5	70	0
	5201001003	22:21:15.60	−46:04:14.0	HIIPHOT	2018 04 21	580V	1000R	2.7	100	0
	5201001005	22:21:12.50	−45:58:55.0	HIIPHOT	2018 04 21	580V	1000R	2.7	100	0
	5201001011	22:21:07.70	−46:05:19.0	HIIPHOT	2018 04 22	580V	1000R	2.2	70	0
	5201001038	22:21:01.30	−46:00:52.0	HIIPHOT	2018 04 23	580V	1000R	1.5	70	2
	5201001053	22:20:59.20	−46:02:00.0	HIIPHOT	2018 04 20	580V	1000R	2.1	90	1
	5201001059	22:20:58.70	−45:58:11.0	HIIPHOT	2018 04 20	580V	1000R	2.1	90	0
	5201001069	22:20:57.50	−46:01:57.0	HIIPHOT	2018 04 21	580V	1000R	2.7	100	1
	5201001075	22:20:57.10	−46:01:04.0	HIIPHOT	2018 04 22	580V	1000R	2.2	70	1
	5201001133	22:20:46.60	−46:05:12.0	HIIPHOT	2018 04 23	580V	1000R	1.5	70	2
	5201001140	22:20:44.30	−46:07:27.0	HIIPHOT	2018 04 20	580V	1000R	2.1	90	0
	5201001147	22:20:41.00	−46:05:51.0	HIIPHOT	2018 04 22	580V	1000R	2.2	70	0
	5201001148	22:20:39.80	−46:04:30.0	HIIPHOT	2018 04 21	580V	1000R	2.7	100	0
	5201001149	22:20:36.90	−46:02:31.0	HIIPHOT	2018 04 20	580V	1000R	2.1	90	0
NGC 5236 (M83)	5236004190	13:37:00.10	−29:52:18.0	dPD83	2017 07 27	580V	1000R	1.7	152	0
	5236004216	13:37:02.08	−29:55:32.6	dPD83	2018 04 22	580V	1000R	1.7	140	1
	5236004309	13:37:10.00	−29:49:12.6	dPD83	2018 04 22	580V	1000R	1.7	70	1
	5236004341	13:37:17.00	−29:53:13.6	dPD83	2018 04 22	580V	1000R	1.7	140	1
	5236006127	13:36:55.15	−30:05:47.5	GALEX	2018 04 22	580V	1000R	1.7	140	1
	5236009016	13:36:35.25	−29:55:27.6	RK83	2017 07 27	580V	1000R	1.7	152	0
	5236009017	13:36:38.03	−29:52:33.6	RK83	2018 04 22	580V	1000R	1.7	70	0
	5236009018	13:36:38.11	−29:51:59.6	RK83	2018 04 21	580V	1000R	2.0	70	0
	5236009019	13:36:38.80	−29:50:15.6	RK83	2017 07 28	580V	1000R	2.0	104	0

Table A1 – *continued*

Host galaxy	Target	RA	Dec.	Source catalogue (see Table 1)	Date	Blue grating	Red grating	Angular resolution (')	Exposure (minutes)	Confirmed regions
NGC 5236	5236009025	13:36:42.48	−29:51:18.6	RK83	2017 07 27	580V	1000R	1.7	152	1
(M83)	5236009030	13:36:43.78	−29:53:04.6	RK83	2017 07 29	580V	1000R	1.7	173	1
	5236009033	13:36:44.55	−29:54:25.6	RK83	2017 07 28	580V	1000R	2.0	104	0
	5236009045	13:36:46.16	−29:53:40.6	RK83	2018 04 22	580V	1000R	1.7	140	2
	5236009150	13:36:57.01	−29:51:51.6	RK83	2018 04 22	580V	1000R	1.7	70	2
	5236009155	13:36:57.20	−29:51:56.0	RK83	2018 04 21	580V	1000R	2.0	70	0
	5236009162	13:36:57.70	−29:46:58.6	RK83	2017 07 29	580V	1000R	1.7	173	0
	5236009170	13:36:58.31	−29:52:02.6	RK83	2017 07 28	580V	1000R	2.0	104	0
	5236009182	13:36:59.39	−29:51:17.6	RK83	2017 07 29	580V	1000R	1.7	173	1
	5236009205	13:37:01.08	−29:51:33.6	RK83	2018 04 22	580V	1000R	1.7	140	1
	5236009260	13:37:06.92	−29:48:42.6	RK83	2017 07 27	580V	1000R	1.7	152	1
	5236009278	13:37:08.00	−29:54:41.6	RK83	2017 07 29	580V	1000R	1.7	173	1
	5236009284	13:37:08.38	−29:48:51.6	RK83	2017 07 28	580V	1000R	2.0	104	2
	5236009295	13:37:09.15	−29:49:06.6	RK83	2018 04 21	580V	1000R	2.0	70	4
	5236009313	13:37:10.16	−29:54:40.6	RK83	2018 04 21	580V	1000R	2.0	70	1
	5236009316	13:37:10.78	−29:55:46.6	RK83	2017 07 27	580V	1000R	1.7	152	0
	5236009329	13:37:13.77	−29:54:09.6	RK83	2018 04 22	580V	1000R	1.7	70	0
	5236009331	13:37:14.62	−29:53:55.6	RK83	2017 07 28	580V	1000R	2.0	104	0
	5236009342	13:37:17.15	−29:50:49.6	RK83	2017 07 29	580V	1000R	1.7	173	0
	5236009346	13:37:18.76	−29:51:59.6	RK83	2017 07 27	580V	1000R	1.7	152	0
	5236009348	13:37:19.29	−29:48:33.6	RK83	2018 04 22	580V	1000R	1.7	140	0
	5236009355	13:37:25.45	−29:50:52.6	RK83	2017 07 28	580V	1000R	2.0	104	0
	5236009356	13:37:25.74	−29:47:25.6	RK83	2017 07 29	580V	1000R	1.7	173	0
	5236009357	13:37:26.07	−29:51:27.6	RK83	2018 04 21	580V	1000R	2.0	70	0
	5236009358	13:37:26.53	−29:51:16.6	RK83	2018 04 22	580V	1000R	1.7	70	0
	5236010049	13:36:47.71	−29:46:28.1	SSTSL	2017 07 27	580V	1000R	1.7	152	0
	5236010172	13:36:58.52	−29:59:24.5	SSTSL	2017 07 29	580V	1000R	1.7	173	1
	5236010183	13:36:59.62	−30:06:21.0	SSTSL	2017 07 29	580V	1000R	1.7	173	0
	5236010338	13:37:16.42	−30:00:47.6	SSTSL	2017 07 27	580V	1000R	1.7	152	1
	5236010349	13:37:19.35	−29:57:40.3	SSTSL	2017 07 29	580V	1000R	1.7	173	0
NGC 628	628001003	01:36:42.38	15:47:07.4	H76	2017 07 26	580V	385R	3.7	72	0
(M74)	628001026	01:36:42.91	15:47:22.2	H76	2017 07 27	580V	1000R	2.4	78	1
	628001677	01:36:27.20	15:46:29.1	H76	2017 07 27	580V	1000R	2.4	78	1
	628001695	01:36:38.25	15:43:23.8	H76	2017 07 27	580V	1000R	2.4	78	0
	628001701	01:36:30.67	15:44:24.2	H76	2017 07 26	580V	385R	3.7	72	0
	628001714	01:36:27.24	15:48:48.8	H76	2017 07 26	580V	385R	3.7	72	0
	628001720	01:36:58.55	15:46:50.7	H76	2017 07 26	580V	385R	3.7	72	0
	628001724	01:36:59.15	15:46:26.7	H76	2017 07 27	580V	1000R	2.4	78	1

Table A2. Emission line fluxes (units 10^{-16} erg s^{-1} cm^{-2}) of the set of lines used in the series of metallicity calculations, for the integrated set of 92 confirmed H II regions in the SAMI Zoom Survey. Emission lines with flux values lower than their 3σ uncertainties are reported as 3σ upper limits. A more extensive list of the entire set of measured emission line fluxes is available online (see Section 6). Region names may be matched with corresponding targets in Table A1 by taking the number before the decimal point (e.g. region 300003026.2 is positioned within target 300003026).

ID	Region	[O II] λ3726	[O II] λ3729	[O III] λ4363	H β λ4861	[O III] λ5007	H α λ6563	[N II] λ6584	[S II] λ6716	[S II] λ6731
0	300002271.0	523.15 ± 0.80	590.97 ± 0.80	23.29 ± 0.80	635.09 ± 0.80	2389.37 ± 0.80	2004.9 ± 1.4	79.8 ± 1.4	109.4 ± 1.4	76.7 ± 1.4
1	300003026.0	247.94 ± 0.48	293.36 ± 0.48	< 2	273.00 ± 0.48	288.19 ± 0.48	904.02 ± 0.56	145.89 ± 0.56	84.46 ± 0.56	60.66 ± 0.56
2	300003026.2	347.4 ± 1.1	398.6 ± 1.1	< 3	257.6 ± 1.1	164.8 ± 1.1	830.5 ± 2.1	230.0 ± 2.1	224.5 ± 2.1	162.5 ± 2.1
3	300003096.0	563.43 ± 0.85	699.20 ± 0.85	< 2	395.77 ± 0.85	157.99 ± 0.85	1139.60 ± 0.87	252.85 ± 0.87	225.92 ± 0.87	161.61 ± 0.87
5	300003167.0	62.61 ± 0.25	74.40 ± 0.25	< 0.9	43.14 ± 0.25	36.34 ± 0.25	143.81 ± 0.41	20.07 ± 0.41	16.76 ± 0.41	11.59 ± 0.41
6	300003198.0	85.06 ± 0.25	122.59 ± 0.25	1.52 ± 0.25	90.11 ± 0.25	259.89 ± 0.25	271.85 ± 0.32	21.26 ± 0.32	18.40 ± 0.32	13.22 ± 0.32
7	300003242.0	187.3 ± 1.7	216.3 ± 1.7	< 6	109.1 ± 1.7	355.8 ± 1.7	349.01 ± 0.76	34.31 ± 0.76	41.26 ± 0.76	28.47 ± 0.76
8	300003247.0	372.65 ± 0.52	419.87 ± 0.52	2.37 ± 0.52	234.37 ± 0.52	246.73 ± 0.52	720.75 ± 0.64	91.80 ± 0.64	158.65 ± 0.64	112.32 ± 0.64
11	300006042.0	415.43 ± 0.91	513.12 ± 0.91	< 3	379.03 ± 0.91	243.18 ± 0.91	1168.19 ± 0.96	252.16 ± 0.96	185.86 ± 0.96	132.08 ± 0.96
13	300006151.1	235.98 ± 0.90	293.41 ± 0.90	< 3	135.78 ± 0.90	178.01 ± 0.90	415.7 ± 1.6	61.9 ± 1.6	55.3 ± 1.6	38.9 ± 1.6
14	300006151.2	36.98 ± 0.41	47.92 ± 0.41	< 1	21.54 ± 0.41	32.16 ± 0.41	69.25 ± 0.52	10.54 ± 0.52	9.83 ± 0.52	6.79 ± 0.52
15	300006152.0	228.89 ± 0.89	280.58 ± 0.89	< 3	163.46 ± 0.89	256.41 ± 0.89	528.6 ± 1.1	78.6 ± 1.1	76.5 ± 1.1	53.6 ± 1.1
16	300006169.1	101.10 ± 0.49	131.20 ± 0.49	< 2	80.77 ± 0.49	67.82 ± 0.49	264.57 ± 0.72	35.93 ± 0.72	37.91 ± 0.72	26.21 ± 0.72
17	300006169.2	28.74 ± 0.39	34.33 ± 0.39	< 1	21.74 ± 0.39	5.39 ± 0.39	63.79 ± 0.43	11.50 ± 0.43	15.99 ± 0.43	11.14 ± 0.43
20	300006181.1	10.78 ± 0.73	9.78 ± 0.73	< 2	4.38 ± 0.73	6.66 ± 0.73	10.68 ± 0.84	< 2	< 2	< 2
21	300006182.0	69.28 ± 0.45	99.21 ± 0.45	< 2	53.68 ± 0.45	90.23 ± 0.45	159.34 ± 0.85	24.43 ± 0.85	25.17 ± 0.85	17.70 ± 0.85
22	300006189.0	25.23 ± 0.46	29.97 ± 0.46	< 2	22.08 ± 0.46	5.29 ± 0.46	64.3 ± 1.1	11.1 ± 1.1	13.5 ± 1.1	9.5 ± 1.1
29	300006248.0	< 0.3	< 0.3	< 0.3	< 0.3	4.97 ± 0.14	1.78 ± 0.13	< 0.3	< 0.3	< 0.3
31	300006262.0	500.78 ± 0.91	547.53 ± 0.91	8.93 ± 0.91	365.47 ± 0.91	947.19 ± 0.91	1190.5 ± 1.1	94.5 ± 1.1	144.4 ± 1.1	103.2 ± 1.1
33	300008108.0	161.41 ± 0.64	195.65 ± 0.64	< 2	168.56 ± 0.64	118.94 ± 0.64	552 ± 1	91 ± 1	67 ± 1	46 ± 1
35	300008185.3	25.92 ± 0.32	31.28 ± 0.32	< 0.9	17.19 ± 0.32	6.29 ± 0.32	54.52 ± 0.60	9.29 ± 0.60	16.69 ± 0.60	11.69 ± 0.60
39	300009011.0	117.99 ± 0.89	144.55 ± 0.89	< 3	157.11 ± 0.89	127.13 ± 0.89	525.1 ± 1.2	151.1 ± 1.2	90.2 ± 1.2	66.5 ± 1.2
40	300009050.0	70.54 ± 0.56	85.17 ± 0.56	< 2	80.84 ± 0.56	19.94 ± 0.56	245.60 ± 0.82	65.67 ± 0.82	55.48 ± 0.82	38.41 ± 0.82
41	300009180.0	279.3 ± 1.4	354.5 ± 1.4	11.9 ± 1.4	355.8 ± 1.4	1865.2 ± 1.4	1109.1 ± 1.8	103.7 ± 1.8	118.7 ± 1.8	84.1 ± 1.8
43	300009275.0	228.38 ± 0.40	247.71 ± 0.40	4.98 ± 0.40	181.85 ± 0.40	510.07 ± 0.40	527.32 ± 0.83	25.64 ± 0.83	28.31 ± 0.83	20.37 ± 0.83
51	3521003210.0	12.9 ± 1.1	7.4 ± 1.1	< 3	10.2 ± 1.1	12.9 ± 1.1	43.1 ± 1.4	14.0 ± 1.4	9.0 ± 1.4	6.1 ± 1.4
53	3521003295.1	15 ± 1	13 ± 1	< 3	34 ± 1	11 ± 1	155.9 ± 1.6	72.5 ± 1.6	29.6 ± 1.6	21.2 ± 1.6
54	3521003295.2	29.3 ± 2.5	28.2 ± 2.5	< 9	69.3 ± 2.5	21.8 ± 2.5	277.6 ± 3.7	114.7 ± 3.7	49.8 ± 3.7	36.0 ± 3.7
60	3621001001.0	38.42 ± 0.75	44.57 ± 0.75	< 2	56.40 ± 0.75	16.85 ± 0.75	200.3 ± 1.2	61.7 ± 1.2	36.5 ± 1.2	25.2 ± 1.2
61	3621001001.3	17.18 ± 0.43	22.67 ± 0.43	< 1	29.17 ± 0.43	16.39 ± 0.43	127.75 ± 0.66	37.45 ± 0.66	26.95 ± 0.66	18.17 ± 0.66
62	3621001001.4	110 ± 2	140 ± 2	< 6	183 ± 2	65 ± 2	832.7 ± 5.1	253.4 ± 5.1	167.3 ± 5.1	119.1 ± 5.1
63	3621001019.0	74.83 ± 0.38	85.85 ± 0.38	1.75 ± 0.38	97.67 ± 0.38	315.81 ± 0.38	352.1 ± 3.3	28.6 ± 3.3	22.7 ± 3.3	16.2 ± 3.3
66	3621005021.0	19.78 ± 0.67	23.09 ± 0.67	< 2	12.54 ± 0.67	23.69 ± 0.67	42.62 ± 0.45	2.89 ± 0.45	4.27 ± 0.45	3.05 ± 0.45
67	3621005022.0	13.83 ± 0.81	18.96 ± 0.81	< 2	9.38 ± 0.81	11.84 ± 0.81	30.38 ± 0.58	2.35 ± 0.58	3.24 ± 0.58	2.02 ± 0.58
68	3621005023.0	6.20 ± 0.52	3.27 ± 0.52	< 2	3.31 ± 0.52	8.24 ± 0.52	11.09 ± 0.35	< 0.9	1.69 ± 0.35	< 0.9
70	3621005026.1	10.87 ± 0.78	13.11 ± 0.78	< 2	6.51 ± 0.78	15.04 ± 0.78	21.38 ± 0.76	< 2	3.55 ± 0.76	2.50 ± 0.76
71	3621005026.2	6.19 ± 0.41	4.47 ± 0.41	< 1	3.02 ± 0.41	9.50 ± 0.41	11.02 ± 0.41	< 1	< 1	< 1
72	3621005032.0	6.93 ± 0.76	10.73 ± 0.76	< 2	5.19 ± 0.76	6.73 ± 0.76	14.66 ± 0.55	< 2	2.33 ± 0.55	< 2
73	3621005033.0	35.4 ± 1.2	31.2 ± 1.2	< 3	16.3 ± 1.2	9.4 ± 1.2	51.2 ± 1.3	6.0 ± 1.3	11.3 ± 1.3	8.4 ± 1.3
74	3621005034.0	5.49 ± 0.65	8.19 ± 0.65	< 2	3.30 ± 0.65	3.78 ± 0.65	11.15 ± 0.68	< 2	< 2	< 2
75	3621005037.0	8.25 ± 0.67	13.03 ± 0.67	< 2	6.87 ± 0.67	10.14 ± 0.67	23.37 ± 0.49	2.05 ± 0.49	2.75 ± 0.49	1.70 ± 0.49
78	3621005055.0	84.7 ± 1.8	97.5 ± 1.8	< 6	114.3 ± 1.8	76.5 ± 1.8	524.9 ± 2.4	159.4 ± 2.4	65.2 ± 2.4	47.8 ± 2.4
81	3621005057.0	31.60 ± 0.61	41.16 ± 0.61	< 2	55.50 ± 0.61	26.41 ± 0.61	288.5 ± 1.7	90.9 ± 1.7	45.6 ± 1.7	33.2 ± 1.7
82	3621005057.2	112.4 ± 2.4	163.0 ± 2.4	< 6	237.1 ± 2.4	59.8 ± 2.4	1043.6 ± 7.3	371.4 ± 7.3	203.2 ± 7.3	147.0 ± 7.3
83	3621005067.0	16.34 ± 0.41	24.46 ± 0.41	< 1	13.80 ± 0.41	9.64 ± 0.41	46.68 ± 0.85	9.79 ± 0.85	7.28 ± 0.85	5.32 ± 0.85

Table A2 – *continued*

ID	Region	[O II] λ3726	[O II] λ3729	[O III] λ4363	H β λ4861	[O III] λ5007	H α λ6563	[N II] λ6584	[S II] λ6716	[S II] λ6731
85	3621005069.0	12.23 ± 0.66	16.28 ± 0.66	< 2	6.41 ± 0.66	14.48 ± 0.66	27.02 ± 0.64	3.44 ± 0.64	5.99 ± 0.64	4.28 ± 0.64
86	3621005069.3	20.76 ± 0.70	35.16 ± 0.70	< 2	15.43 ± 0.70	36.58 ± 0.70	52.69 ± 0.91	5.67 ± 0.91	7.91 ± 0.91	5.84 ± 0.91
87	3621005069.4	17.58 ± 0.67	23.17 ± 0.67	< 2	9.26 ± 0.67	26.84 ± 0.67	33.98 ± 0.76	4.69 ± 0.76	7.51 ± 0.76	5.64 ± 0.76
88	3621005070.1	32.95 ± 0.26	42.17 ± 0.26	< 0.9	41.22 ± 0.26	146.81 ± 0.26	129.46 ± 0.90	7.40 ± 0.90	6.78 ± 0.90	5.10 ± 0.90
89	3621005070.2	31.64 ± 0.72	34.04 ± 0.72	< 2	26.42 ± 0.72	96.32 ± 0.72	83.7 ± 1.2	6.8 ± 1.2	9.6 ± 1.2	7.0 ± 1.2
90	3621005086.0	22.01 ± 0.39	24.72 ± 0.39	< 1	13.19 ± 0.39	26.21 ± 0.39	46.72 ± 0.60	3.79 ± 0.60	4.97 ± 0.60	3.78 ± 0.60
91	3621005087.0	10.73 ± 0.50	13.08 ± 0.50	< 2	6.88 ± 0.50	8.22 ± 0.50	20.39 ± 0.46	2.19 ± 0.46	2.06 ± 0.46	1.76 ± 0.46
92	3621005089.0	6.56 ± 0.64	6.14 ± 0.64	< 2	3.55 ± 0.64	4.22 ± 0.64	12.38 ± 0.58	1.78 ± 0.58	< 2	1.82 ± 0.58
93	3621005090.0	6.80 ± 0.42	10.08 ± 0.42	< 1	4.72 ± 0.42	4.66 ± 0.42	14.37 ± 0.40	1.84 ± 0.40	1.40 ± 0.40	1.32 ± 0.40
94	3621005091.0	25.31 ± 0.52	32.74 ± 0.52	< 2	15.91 ± 0.52	13.09 ± 0.52	50.12 ± 0.66	4.04 ± 0.66	5.74 ± 0.66	4.32 ± 0.66
95	5068001006.1	85.8 ± 1.2	97.4 ± 1.2	< 3	106.2 ± 1.2	150.9 ± 1.2	420.8 ± 6.1	100.2 ± 6.1	59.4 ± 6.1	45.2 ± 6.1
96	5068001006.2	45.58 ± 0.73	53.43 ± 0.73	< 2	45.09 ± 0.73	26.62 ± 0.73	160.0 ± 2.1	48.8 ± 2.1	40.4 ± 2.1	28.8 ± 2.1
106	5068002272.0	19.35 ± 0.44	27.41 ± 0.44	< 1	18.45 ± 0.44	10.17 ± 0.44	62.12 ± 0.71	19.15 ± 0.71	15.91 ± 0.71	11.23 ± 0.71
108	5068002323.0	124.93 ± 0.79	159.51 ± 0.79	< 2	134.07 ± 0.79	210.77 ± 0.79	492.0 ± 2.7	73.4 ± 2.7	54.4 ± 2.7	39.3 ± 2.7
118	5201001038.0	64 ± 3	74 ± 3	< 9	51 ± 3	117 ± 3	163.73 ± 0.57	14.42 ± 0.57	17.95 ± 0.57	12.38 ± 0.57
119	5201001038.2	7.00 ± 0.56	9.77 ± 0.56	< 2	7.00 ± 0.56	12.90 ± 0.56	24.85 ± 0.25	2.04 ± 0.25	2.86 ± 0.25	2.08 ± 0.25
120	5201001053.1	11.47 ± 0.93	23.00 ± 0.93	< 3	10.33 ± 0.93	17.93 ± 0.93	33.07 ± 0.65	5.21 ± 0.65	8.39 ± 0.65	5.96 ± 0.65
123	5201001069.0	221.2 ± 4.1	284.2 ± 4.1	< 10	290.5 ± 4.1	730.8 ± 4.1	1012.0 ± 2.5	117.3 ± 2.5	90.3 ± 2.5	65.3 ± 2.5
124	5201001075.0	23.18 ± 0.69	23.41 ± 0.69	< 2	15.08 ± 0.69	36.00 ± 0.69	49.74 ± 0.57	3.23 ± 0.57	6.22 ± 0.57	4.45 ± 0.57
125	5201001133.1	13.9 ± 1.1	25.4 ± 1.1	< 3	13.5 ± 1.1	39.7 ± 1.1	42.86 ± 0.74	2.84 ± 0.74	6.12 ± 0.74	4.25 ± 0.74
126	5201001133.2	47.37 ± 0.84	59.85 ± 0.84	< 2	28.49 ± 0.84	54.29 ± 0.84	82.77 ± 0.48	5.07 ± 0.48	11.30 ± 0.48	7.92 ± 0.48
132	5236004216.0	177.9 ± 1.2	219.0 ± 1.2	< 3	511.4 ± 1.2	109.4 ± 1.2	2277 ± 36	851 ± 36	238 ± 36	170 ± 36
133	5236004309.0	516.6 ± 1.8	644.3 ± 1.8	< 6	789.5 ± 1.8	701.7 ± 1.8	2806 ± 43	947 ± 43	311 ± 43	222 ± 43
134	5236004341.0	98.0 ± 1.1	120.2 ± 1.1	< 3	286.1 ± 1.1	72.3 ± 1.1	1331 ± 22	564 ± 22	202 ± 22	148 ± 22
135	5236006127.0	22.81 ± 0.29	28.70 ± 0.29	< 0.9	20.93 ± 0.29	56.57 ± 0.29	72.17 ± 0.92	10.18 ± 0.92	4.60 ± 0.92	3.10 ± 0.92
140	5236009025.0	15.43 ± 0.25	8.53 ± 0.25	< 0.9	28.45 ± 0.25	22.73 ± 0.25	114.5 ± 2.3	49.9 ± 2.3	11.4 ± 2.3	8.8 ± 2.3
142	5236009030.1	28.24 ± 0.69	30.36 ± 0.69	< 2	45.27 ± 0.69	11.62 ± 0.69	149.7 ± 3.2	81.2 ± 3.2	39.4 ± 3.2	28.1 ± 3.2
144	5236009045.1	42.84 ± 0.82	56.50 ± 0.82	< 2	69.15 ± 0.82	27.99 ± 0.82	261.3 ± 5.9	134.4 ± 5.9	54.4 ± 5.9	38.1 ± 5.9
145	5236009045.2	11.42 ± 0.25	10.59 ± 0.25	< 0.6	6.88 ± 0.25	8.13 ± 0.25	33.59 ± 0.98	27.38 ± 0.98	9.49 ± 0.98	6.82 ± 0.98
146	5236009150.0	59.6 ± 2.4	73.2 ± 2.4	< 6	120.2 ± 2.4	34.0 ± 2.4	307.9 ± 7.4	178.6 ± 7.4	76.8 ± 7.4	56.1 ± 7.4
147	5236009150.2	9.11 ± 0.51	7.50 ± 0.51	< 2	10.09 ± 0.51	4.48 ± 0.51	32.15 ± 0.84	19.35 ± 0.84	7.77 ± 0.84	5.72 ± 0.84
154	5236009182.0	106.5 ± 2.8	138.6 ± 2.8	< 9	171.4 ± 2.8	81.1 ± 2.8	618 ± 15	324 ± 15	143 ± 15	105 ± 15
156	5236009205.2	207.8 ± 4.2	212.3 ± 4.2	< 10	794.7 ± 4.2	153.2 ± 4.2	3119 ± 74	1768 ± 74	626 ± 74	515 ± 74
157	5236009260.0	51.2 ± 3.2	101.0 ± 3.2	< 9	109.3 ± 3.2	66.5 ± 3.2	363.0 ± 8.2	177.4 ± 8.2	82.1 ± 8.2	63.9 ± 8.2
159	5236009278.0	97.3 ± 1.1	118.6 ± 1.1	< 3	243.2 ± 1.1	57.1 ± 1.1	910 ± 17	348 ± 17	164 ± 17	117 ± 17
160	5236009284.0	35.51 ± 0.56	46.17 ± 0.56	< 2	38.53 ± 0.56	15.98 ± 0.56	136.1 ± 3.5	67.1 ± 3.5	36.2 ± 3.5	25.5 ± 3.5
161	5236009284.2	63.86 ± 0.81	82.94 ± 0.81	< 2	97.94 ± 0.81	42.11 ± 0.81	378.3 ± 7.6	174.9 ± 7.6	75.2 ± 7.6	53.0 ± 7.6
162	5236009295.2	80 ± 1	107 ± 1	< 3	113 ± 1	49 ± 1	362.0 ± 7.7	146.8 ± 7.7	69.2 ± 7.7	49.7 ± 7.7
163	5236009295.3	50.8 ± 1.1	50.0 ± 1.1	< 3	67.3 ± 1.1	47.1 ± 1.1	210.5 ± 4.2	71.9 ± 4.2	29.7 ± 4.2	20.9 ± 4.2
164	5236009295.5	136.24 ± 0.91	175.58 ± 0.91	< 3	200.27 ± 0.91	238.95 ± 0.91	657 ± 11	207 ± 11	73 ± 11	51 ± 11
165	5236009295.6	76.53 ± 0.83	102.81 ± 0.83	< 2	110.69 ± 0.83	47.64 ± 0.83	346.9 ± 5.9	143.1 ± 5.9	66.3 ± 5.9	46.9 ± 5.9
166	5236009313.0	58.55 ± 0.88	79.52 ± 0.88	< 3	109.03 ± 0.88	28.42 ± 0.88	347.2 ± 6.4	168.7 ± 6.4	77.5 ± 6.4	56.2 ± 6.4
182	5236010172.0	78.13 ± 0.21	92.94 ± 0.21	0.67 ± 0.21	78.04 ± 0.21	147.03 ± 0.21	277.4 ± 3.8	63.9 ± 3.8	19.1 ± 3.8	13.7 ± 3.8
186	5236010338.0	6.79 ± 0.30	8.85 ± 0.30	< 0.9	5.94 ± 0.30	7.77 ± 0.30	16.29 ± 0.40	3.33 ± 0.40	1.77 ± 0.40	1.40 ± 0.40
190	628001026.0	7.2 ± 1.1	11.1 ± 1.1	< 3	8.9 ± 1.1	6.4 ± 1.1	42.6 ± 2.2	18.8 ± 2.2	9.9 ± 2.2	6.9 ± 2.2
191	628001677.0	41.8 ± 2.4	52.5 ± 2.4	< 6	81.0 ± 2.4	225.7 ± 2.4	178.0 ± 3.2	23.1 ± 3.2	12.6 ± 3.2	< 9
196	628001724.0	95.6 ± 1.2	130.3 ± 1.2	< 3	80.2 ± 1.2	160.6 ± 1.2	266.7 ± 5.9	53.8 ± 5.9	52.6 ± 5.9	36.8 ± 5.9

Table A3. The physical parameters of the 92 confirmed H II regions in the SAMI Zoom Survey, measured where possible using their integrated spectra. Values of marked with an asterisk (∗) were determined assuming an [O III] electron temperature of 1×10^4 K.

ID	Region	T_e([OIII]) ($\times 10^4$ K)	T_e([OII]) ($\times 10^4$ K)	n_e (cm^{-1})	log(q)	R_{23} Branch
0	300002271.0	1.138 ± 0.013	1.31 ± 0.10	12 ± 16	8.0150 ± 0.0009	Upper
1	300003026.0	–	–	39 ± 13 ∗	7.6761 ± 0.0011	Upper
2	300003026.2	–	–	46 ± 14 ∗	7.3113 ± 0.0027	Upper
3	300003096.0	–	–	35.6 ± 6.6 ∗	7.1749 ± 0.0016	Upper
5	300003167.0	–	–	3 ± 33 ∗	7.3218 ± 0.0028	Upper
6	300003198.0	0.972 ± 0.039	1.074 ± 0.088	39 ± 24	7.8522 ± 0.0017	Upper
7	300003242.0	–	–	2 ± 22 ∗	7.5545 ± 0.0075	Upper
8	300003247.0	1.128 ± 0.072	1.252 ± 0.076	21.9 ± 6.6	7.38831 ± 0.00096	Upper
11	300006042.0	–	–	28.9 ± 8.1 ∗	7.4293 ± 0.0016	Upper
13	300006151.1	–	–	20 ± 35 ∗	7.3643 ± 0.0031	Upper
14	300006151.2	–	–	2 ± 67 ∗	7.3646 ± 0.0068	Upper
15	300006152.0	–	–	16 ± 24 ∗	7.5123 ± 0.0024	Upper
16	300006169.1	–	–	3 ± 29 ∗	7.3869 ± 0.0031	Upper
17	300006169.2	–	–	10 ± 28 ∗	7.08 ± 0.02	Upper
20	300006181.1	–	–	–	7.408 ± 0.062	Upper
21	300006182.0	–	–	19 ± 37 ∗	7.5705 ± 0.0043	Upper
22	300006189.0	–	–	21 ± 117 ∗	7.137 ± 0.025	Upper
29	300006248.0	–	–	–	–	Lower
31	300006262.0	1.131 ± 0.033	1.229 ± 0.058	31 ± 15	7.6600 ± 0.0014	Upper
33	300008108.0	–	–	8 ± 18 ∗	7.5121 ± 0.0028	Upper
35	300008185.3	–	–	15 ± 44 ∗	7.087 ± 0.015	Upper
39	300009011.0	–	–	65 ± 27 ∗	7.6890 ± 0.0037	Upper
40	300009050.0	–	–	5 ± 16 ∗	7.2499 ± 0.0078	Upper
41	300009180.0	0.999 ± 0.031	1.127 ± 0.094	26 ± 19	8.0025 ± 0.0029	Upper
43	300009275.0	1.123 ± 0.031	1.203 ± 0.086	39 ± 39	7.7898 ± 0.0013	Upper
51	3521003210.0	–	–	–	7.588 ± 0.055	Upper
53	3521003295.1	–	–	33 ± 111 ∗	7.585 ± 0.036	Upper
54	3521003295.2	–	–	44 ± 164 ∗	7.625 ± 0.052	Upper
60	3621001001.0	–	–	2 ± 45 ∗	7.375 ± 0.016	Upper
61	3621001001.3	–	–	–	7.536 ± 0.012	Upper
62	3621001001.4	–	–	28 ± 54 ∗	7.363 ± 0.011	Upper
63	3621001019.0	0.980 ± 0.048	1.09 ± 0.10	33 ± 460	7.9803 ± 0.0028	Upper
66	3621005021.0	–	–	32 ± 143 ∗	7.472 ± 0.022	Upper
67	3621005022.0	–	–	–	7.389 ± 0.034	Upper
68	3621005023.0	–	–	–	7.640 ± 0.061	Upper
70	3621005026.1	–	–	–	7.486 ± 0.048	Lower
71	3621005026.2	–	–	–	7.51 ± 0.05	Upper
72	3621005032.0	–	–	–	7.484 ± 0.075	Upper
73	3621005033.0	–	–	79 ± 218 ∗	7.112 ± 0.036	Upper
74	3621005034.0	–	–	–	7.247 ± 0.082	Upper
75	3621005037.0	–	–	–	7.47 ± 0.05	Upper
78	3621005055.0	–	–	57 ± 77 ∗	7.4837 ± 0.0099	Upper
81	3621005057.0	–	–	49 ± 100 ∗	7.42 ± 0.01	Upper
82	3621005057.2	–	–	44 ± 65 ∗	7.336 ± 0.013	Upper
83	3621005067.0	–	–	55 ± 264 ∗	7.301 ± 0.019	Upper
85	3621005069.0	–	–	33 ± 373 ∗	7.330 ± 0.034	Upper
86	3621005069.3	–	–	66 ± 225 ∗	7.48 ± 0.02	Upper
87	3621005069.4	–	–	83 ± 209 ∗	7.445 ± 0.026	Upper
88	3621005070.1	–	–	86 ± 248 ∗	7.9932 ± 0.0047	Upper
89	3621005070.2	–	–	47 ± 298 ∗	7.800 ± 0.017	Upper
90	3621005086.0	–	–	96 ± 376 ∗	7.441 ± 0.011	Upper
91	3621005087.0	–	–	240 ± 607 ∗	7.428 ± 0.036	Upper
92	3621005089.0	–	–	–	7.322 ± 0.076	Upper
93	3621005090.0	–	–	395 ± 14018 ∗	7.344 ± 0.041	Upper
94	3621005091.0	–	–	88 ± 219 ∗	7.266 ± 0.016	Upper
95	5068001006.1	–	–	97 ± 394 ∗	7.7503 ± 0.0062	Upper
96	5068001006.2	–	–	31 ± 89 ∗	7.3927 ± 0.0095	Upper
106	5068002272.0	–	–	22 ± 68 ∗	7.318 ± 0.014	Upper
108	5068002323.0	–	–	44 ± 74 ∗	7.6855 ± 0.0033	Upper
118	5201001038.0	–	–	1 ± 29 ∗	7.684 ± 0.032	Upper
119	5201001038.2	–	–	50 ± 176 ∗	7.662 ± 0.046	Upper
120	5201001053.1	–	–	29 ± 135	7.499 ± 0.042	Upper

Table A3 – *continued*

ID	Region	T_e([OIII]) ($\times 10^4$ K)	T_e([OII]) ($\times 10^4$ K)	n_e (cm^{-1})	log(q)	R_{23} Branch
123	5201001069.0	–	–	45 ± 46 *	7.9386 ± 0.0092	Upper
124	5201001075.0	–	–	35 ± 114 *	7.594 ± 0.022	Upper
125	5201001133.1	–	–	8 ± 245 *	7.678 ± 0.045	Upper
126	5201001133.2	–	–	16 ± 51 *	7.498 ± 0.013	Upper
132	5236004216.0	–	–	–	7.463 ± 0.004	Upper
133	5236004309.0	–	–	33 ± 400 *	7.7656 ± 0.0014	Upper
134	5236004341.0	–	–	59 ± 359 *	7.5142 ± 0.0068	Upper
135	5236006127.0	–	–	–	7.7308 ± 0.0077	Upper
140	5236009025.0	–	–	–	7.989 ± 0.008	Upper
142	5236009030.1	–	–	32 ± 114 *	7.416 ± 0.026	Upper
144	5236009045.1	–	–	14 ± 400 *	7.465 ± 0.012	Upper
145	5236009045.2	–	–	37 ± 627 *	7.219 ± 0.015	Upper
146	5236009150.0	–	–	57 ± 122 *	7.647 ± 0.026	Upper
147	5236009150.2	–	–	63 ± 164 *	7.508 ± 0.049	Upper
154	5236009182.0	–	–	60 ± 617 *	7.546 ± 0.016	Upper
156	5236009205.2	–	–	187 ± 637 *	7.671 ± 0.011	Upper
157	5236009260.0	–	–	123 ± 229 *	7.696 ± 0.024	Upper
159	5236009278.0	–	–	34 ± 207 *	7.5097 ± 0.0078	Upper
160	5236009284.0	–	–	21 ± 208 *	7.302 ± 0.013	Upper
161	5236009284.2	–	–	20 ± 276 *	7.4531 ± 0.0077	Upper
162	5236009295.2	–	–	39 ± 168 *	7.5039 ± 0.0084	Upper
163	5236009295.3	–	–	20 ± 252 *	7.738 ± 0.013	Upper
164	5236009295.5	–	–	17 ± 261 *	7.8728 ± 0.0027	Upper
165	5236009295.6	–	–	25 ± 143 *	7.5137 ± 0.0078	Upper
166	5236009313.0	–	–	49 ± 159 *	7.449 ± 0.012	Upper
182	5236010172.0	0.932 ± 0.038	–	–	7.7239 ± 0.0016	Upper
186	5236010338.0	–	–	141 ± 1364 *	7.663 ± 0.029	Upper
190	628001026.0	–	–	–	7.336 ± 0.087	Upper
191	628001677.0	–	–	52 ± 452 *	8.481 ± 0.035	Upper
196	628001724.0	–	–	15 ± 261 *	7.6132 ± 0.0075	Upper

Table A4. The measured metallicities of the 92 confirmed H II regions in the SAMI Zoom Survey using their integrated spectra. Values marked with an asterisk (∗) fall outside the valid metallicity ranges for which their respective methods were calibrated, thus may be unreliable; these values were not considered throughout further analysis in this work.

ID	Region	R/R$_{25}$	Z_{T_e}	$Z_{R_{23}}$	Z_{N2O2}	Z_{N2S2}	$Z_{\mathrm{N2H}\alpha}$	$Z_{\mathrm{N2S2H}\alpha}$	Z_{O3N2}
0	300002271.0	1.031	8.047 ± 0.017	8.69481 ± 0.00086	8.351 ± 0.011	7.889 ± 0.078 ∗	8.1192 ± 0.0034	8.028 ± 0.013	8.1112 ± 0.0019 ∗
1	300003026.0	0.105	–	8.96775 ± 0.00064	8.7973 ± 0.0014	8.72 ± 0.16	8.3932 ± 0.0013	8.5668 ± 0.0037	8.35994 ± 0.00051
2	300003026.2	0.105	–	8.9251 ± 0.0017	8.8433 ± 0.0023	8.47 ± 0.15	8.5740 ± 0.0049	8.4000 ± 0.0075	8.4564 ± 0.0013
3	300003096.0	0.277	–	8.95169 ± 0.00084	8.78729 ± 0.00097	8.53 ± 0.28	8.4918 ± 0.0011	8.4122 ± 0.0022	8.47852 ± 0.00061
5	300003167.0	0.572	–	8.8597 ± 0.0029	8.6151 ± 0.0072	8.56 ± 0.18	8.3549 ± 0.0053	8.398 ± 0.018	8.3675 ± 0.0027
6	300003198.0	0.799	8.311 ± 0.063	8.7414 ± 0.0018	8.5511 ± 0.0063	8.378 ± 0.016	8.2327 ± 0.0026	8.307 ± 0.011	8.1983 ± 0.0015 ∗
7	300003242.0	0.867	–	8.492 ± 0.017	8.427 ± 0.012	8.13 ± 0.16 ∗	8.276 ± 0.005	8.198 ± 0.017	8.2087 ± 0.0024
8	300003247.0	0.859	8.380 ± 0.084	8.8353 ± 0.0012	8.5851 ± 0.0029	7.88 ± 0.10 ∗	8.3329 ± 0.0019	8.0607 ± 0.0049	8.33746 ± 0.00084
11	300006042.0	0.186	–	8.98003 ± 0.00088	8.8333 ± 0.0012	8.61 ± 0.25	8.4823 ± 0.0014	8.4955 ± 0.0028	8.43253 ± 0.00057
13	300006151.1	0.389	–	8.7432 ± 0.0052	8.5911 ± 0.0099	8.52 ± 0.29	8.3718 ± 0.0077	8.371 ± 0.018	8.3316 ± 0.0025
14	300006151.2	0.389	–	8.695 ± 0.014	8.581 ± 0.023	8.50 ± 0.26	8.377 ± 0.016	8.360 ± 0.034	8.3220 ± 0.0058
15	300006152.0	0.434	–	8.7884 ± 0.0032	8.651 ± 0.005	8.48 ± 0.26	8.3713 ± 0.0041	8.336 ± 0.013	8.3153 ± 0.0017
16	300006169.1	0.665	–	8.9002 ± 0.0027	8.6431 ± 0.0076	8.44 ± 0.21	8.3482 ± 0.0052	8.293 ± 0.014	8.3651 ± 0.0021
17	300006169.2	0.665	–	8.9938 ± 0.0066	8.753 ± 0.013	8.26 ± 0.20 ∗	8.425 ± 0.012	8.201 ± 0.022	8.5037 ± 0.0084
20	300006181.1	0.713	–	8.71 ± 0.11	8.65 ± 0.24	–	8.42 ± 0.16	8.2 ± 2.2	8.331 ± 0.057
21	300006182.0	0.525	–	8.796 ± 0.005	8.681 ± 0.012	8.26 ± 0.12 ∗	8.3795 ± 0.0098	8.312 ± 0.023	8.3109 ± 0.0039
22	300006189.0	0.570	–	9.0334 ± 0.0057	8.783 ± 0.028	8.36 ± 0.32	8.412 ± 0.027	8.252 ± 0.064	8.503 ± 0.013
29	300006248.0	1.157	–	–	–	–	8.0 ± 1.0	7.5 ± 7.7	7.94 ± 0.14 ∗
31	300006262.0	0.999	8.229 ± 0.053	8.6891 ± 0.0019	8.4389 ± 0.0067	7.57 ± 0.18 ∗	8.2353 ± 0.0023	8.0594 ± 0.0083	8.2103 ± 0.0011
33	300008108.0	0.306	–	8.9934 ± 0.0012	8.7913 ± 0.0034	8.62 ± 0.16	8.4015 ± 0.0038	8.475 ± 0.009	8.4001 ± 0.0012
35	300008185.3	0.522	–	8.9134 ± 0.0086	8.679 ± 0.022	7.53 ± 0.30 ∗	8.41 ± 0.02	8.081 ± 0.044	8.4630 ± 0.0076
39	300009011.0	0.073	–	9.0188 ± 0.0016	8.9635 ± 0.0021	8.70 ± 0.14	8.5894 ± 0.0044	8.6154 ± 0.0075	8.4385 ± 0.0012
40	300009050.0	0.163	–	9.0734 ± 0.0017	8.9354 ± 0.0029	9.25 ± 0.19 ∗	8.5602 ± 0.0052	8.4651 ± 0.0094	8.5411 ± 0.0031
41	300009180.0	0.531	8.361 ± 0.048	8.500 ± 0.004	8.6912 ± 0.0064	8.138 ± 0.026 ∗	8.2663 ± 0.0032	8.209 ± 0.012	8.1596 ± 0.0015 ∗
43	300009275.0	1.073	8.153 ± 0.056	8.7218 ± 0.0015	8.27 ± 0.31 ∗	9.25 ± 0.28 ∗	8.1524 ± 0.0055	8.144 ± 0.022	8.1563 ± 0.0032 ∗
51	3521003210.0	1.049	–	8.900 ± 0.053	8.911 ± 0.036	–	8.642 ± 0.071	8.62 ± 0.14	8.41 ± 0.02
53	3521003295.1	0.190	–	9.1133 ± 0.0061	9.1256 ± 0.0076	8.88 ± 0.17	8.821 ± 0.023 ∗	8.852 ± 0.035	8.57 ± 0.01
54	3521003295.2	0.190	–	9.1181 ± 0.0064	9.1216 ± 0.0094	8.85 ± 0.19	8.757 ± 0.029 ∗	8.805 ± 0.045	8.562 ± 0.012
60	3621001001.0	0.343	–	9.0848 ± 0.0027	8.9915 ± 0.0046	8.58 ± 0.18	8.618 ± 0.011	8.64 ± 0.02	8.5380 ± 0.0053
61	3621001001.3	0.343	–	9.0430 ± 0.0035	8.9615 ± 0.0053	9.25 ± 0.21 ∗	8.596 ± 0.012	8.559 ± 0.022	8.4768 ± 0.0037
62	3621001001.4	0.343	–	9.0618 ± 0.0024	8.9635 ± 0.0073	8.69 ± 0.14	8.612 ± 0.015	8.592 ± 0.028	8.522 ± 0.004
63	3621001019.0	0.660	8.23 ± 0.19	8.7548 ± 0.0023	8.63 ± 0.05	8.41 ± 0.23	8.240 ± 0.026	8.35 ± 0.11	8.193 ± 0.016 ∗
66	3621005021.0	2.084	–	8.69 ± 0.04	8.22 ± 0.26 ∗	8.16 ± 0.39 ∗	8.207 ± 0.037	8.06 ± 0.14	8.225 ± 0.019
67	3621005022.0	1.906	–	8.779 ± 0.049	8.32 ± 0.27 ∗	8.28 ± 0.47 ∗	8.231 ± 0.054	8.13 ± 0.29	8.275 ± 0.033
68	3621005023.0	1.833	–	8.69 ± 0.10	7.56 ± 0.30 ∗	–	8.17 ± 0.14	7.7 ± 4.7	8.179 ± 0.068 ∗
70	3621005026.1	1.725	–	8.61 ± 0.10	7.86 ± 0.29 ∗	–	8.17 ± 0.18	7.6 ± 19.0	8.19 ± 0.07 ∗
71	3621005026.2	1.725	–	8.48 ± 0.13	7.86 ± 0.22 ∗	–	8.12 ± 0.18	7.7 ± 2.4	8.131 ± 0.086 ∗
72	3621005032.0	1.299	–	8.828 ± 0.076	8.52 ± 0.26	–	8.283 ± 0.092	8.09 ± 0.45	8.296 ± 0.049
73	3621005033.0	1.376	–	8.802 ± 0.042	8.47 ± 0.20	8.33 ± 0.44	8.315 ± 0.052	8.00 ± 0.19	8.387 ± 0.026
74	3621005034.0	1.048	–	8.69 ± 0.14	8.49 ± 0.34	–	8.34 ± 0.94	8.2 ± 2.4	8.335 ± 0.059
75	3621005037.0	1.230	–	8.79 ± 0.07	8.43 ± 0.26	–	8.254 ± 0.048	8.16 ± 0.23	8.272 ± 0.028
78	3621005055.0	0.379	–	9.0006 ± 0.0052	8.9294 ± 0.0058	8.87 ± 0.15	8.611 ± 0.011	8.796 ± 0.026	8.4642 ± 0.0038
81	3621005057.0	0.198	–	9.0383 ± 0.0029	8.9555 ± 0.0067	8.79 ± 0.19	8.626 ± 0.015	8.72 ± 0.03	8.5007 ± 0.0043
82	3621005057.2	0.198	–	9.0987 ± 0.0022	9.0275 ± 0.0051	8.75 ± 0.13	8.682 ± 0.016	8.688 ± 0.025	8.5694 ± 0.0049
83	3621005067.0	0.804	–	8.898 ± 0.014	8.757 ± 0.027	8.61 ± 0.23	8.472 ± 0.038	8.486 ± 0.083	8.423 ± 0.011
85	3621005069.0	1.442	–	8.39 ± 0.09	8.34 ± 0.29 ∗	7.92 ± 0.56 ∗	8.332 ± 0.073	8.06 ± 0.19	8.270 ± 0.029

Table A4 – *continued*

ID	Region	R/R$_{25}$	Z_{T_e}	$Z_{R_{23}}$	$Z_{\rm N2O2}$	$Z_{\rm N2S2}$	$Z_{\rm N2H\alpha}$	$Z_{\rm N2S2H\alpha}$	$Z_{\rm O3N2}$
86	3621005069.3	1.442	–	8.599 ± 0.039	8.453 ± 0.088	8.21 ± 0.38 ∗	8.295 ± 0.039	8.13 ± 0.12	8.247 ± 0.021
87	3621005069.4	1.442	–	8.386 ± 0.072	8.45 ± 0.23	8.01 ± 0.44 ∗	8.352 ± 0.048	8.10 ± 0.13	8.253 ± 0.021
88	3621005070.1	1.176	–	8.7115 ± 0.0044	8.507 ± 0.051	8.29 ± 0.22 ∗	8.179 ± 0.021	8.238 ± 0.099	8.150 ± 0.014 ∗
89	3621005070.2	1.176	–	8.610 ± 0.025	8.52 ± 0.14	7.75 ± 0.40 ∗	8.240 ± 0.035	8.10 ± 0.14	8.181 ± 0.021 ∗
90	3621005086.0	1.479	–	8.647 ± 0.022	8.30 ± 0.31 ∗	8.26 ± 0.45 ∗	8.239 ± 0.042	8.12 ± 0.14	8.238 ± 0.021
91	3621005087.0	1.937	–	8.821 ± 0.046	8.52 ± 0.16	8.44 ± 0.41	8.294 ± 0.043	8.27 ± 0.16	8.309 ± 0.022
92	3621005089.0	1.644	–	8.75 ± 0.14	8.57 ± 0.29	–	8.36 ± 0.11	8.26 ± 0.59	8.339 ± 0.067
93	3621005090.0	1.827	–	8.82 ± 0.05	8.57 ± 0.18	8.54 ± 0.43	8.335 ± 0.055	8.37 ± 0.17	8.344 ± 0.026
94	3621005091.0	1.996	–	8.82 ± 0.02	8.34 ± 0.27 ∗	8.22 ± 0.43 ∗	8.238 ± 0.029	8.08 ± 0.15	8.318 ± 0.021
95	5068001006.1	0.099	–	8.9308 ± 0.0045	8.887 ± 0.022	8.57 ± 0.26	8.516 ± 0.027	8.595 ± 0.056	8.3703 ± 0.0082
96	5068001006.2	0.099	–	8.9849 ± 0.0067	8.909 ± 0.012	8.56 ± 0.23	8.613 ± 0.024	8.487 ± 0.032	8.4738 ± 0.0058
106	5068002272.0	0.195	–	8.9642 ± 0.0095	8.8894 ± 0.0092	8.58 ± 0.24	8.618 ± 0.021	8.488 ± 0.035	8.4807 ± 0.0063
108	5068002323.0	0.464	–	8.8798 ± 0.0028	8.735 ± 0.011	9.25 ± 0.20 ∗	8.372 ± 0.013	8.453 ± 0.034	8.3167 ± 0.0043
118	5201001038.0	0.441	–	8.750 ± 0.036	8.515 ± 0.022	8.09 ± 0.19 ∗	8.2547 ± 0.0082	8.170 ± 0.025	8.231 ± 0.007
119	5201001038.2	0.441	–	8.821 ± 0.045	8.50 ± 0.12	8.22 ± 0.28 ∗	8.241 ± 0.027	8.10 ± 0.10	8.246 ± 0.018
120	5201001053.1	0.185	–	8.743 ± 0.057	8.65 ± 0.05	8.03 ± 0.42 ∗	8.386 ± 0.038	8.118 ± 0.092	8.311 ± 0.017
123	5201001069.0	0.115	–	8.8305 ± 0.0072	8.7332 ± 0.0069	8.42 ± 0.21	8.3110 ± 0.0066	8.405 ± 0.019	8.2489 ± 0.0028
124	5201001075.0	0.477	–	8.682 ± 0.033	8.28 ± 0.29 ∗	7.45 ± 0.53 ∗	8.200 ± 0.038	7.92 ± 0.21	8.199 ± 0.021 ∗
125	5201001133.1	1.109	–	8.641 ± 0.079	8.35 ± 0.28	7.37 ± 0.30 ∗	8.204 ± 0.052	7.87 ± 0.35	8.181 ± 0.035 ∗
126	5201001133.2	1.109	–	8.702 ± 0.019	7.58 ± 0.28	7.34 ± 0.60 ∗	8.191 ± 0.016	7.838 ± 0.079	8.2138 ± 0.0088
132	5236004216.0	0.537	–	9.13521 ± 0.00056	9.102 ± 0.011	–	8.705 ± 0.034 ∗	9.00 ± 0.12	8.5892 ± 0.0067
133	5236004309.0	0.503	–	9.0212 ± 0.0005	9.01 ± 0.01	8.82 ± 0.15	8.658 ± 0.032	8.906 ± 0.096	8.4452 ± 0.0063
134	5236004341.0	0.568	–	9.12714 ± 0.00083	9.1196 ± 0.0094	9.25 ± 0.15 ∗	8.770 ± 0.036 ∗	8.896 ± 0.084	8.5859 ± 0.0071
135	5236006127.0	2.064	–	8.7151 ± 0.0094	8.69 ± 0.03	–	8.358 ± 0.028	8.671 ± 0.097	8.2605 ± 0.0097
140	5236009025.0	0.623	–	9.0639 ± 0.0014	9.1276 ± 0.0096	–	8.785 ± 0.039 ∗	9.12 ± 0.18	8.4802 ± 0.0079
142	5236009030.1	0.598	–	9.109 ± 0.003	9.1196 ± 0.0069	8.81 ± 0.12	8.913 ± 0.033 ∗	8.785 ± 0.046	8.604 ± 0.008
144	5236009045.1	0.558	–	9.0686 ± 0.0028	9.08 ± 0.01	8.88 ± 0.18	8.880 ± 0.042 ∗	8.867 ± 0.077	8.5581 ± 0.0072
145	5236009045.2	0.558	–	8.665 ± 0.026	8.977 ± 0.011	8.95 ± 0.16	9.196 ± 0.057 ∗	9.001 ± 0.087	8.5038 ± 0.0078
146	5236009150.0	0.134	–	9.1245 ± 0.0034	9.1857 ± 0.0067	8.64 ± 0.17	8.957 ± 0.031 ∗	8.836 ± 0.036	8.5989 ± 0.0075
147	5236009150.2	0.134	–	9.064 ± 0.013	9.1036 ± 0.0091	8.87 ± 0.16	8.980 ± 0.036 ∗	8.88 ± 0.05	8.562 ± 0.013
154	5236009182.0	0.110	–	9.0652 ± 0.0031	9.088 ± 0.011	8.83 ± 0.17	8.893 ± 0.039 ∗	8.821 ± 0.054	8.5450 ± 0.0075
156	5236009205.2	0.058	–	9.1611 ± 0.0018	9.2337 ± 0.0083	8.91 ± 0.17	8.940 ± 0.041 ∗	8.91 ± 0.08	8.6364 ± 0.0064
157	5236009260.0	0.517	–	9.059 ± 0.006	9.0916 ± 0.0088	8.80 ± 0.16	8.85 ± 0.04 ∗	8.78 ± 0.05	8.5142 ± 0.0069
159	5236009278.0	0.472	–	9.131 ± 0.001	9.11 ± 0.01	8.81 ± 0.20	8.718 ± 0.037 ∗	8.759 ± 0.059	8.5812 ± 0.0067
160	5236009284.0	0.518	–	9.0135 ± 0.0047	9.012 ± 0.013	8.76 ± 0.10	8.855 ± 0.043 ∗	8.731 ± 0.057	8.5512 ± 0.0081
161	5236009284.2	0.518	–	9.0582 ± 0.0019	9.048 ± 0.011	8.85 ± 0.18	8.818 ± 0.037 ∗	8.826 ± 0.059	8.5427 ± 0.0063
162	5236009295.2	0.499	–	9.0646 ± 0.0017	9.038 ± 0.012	8.81 ± 0.19	8.748 ± 0.035 ∗	8.762 ± 0.051	8.527 ± 0.005
163	5236009295.3	0.499	–	9.0477 ± 0.0032	9.028 ± 0.012	8.73 ± 0.17	8.665 ± 0.031	8.804 ± 0.069	8.4673 ± 0.0071
164	5236009295.5	0.499	–	8.9926 ± 0.0012	8.997 ± 0.011	8.75 ± 0.13	8.628 ± 0.029	8.863 ± 0.087	8.4106 ± 0.0061
165	5236009295.6	0.499	–	9.0685 ± 0.0015	9.0455 ± 0.0074	8.82 ± 0.17	8.757 ± 0.029 ∗	8.774 ± 0.046	8.530 ± 0.005
166	5236009313.0	0.510	–	9.1120 ± 0.0016	9.1116 ± 0.0072	8.82 ± 0.17	8.847 ± 0.029 ∗	8.792 ± 0.039	8.5920 ± 0.0053
182	5236010172.0	1.112	–	8.8422 ± 0.0014	8.845 ± 0.015	–	8.50 ± 0.03	8.90 ± 0.12	8.3399 ± 0.0065
186	5236010338.0	1.411	–	8.910 ± 0.021	8.825 ± 0.028	8.60 ± 0.21	8.464 ± 0.035	8.609 ± 0.095	8.360 ± 0.011
190	628001026.0	0.095	–	8.922 ± 0.059	8.945 ± 0.048	–	8.79 ± 0.14 ∗	8.74 ± 0.32	8.493 ± 0.031
191	628001677.0	0.753	–	8.902 ± 0.012	8.947 ± 0.023	8.56 ± 0.22	8.338 ± 0.027	8.56 ± 0.11	8.25 ± 0.01
196	628001724.0	0.897	–	8.7641 ± 0.0097	8.763 ± 0.033	8.309 ± 0.084	8.459 ± 0.043	8.369 ± 0.093	8.321 ± 0.012

Table A5. The measured unbroken metallicity gradients for NGC 3621 as tested within Section 5.2.2. Also provided are the mean and total data-fit residuals for both forms used to confirm a preferred broken gradient form.

Host Galaxy	Method	N	Slope (dex $R_{25}{}^{-1}$)	Intercept ($12 + \log(O/H)$)	Unbroken residuals (mean, total)	Broken residuals (mean, total)
NGC 3621	$Z_{R_{23}}$	27	-0.284 ± 0.042	9.111 ± 0.031	0.120, 3.236	0.092, 2.473
	Z_{N2O2}	19	-0.412 ± 0.041	9.093 ± 0.020	0.086, 1.641	0.039, 0.736
	Z_{N2S2}	10	-0.201 ± 0.080	8.769 ± 0.062	0.098, 0.978	0.083, 0.828
	$Z_{\mathrm{N2H}\alpha}$	27	-0.254 ± 0.028	8.668 ± 0.030	0.070, 1.897	0.058, 1.560
	$Z_{\mathrm{N2S2H}\alpha}$	25	-0.379 ± 0.040	8.760 ± 0.035	0.130, 3.260	0.084, 2.110
	Z_{O3N2}	21	-0.158 ± 0.017	8.553 ± 0.015	0.048, 1.008	0.035, 0.739

This paper has been typeset from a TEX/LATEX file prepared by the author.